Patterns of climate variability of the Northern Hemisphere wintertime circulation

Roberta Quadrelli

A dissertation submitted in partial fulfillment of
the requirements for the degree of

Doctor of Philosophy

University of Washington

2004

Program Authorized to Offer Degree: Atmospheric Sciences

University of Washington

Graduate School

This is to certify that I have examined this copy of a doctoral dissertation by

Roberta Quadrelli

and have found that it is complete and satisfactory in all respects,
and that any and all revisions required by the final
examining committee have been made.

Chair of Supervisory Committee:

_____

John M. Wallace

Reading Committee:

_____

David S. Battisti

_____

Christopher S. Bretherton

_____

John M. Wallace

Date: _____

In presenting this dissertation in partial fulfillment of the requirements for the doctoral degree at the University of Washington, I agree that the Library shall make its copies freely available for inspection. I further agree that extensive copying of this dissertation is allowable only for scholarly purposes, consistent with "fair use" as prescribed in the U.S. Copyright Law. Requests for copying or reproduction of this dissertation may be referred to Bell and Howell Information and Learning, 300 North Zeeb Road, Ann Arbor, MI 48106-1346, to whom the author has granted "the right to reproduce and sell (a) copies of the manuscript in microform and/or (b) printed copies of the manuscript made from microform."

Signature_____

Date_____

University of Washington

Abstract

Patterns of climate variability of the Northern Hemisphere wintertime circulation

by Roberta Quadrelli

Chair of Supervisory Committee:

Professor John M. Wallace
Atmospheric Sciences

The principal patterns of variability of the extratropical Northern Hemisphere (NH) wintertime circulation are examined. The two-dimensional phase space defined by the two leading PCs of the monthly-mean sea-level pressure (SLP) field poleward of 20°N is used as a basis for surveying the structure of the geopotential height and other fields. The leading EOF corresponds to the NH annular mode (NAM) and the second EOF resembles the Pacific-North American (PNA) pattern. Together these two patterns account for roughly half the variance of SLP on interannual time scales and longer, and virtually all the planetary-scale SLP trends over the 42 year period of record. Also, all the most important NH patterns of variability can be described in terms of our two basis functions; therefore, several of the pattern definitions found in the climate literature are shown to be redundant.

The relationship between the low frequency variability and time scales closer to the synoptic time scale are investigated by studying the variability observed within four different subsets of the climatology as defined by the high-index and low-index polarities of the 10-day mean projections of the two SLP PCs. The variability of

the flow is substantially different within those different mean states. Within the individual subsets of the climatology there are suggestions of multiple circulation regimes; teleconnection patterns for the subsets of the climatology are also discernibly different; cold temperature anomalies associated with low polarities of both PCs are observed more frequently than expected on the basis of linear correlation analysis. These results constitute evidence of non-normal or non-linear behavior of 10-day mean fields, and provide indications that the intraseasonal variability depends on the mean state of the flow in which it is embedded.

The latter idea is extended to investigate the effects of changes in the winter mean background flow observed in association with the ENSO cycle upon the extratropical month-to-month variability. The structure of the NAM is shown to be significantly different during warm and cold winters of the ENSO cycle. Furthermore, the observed NH surface trends of the period 1958-99 were much stronger during the years characterized by warm ENSO events.

TABLE OF CONTENTS

LIST OF FIGURES

LIST OF TABLES

ACKNOWLEDGMENTS

I would like to thank the generous advising of Mike Wallace throughout these years. His love for science is contagious, his support to students is constant, attentive and considerate, his immense scientific knowledge is matched by a similarly great modesty.

Thank you to my reading committee: I enjoyed very much working with Chris Bretherton and I appreciated the insightful suggestions of David Battisti on my thesis. Many thanks to our Chairman Dennis Hartmann, for his help and inspiration, and for making the working environment more pleasant through the "Atmospherics" performances. Thanks also to Greg Hakim for serving on my committee. Special thanks to the professors who a-priori made this experience possible by inspiring me to look into the climate sciences: Franco Molteni and Stefano Tibaldi.

Thanks to Marcia for taking care of me a like a real mother!

Friends of course... Thanks to Dan, Tom, Jack for precious help and fun, Vera, Janet, Alex, Wei and Claire for their nice encouragement, Alberto, Vanina, Francesca-s, Valentina and Alessia for their constant support from Italy, Todd and all the Jisao grads for making such a great work environment. Special thanks to Ioana, my first and unforgettable TA... and unique friend!

Finally, thanks to my mother, Stefano, Silvia, Giulia, Nicola and all the (large) family, for being supportive in all the moments of need. Francis, thanks for your help with science, your endless trips to US, your patience on (and off) the phone, ... your love.

Chapter 1

INTRODUCTION: THE LOW FREQUENCY VARIABILITY OF THE NORTHERN HEMISPHERE EXTRATROPICS

Because of the existence of land/sea contrasts and orography, the wintertime climatological flow of the Northern Hemisphere is far from zonal, with deep troughs over the eastern parts of the American and Asian continents. The geographical distribution of variance is also highly inhomogeneous, with marked maxima over the ocean basins. These two points are exemplified in Fig. 1.1 for the monthly 500 hPa geopotential height level.

Figure 1.1: Maps of mean and variance of the monthly 500 hPa geopotential height, December through March 1958-99. NCEP-NCAR data. Contours every 60 m, bold 5100, 5400, 5700 m (left), and at 1600, 2500, 3600, 4900 (bold), 6400, 8100, 10000 m^2 (right).

On the month-to-month time scale, the variance shown tends to manifest itself through organized large-scale patterns of variability. Efforts to describe this covari-

ability between regions far apart have led to an abundance of definitions of indices, each referring to a particular pattern, fixed in space, empirically identified based on observations of variables such as geopotential height, sea level pressure, temperature, ..., or a combination thereof. However, from a dynamical point of view, only a few basic mechanisms have been invoked to explain the observed patterns of variability.

In this chapter we summarize our current understanding of the most important features of extratropical atmospheric wintertime climate variability of the northern hemisphere, from both an observational and theoretical point of view. Such a description will naturally lead to a discussion of the motivation for this thesis.

1.1 Diagnostic studies: the need for synthesis

We present here a summary of the major definitions of observed patterns of the extratropical northern hemisphere variability found in the literature, starting with the zonally symmetric patterns. In the process of describing the patterns we will highlight the contrast between the large number of papers that have been written to define patterns and the minimal effort to place them within a unified framework.

1.1.1 Zonally symmetric flow

Many observational studies have been devoted to the description of the zonally symmetric component of the flow. An early paper by Exner (1913) already observed an out-of-phase covariability between high- and mid-latitude sea level pressure station data. Rossby (1939) observed the variation in strength of the westerlies along 45°N and its systematic relation with the position of the Aleutian low. Later on, Willett (1948) and Rossby and Willett (1948) introduced the idea of a "zonal index", based on the meridional pressure gradient between 35°N and 55°N, which could fluctuate between "high" and "low" states. By analyzing correlation coefficients between zonal mean sea level pressure at different latitudes throughout the hemisphere,

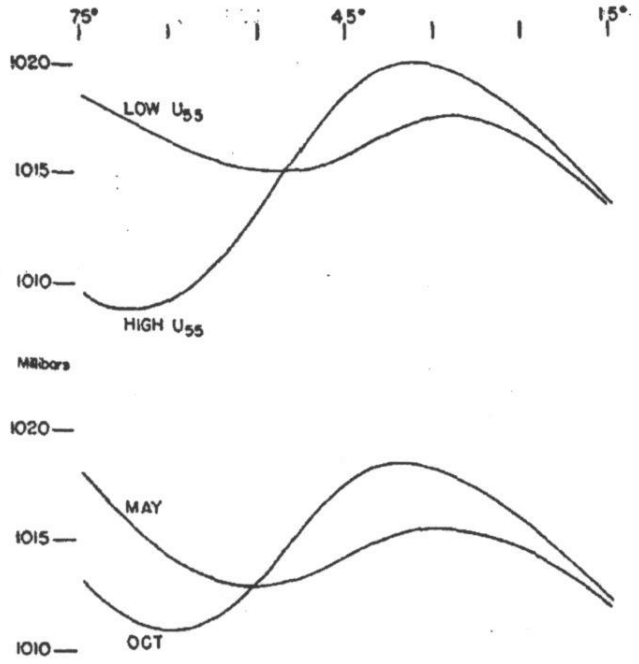

Figure 1.2: Typical Northern Hemisphere zonally averaged sea level pressure profiles associated with high and low values of the zonal index, compared with climatological sea level pressure profiles of October and March. From Lorenz (1951).

Lorenz (1951) deduced that fluctuations in position of the zonal mean zonal wind around 55°N were dominating the extratropical variability; he also noticed that this mode of month-to-month variability was similar in structure to the variation of the climatological jet position associated with the seasonal cycle (as shown in Fig. 1.2). Lorenz's idea of a north-south shift of the midlatitude jet as a mode of variability was consistent with the theory proposed by Namias (1950), who hypothesized a cyclical alternation between high and low index states of the zonal mean zonal wind ("zonal index cycle"), associated with the latitudinal expansion or contraction of the polar vortex. The consequent modulation in the frequency of cyclogenesis, expected by Namias to occur at the same time as the cycle throughout the hemisphere, was not actually observed in weather data. This "failure" contributed to a decrease of interest

in the zonally symmetric patterns that persisted until recently, accompanied by an increase of interest in zonally asymmetric patterns (described in section 1.1.2).

Following the identification of a zonally symmetric pattern of variability in the southern hemisphere (see for example the "High Latitude Mode" in Kidson (1988)), the definition of the northern and southern annular modes (Thompson and Wallace, 1998, 2000) made the "zonal index" re-emerge as a paradigm. The NAM and SAM are now established as fundamental modes of variability of the extratropics in both hemispheres, and have been substantiated by strong dynamical evidence (see section 1.2.1).

1.1.2 Teleconnections

A broader group of patterns, known as "teleconnection" patterns, refers to simultaneous variations of a given variable at widely separated points in space; in contrast with the zonally symmetric patterns, which are functions of latitude only, teleconnection patterns are generally characterized by a two-dimensional horizontal structure.

The idea of covariability between atmospheric variables in distant regions, found in Walker and Bliss (1932) among other early studies, was emphasized by van Loon and Rogers (1978) with reference to the seesaw in winter temperature between Greenland and Northern Europe, now identified as North Atlantic Oscillation (NAO). The first systematic work on teleconnections on a hemispheric scale was the paper by Wallace and Gutzler (1981), who defined a set of patterns based on the "teleconnectivity", the strongest negative correlation between geopotential height at a given gridpoint and geopotential height at any other gridpoint. Examples of structures identified in that study include the NAO, the Pacific-North American (PNA) pattern, and the Eastern Atlantic (EA) pattern. Other authors followed this paradigm by introducing an even larger number of spatial patterns. Figure 1.4 reproduces a table from Barnston and Livezey (1987), which compares several definitions of regional and hemispheric patterns found in different papers, and gives a qualitative impression of the large

Figure 1.3: The Pacific-North American (PNA) pattern, as defined in Wallace and Gutzler (1981).

number of pattern definitions that had emerged by the late 1980s.

Among the statistical methodologies used, principal component analysis (sometimes with rotation) has been applied to a large variety of fields and over different regions to retrieve large scale patterns of variability (Kutzbach, 1970; Trenberth and Paolino, 1980; Horel, 1981; Kushnir and Wallace, 1989; Barnston and Livezey, 1987; Feldstein, 2000). Alternative linear analysis techniques have been explored like, for example, the "empirical orthogonal teleconnections" of van den Dool et al. (2000). As a consequence of the variety of methodologies, a large number of patterns have been identified in diagnostic studies. Some of those patterns (like the NAO and the PNA pattern) are more robust than others, and appear reproducible in independent studies. However, in all the cases, the choice of methodology has influenced the resulting patterns, at least to some degree.

APPENDIX B

Winter Comparison of the Present Study's Orthogonally Rotated Principal Component Results with Results of Five Major Studies of Low-frequency Upper-air Variability in the Northern Hemisphere

	Barnston and Livezey (1987) (present study)	Wallace and Gutzler (1981) (WG)	Horel (1981) (H81)	
Analysis method, meteorological parameter	orthogonally rotated principal components of 700 mb height	teleconnections of 500 mb height	orthogonally rotated principal components of 500 mb height	
Grid	358-point approx. equal area (derived from NMC 541-point diamond grid)	111-point approx. equal area (derived from NMC 541-point diamond grid)	111-point approx. equal area (derived from NMC 541-point diamond grid)	120-point approx. equal area (every 4th point of NMC octogonal grid)
Source of data	NMC	NMC: obtained from NCAR	NMC: obtained from NCAR	NMC
Period of record	1950–84 (35 years)	1963–1977 (15 years), and 1950–1962 (13 years)	1963–1977 (15 years)	1951–1980 (30 years)
Averaging period per sampling element	1-month	1-month	1-month	1-month
Concatenation (pooling) time window; sampling elements per time window	1 month (Jan); 1	3 months (DJF); 3	3 months (DJF); 3	3 months (DJF); 3
Major preprocessing of data	treatment of early 1950s analysis bias in Caribbean and North Africa; exclusion of grid points in Himalayas, India, Saudi Arabia			
Names of robust January circulation patterns found in present study, with names of corresponding winter patterns found in the other studies	North Atlantic Oscillation (NAO) (mode 1: 11.1%)	Western Atlantic (WA)	mode 5 (6.1%)[1] / mode 3 (7.3%)[2]	mode 10 (4.5%)
	Pacific/North American (PNA) (mode 2: 10.8%)	Pacific/North American (PNA)	mode 2 (8.7%)	mode 1 (7.8%)
	West Pacific Oscillation (WPO) (mode 3: 9.8%)	Western Pacific (WP)	mode 1 (12.9%)	mode 3 (6.1%)
	Tropical/Northern Hemisphere (TNH) (mode 4: 9.8%)		mode 5 (6.1%)[1] / mode 6 (5.0%)[3]	mode 5 (5.5%)
	Northern Asian (NA) (mode 5: 8.3%)		mode 4 (6.9%)	
	Eurasian #1 (EU1) (mode 6: 8.0%)	Eurasian (EU)[1]	mode 8 (4.5%)[4] / mode 10 (4.0%)	
	Eurasian #2 (EU2) (mode 7: 7.7%)		mode 9 (4.5%)	
	East Atlantic (EA) (mode 8: 5.8%)	Eastern Atlantic (EA)	mode 3 (7.3%)	mode 2 (7.0%)
	East Pacific (EP) (mode 10: 5.0%)		mode 7 (4.7%)	
Column footnotes		[1] Japanese center version	[1] is westward-displaced NAO and northeastward-displaced TNH without Pacific center [2] good as EA; also is southeast version of NAO [3] only 2 western centers appear: mode 5 provides some of Caribbean center [4] mode 8: Mongolian and Japanese centers mode 10: Scandanavian center	
Patterns not corresponding to any of those classified in present study				mode 4 (5.8%)* mode 6 (4.9%)* mode 7 (4.9%)* mode 8 (4.7%)* mode 9 (4.6%)** * Single, subtropical center ** Single, mid-latitude center

Figure 1.4: Appendix B from Barnston and Livezey (1987).

APPENDIX B (*Continued*)

Esbensen (1984) (E)		Lebow and Toldalagi (1985) (LT)	Hsu and Wallace (1985) (HW)
teleconnection of 700 mb height		obliquely rotated principal components of 700 mb height	500 mb height patterns associated with orthogonally rotated principal components of sea level pressure
541-point NMC diamond grid (36 points per latitude circle)		111-point approx. equal area (derived from NMC 541-point diamond grid)	1977-point NMC octagonal equal area
NMC		NMC	NMC: obtained from NCAR
1950–1977 (28 years)		1949–1982 (34 years)	1947–1977, without 1960, 1961 (29 years)
1-month		½-month	5-day
3 months (DJF); 3		2 months (mid-Dec. to mid-Feb.); 4	5 months (NDJFM); 30
digital filter to obtain intermonthly signal	digital filter to obtain interannual signal		
Western Atlantic (WA) / Zonally-Symmetric Seesaw (ZS)*	Western Atlantic (WA) / Zonally-Symmetric Seesaw (ZS)[1]	mode 2 (8.8%)	Atlantic pattern (A) (SLP mode 1: 7.3%)
Pacific-North American (PNA)	Pacific-North American (PNA)	mode 4 (7.0%)	Pacific/North American (PNA) (SLP mode 6: 4.8%)
Western Pacific (WP)[1]		mode 1 (8.9%)	Pacific pattern (P)[1] (SLP mode 3: 6.1%)
	Zonally-Symmetric Seesaw (ZS)[1]	mode 7 (5.8%)	
Northern Asian (NA)		mode 5 (6.1%)[1]	Siberian Pattern (S) (SLP mode 2: 6.1%)
Eurasian (EU)*[2]	Eurasian (EU)*[2]	mode 10 (4.3%)[2]	Chinese Pattern (C)[2] (SLP mode 4: 5.9%)
Eastern Atlantic (EA)[3]	Eastern Atlantic (EA)*[3] / Zonally-Symmetric Seesaw (ZS)[1]	mode 9 (4.5%)[3]	
Eastern Atlantic (EA)[3]		mode 6 (6.0%)	unnamed; "N-S seesaw with major center over North Africa"[3] (SLP mode 5: 5.1%)
	North Pacific (NP)	mode 8 (5.7%)	
[1] less prominent U.S. center	[1] most strongly NAO, but clearly contains TNH and EU2 also	[1] strong European center also	[1] translated east
[2] Japanese center version	[2] Japanese center version	[2] all 4 centers represented	[2] only Mongolian and Japanese centers
[3] mixture of EA (Atlantic center displaced to east) and EU2 (eastern center displaced to northwest)	[3] mixture of EA (Atlantic center displaced to east) and EU2 (eastern center displaced to northwest)	[3] somewhat different (Caspian center shifted southwest, Chinese center shifted northwest, Pacific center appears)	[3] pattern not shown in paper
* interannual signal stronger	* intermonthly signal stronger		
		mode 3 (7.2%)	

Figure 1.4: (continued).

1.1.3 Nonlinear paradigm

Complementary to the linear framework discussed in the previous subsections, several studies have tried to identify patterns on the basis of nonlinear analysis procedures. The most popular nonlinear perspective is the idea of a regime-like behavior of the atmosphere, which stems from works such as Lorenz (1963) on chaotic systems, or by Charney and DeVore (1979) on multiple equilibria in the atmospheric flow. A theoretical overview is presented in Palmer (1999), with emphasis on the changes in frequency of occurrence of different regimes induced by an external forcing such as the greenhouse effect. Examples of methodologies used to identify multiple equilibrium states of the extratropical flow include the search for multimodality in the probability density function of circulation indices (Sutera, 1986; Molteni et al., 1988; Kimoto and Ghil, 1993a,b; Corti et al., 1999), the search for patterns whose time derivative vanishes (Vautard and Legras, 1988; Vautard, 1990), and nonlinear principal component analysis (Monahan, 2000; Monahan et al., 2000; Monahan and Fyfe, 2001). Cluster analysis has probably been the favorite tool to look for regimes, both hemispheric (Mo and Ghil, 1988; Molteni and Palmer, 1990; Cheng and Wallace, 1993; Wu and Straus, 2003), and regional (Cheng and Wallace, 1993; Robertson and Ghil, 1999).

1.1.4 Patterns of climate change

Global climate change and its regional manifestations are attracting great interest. The observation and description of interdecadal variability and trends has recently motivated a renewed interest in previously identified patterns, as well as the definition of new indices. Hurrell (1995), Thompson et al. (2000), Gillet and Thompson (2003) stressed the importance of the NAO and the annular modes (NAM and SAM), respectively, in explaining observed trends in sea level pressure. Examples of "ad hoc" patterns defined in the context of decadal variability and climate change include Wallace et al.'s (1995) cold ocean warm land (COWL) pattern, which is helpful in in-

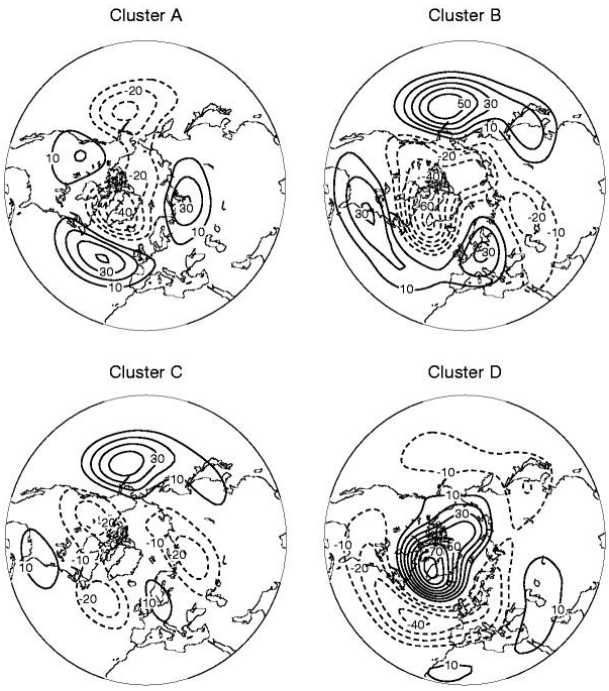

Figure 1.5: Four atmospheric regimes identified in Corti et al. (1999).

terpreting the pattern of hemispheric mean temperature trends; Nitta and Yamada's (1989) index of the intensity of the Aleutian low (Nitta and Yamada, 1989); Trenberth and Hurrel's (1994) North Pacific index, which monitors decadal variations of the North Pacific sea level pressure; Walsh et al.'s (1996) index of the Arctic sea level pressure used to monitor local changes in the Arctic region; and the Pacific Decadal Oscillation (Mantua et al., 1997), which describes long term variations of sea surface temperature in the Pacific basin.

1.2 Dynamical concepts

From a dynamical point of view, two main internal physical mechanisms have been succesfully shown to have spatial signatures consistent with observed patterns of extratropical variability: interaction between the storm tracks and the background

flow, and barotropic instability of zonally varying climatological mean flow.

1.2.1 Zonally symmetric dynamics

In recent years the importance of positive eddy feedback in maintaining zonal mean wind anomalies has emerged, building on results for simple models and for southern hemisphere observations, whose patterns of variability are more zonally symmetric than those in the northern hemisphere. Using zonally symmetric models with various degrees of complexity Robinson (1991), Lee and Feldstein (1996), and Feldstein and Lee (1996) have shown that zonal wind anomalies are mantained by eddy momentum flux convergence; similar results have been obtained for the southern hemisphere (Karoly, 1990; Hartmann and Zuercher, 1998; Limpasuvan and Hartmann, 2000). Studies on northern hemisphere observations have followed (DeWeaver and Nigam, 2000; Limpasuvan and Hartmann, 2000), which proposed quasi-stationary waves and transient eddies as sources of the positive feedback necessary to maintain zonal wind anomalies. More recent works of Lorenz and Hartmann (2001, 2003) on the observed southern and northern annular modes, respectively, have shown that high frequency eddies play a critical role: baroclinic wave development is enhanced in regions of westerly wind anomalies, and the propagation of wave activity out of these source regions is associated with a positive momentum flux into the jet, which reinforces the westerly wind anomalies.

1.2.2 Zonally asymmetric teleconnections

The wavelike structure of observed teleconnection patterns is consistent with Rossby wave dispersion on a sphere, with a prevalence of wavetrains oriented along "great circle routes" (Hoskins et al., 1977). For example, the global teleconnection patterns associated with ENSO resemble the Rossby-wave response to a heat source in the central equatorial Pacific (Hoskins and Karoly, 1981; Horel and Wallace, 1981).

The work of Simmons et al. (1983) on the barotropic instability of the zonally asymmetric climatological flow provides a partial explanation of the existence of geographically fixed teleconnection patterns. Their barotropic model, linearized about the wintertime climatology, showed structures qualitatively similar to the PNA or the EA patterns emerging as fastest growing modes. These perturbations were able to grow in the regions of diffluence of the jet, extracting energy from it. The key point is the structure of the time-mean flow, which determines, indirectly, the structure of the low frequency variability. Later papers have studied the PNA in more detail: Sardeshmukh et al. (1997) showed that barotropic processes alone cannot account for its time evolution; Feldstein (2002) showed that the two upstream centers grow through barotropic energy conversion, that dispersion transfers energy to the two downstream anomalies, and that additional processes (like transient eddy forcing and diabatic heating) can play important roles in the life cycle of such low-frequency anomalies. Cash and Lee (2001) proposed an integrated view of previous theories: the PNA can be excited both by tropical convection and by midlatitude stochastic forcing (e.g. anomalous high-frequency eddies), it amplifies by extracting energy from the zonally asymmetric flow, it can be reinforced by the high-frequency eddies which are reorganized by the large scale flow anomalies, and it decays because of linear Rossby wave dispersion of energy.

1.3 Changes in the basic state of the flow

Given the mismatch between the large number of identified patterns and the small number of proposed physical mechanisms, it is probable that just a few dynamical mechanisms can result in a variety of spatial patterns of low frequency variability when acting, for example, on different climatological mean states. Simmons et al. (1983) very briefly explored this idea by linearizing their barotropic model around different mean states of the winter streamfunction field. In this way, a set of quite

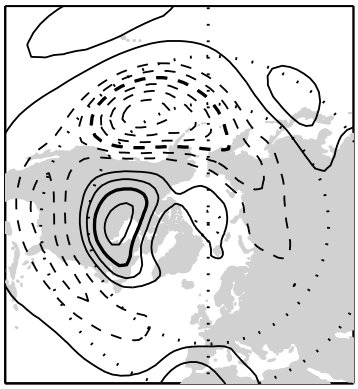

Figure 1.6: Regression of monthly 500 hPa geopotential height field upon standardized CTI time series, December through March 1958-1999. Contours every 5 m, bold 15 m, negative dashed.

different response patterns was obtained. Also, analyzing the wintertime low frequency variability, Kushnir and Wallace (1989) discussed how the lack of uniqueness of the basic state (due to interannual variability, or to the seasonal cycle within the same season) leads to a variety of positions for the main waveguides, and, as a consequence, for the modal structures embedded in them. The comprehensive review of Barnston and Livezey (1987) included an analysis of the variations, in shape and in explained variance, of several patterns of variability, due to the seasonal evolution of the climatological mean flow. More recently, Newman and Sardeshmukh (1998) have analyzed the impact of the annual cycle of the wind field on Rossby wave propagation over the North Pacific region, and have concluded that "the annual cycle must be taken into account in any complete theory of low-frequency variability".

The annual cycle is one source of variation of the basic state flow; another is associated with the global circulation anomalies induced by ENSO. The occurrence of a positive or negative phase of the ENSO is predictable several months in advance, and its signature persists over a whole winter, making it an extremely interesting "natural experiment". The direct effect of an El Niño or La Niña event on the basic state

flow is a displacement in latitude of jets and their associated baroclinic activity, in accordance with the pattern of 500 hPa height anomalies in Fig. 1.6. Besides the large body of literature on different aspects of this "direct" (linear and non-linear) ENSO signature on the extratropical circulation, several studies have analyzed the "indirect" changes in variability induced by ENSO. Examples include changes in the probability density function of extratropical regimes due to the SST boundary forcing (Molteni et al., 1993; Robertson and Ghil, 1999; Corti et al., 1999), changes in the frequency of blocking, in observations (Renwick and Wallace, 1996) and in both observations and a GCM (Chen and van den Dool, 1997), changes in the annual cycle of predictability (Kumar and Hoerling, 1998), changes in the intraseasonal variability of temperature and the frequency of occurrence of extreme events (Smith and Sardeshmukh, 2000), changes in the variability of seasonal anomalies (Sardeshmukh et al., 2000; Kumar et al., 2000), and changes in the variability of seasonal mean forecasts (Schubert et al., 2001).

1.4 Motivation for this thesis

The foregoing historical background suggests the need for a more concise description of the observed extratropical variability. Some of the previously defined patterns are probably redundant -their differences being attributable to the lack of a common criterion for defining such patterns, use of different methodologies, use of station data versus gridded datasets, local versus global definitions, choice of basing indices on different fields, or different height levels; the number of possible choices is extremely large. In addition, different patterns can result when different background states are analyzed with the same technique.

Our purpose here is to define an objective framework for synthetizing most of the scattered and inhomogeneous information described in section 1.1; our frame should also be as simple as possible. Therefore, the initial question we want to address is

which portion of the low frequency variability can be described by using only two basis functions.

Besides facilitating the organization of existing information, the definition of such an objective framework enables comparisons among new patterns, including patterns generated by models; the latter can be particularly useful in the context of climate change studies.

The second question we want to address is how the patterns described within the context of this two dimensional framework can vary in the presence of different basic state flows. The relation between the variability and the climatological flow in which it is embedded has certainly been studied for several phenomena (e.g. Hartmann and Zuercher (1998) for baroclinic waves and zonal flow). Here we want to extend this question to the structure of our low frequency patterns of variability. The current record of observations is starting to be long enough to enable stratification of the data according to the phase of specified patterns. Grouping several patterns under a few categories would simplify the understanding of climate variability, and improve the prediction of climate regional impacts.

A further goal is to organize the known patterns of variability under categories which correspond to the basic mechanisms discussed in section 1.2.

1.5 Outline of the thesis

The goal of this thesis is to illustrate the power of a very limited set of basis functions in describing the main features of the low frequency extratropical variability, and to explore applications of this framework. The thesis is comprised of 7 chapters and an appendix.

After the description of the datasets used (chapter 2), chapter 3 describes a two-dimensional phase space that encompasses many of the extratropical NH wintertime teleconnection patterns that have been identified in previous studies. Our phase-space

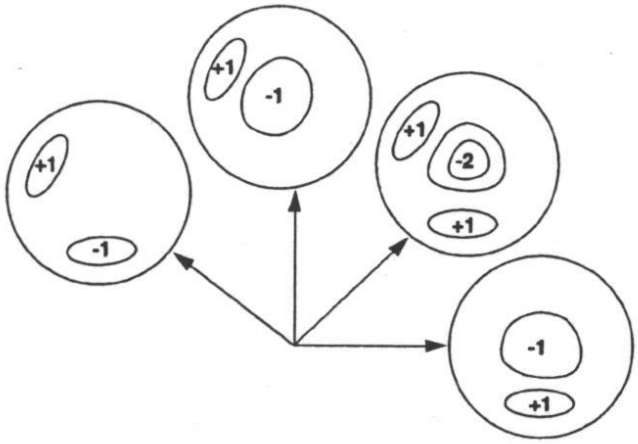

Figure 1.7: Idealized two-dimensional phase-space and sea level pressure patterns, from Wallace and Thompson (2002).

is based on the two leading empirical orthogonal functions (EOFs) of the monthly mean sea level pressure field, which can be roughly associated with the northern annular mode (NAM) and a version of the Pacific North American pattern (PNA). This choice naturally stems from the ideas presented in Wallace and Thompson (2002) in which the authors argued that the simultaneous variability of NAM and PNA as hemispheric patterns could mask correlations between Atlantic and Pacific sectors, while making regional correlations stronger. Fig. 1.7 reproduces their Fig. 3, which illustrates their hypothesis that different linear combinations of the two patterns can result in a variety of hemispheric configurations of the flow. Chapter 3 in this thesis presents an extensive and systematic description of the possible patterns explained by our two eigenvectors together. In chapter 4 we analyze the frequency dependence of our phase space, with special attention to the role of these patterns in hemispheric climate change over the past few decades; our two degrees of freedom explain progressively higher percentages of the variance as one moves toward lower frequencies (from monthly, to interannual, to 5-yr means). Chapters 2 and 3 represent an extended

version of Quadrelli and Wallace (2004a).

The mathematical justification for choosing the eigenvectors of the sea level pressure, as opposed, say, to any other level in the troposphere, is offered in Appendix A, which presents the results of Quadrelli et al. (2004). There we derive and apply a formula for estimating the errors due to sampling variability in the computation of EOFs. The smallest sampling errors for the EOFs of the hemispheric geopotential height field at any level in the troposphere are found to be at the earth's surface. This part of the thesis extends the well known study of North et al. (1982) on sampling variability, which has been widely used to test eigenvalue separation in principal component analysis of atmospheric variables.

In chapter 5, which refers to the results presented in Quadrelli and Wallace (2004b), higher frequency (5-10 day mean data) fields are analyzed, as opposed to the monthly mean data of the previous chapter. Here the analysis focuses on the variability around specified different mean states, which correspond to contrasting polarities of the leading EOFs of the hemispheric field. Special attention is given here to the frequency of occurrence of extreme events and its association with the low frequency variability; the underlying idea being to link the variability in different frequency ranges, by studying how individual events of month-to-month variability differ among each other, and how this can affect the "synoptic" time-scale events.

The same basic idea of studying the dependence of the structure of the variability upon the mean state of the flow is explored in a broader sense in chapter 6 where we investigate whether the changes in the mean hemispheric flow induced by ENSO from a winter season to the next can affect the patterns of extratropical variability represented by our basis functions. Emphasis is given to the annular mode, and its structure. As mentioned earlier (section 1.3), changes in mean jet and baroclinic activity are expected to induce structural changes in a "mode", like the NAM, maintained by the feedback between high frequency eddies and zonal wind. Some of the results of this chapter were published in Quadrelli and Wallace (2002). Both chapters

5 and 6, though focusing on different time scales of variability, stress the importance of considering the patterns of low frequency variability as being "flexible", rather than fixed in space. That the structure of patterns can vary under different climatological flows has important implications, for example in the study of regional climatic impacts.

A chapter of conclusions follows (chapter 7), with a general discussion of the goals that have been achieved and of the questions left open by this thesis.

Chapter 2

DATA AND ANALYSIS TECHNIQUES

The primary dataset used in this study is the National Centers for Environmental Prediction-National Centers for Atmospheric Research (NCEP-NCAR) Reanalysis (Kalnay et al. 1996) obtained from the National Oceanic and Atmospheric Administration (NOAA) Climate Diagnostic Center (CDC). The data are gridded on a 2.5°lat $\times$ 2.5°lon mesh.

We make extensive use of principal component analysis (PCA)[1], performed on the covariance matrix of anomalies obtained after removing the monthly climatology. The anomalies are area-weighted by the square root of the cosine of latitude, and only the region north of 20°N is included in the analysis. The corresponding spatial patterns that we will refer to as EOFs are derived by linearly regressing the anomaly field upon these principal component time series.[2]

The analysis is restricted to the winter season, defined as extending from December through March (DJFM) for the 42 year period of record 1958-1999, a total of 168 months.

The description of the specific fields included in the Reanalysis dataset, of any additional datasets, and of different analysis techniques used in different chapters follows.

---

[1]Principal component (PC) time series and the associated spatial patterns called "empirical orthogonal functions" (EOFs) have been widely used as basis for identifying the dominant patterns of climate variability. Examples include the studies of Kutzbach (1970), Kidson (1975), and Trenberth and Paolino (1981).

[2]This definition of EOF differs slightly form the conventional mathematical definition in the sense the the regression coefficients are not area-weighted.

2.1 Monthly and lower frequency variability

In chapters 3 and 4, the fields used are sea level pressure (SLP), 850, 700, 500, 250, 200, 100, 50, 30, 10-hPa geopotential height, 500 hPa wind, and 850 hPa temperature. An additional SLP dataset for the extended period 1925-1999 (Trenberth and Paolino, 1980) is used to test the robustness of results relating to interannual and longer term variability. We also make use of land temperature and precipitation datasets produced at the University of Delaware by Willmott and collaborators, available from
http : *//climate.geog.udel.edu/˜climate/html_pages/archive.html* for the period 1950-1999: the newest version with "climatologically aided interpolation" (Willmott and Robeson, 1995); monthly values from 1958 through 1999. Higher spatial resolution monthly precipitation data over the region of the Alps ($42-50°$N, $2-19°$E) for the period $1971-1992$ are taken from the Frei and Schär (1998) gridded (0.22°x0.3°lat-lon) dataset.

Principal component analysis (PCA) of monthly DJFM SLP anomalies is performed to obtain the two eigenvectors that define our two-dimensional phase space. The leading two principal component (PC1 and PC2) time series and the associated EOFs may be viewed as comprising the 2-dimensional temporal and spatial phase spaces upon which various time series and spatial patterns can be projected, as described in more detail in the next section.

PCs 1 and 2 of monthly mean DJFM SLP anomalies poleward of 20°N explain 24% and 13% of the total variance of the field, respectively, compared to 9.5% for the third PC. Hence, the first and second PCs qualify as well separated, based on the criterion of North et al. (1982). Figure 2.1 shows the signature of these modes in the monthly mean 500-hPa height and SLP fields, and their monthly time series.

Time varying indices are used to represent a number of previously identified patterns of climate variability. Following Hurrell (1995), the North Atlantic Oscillation

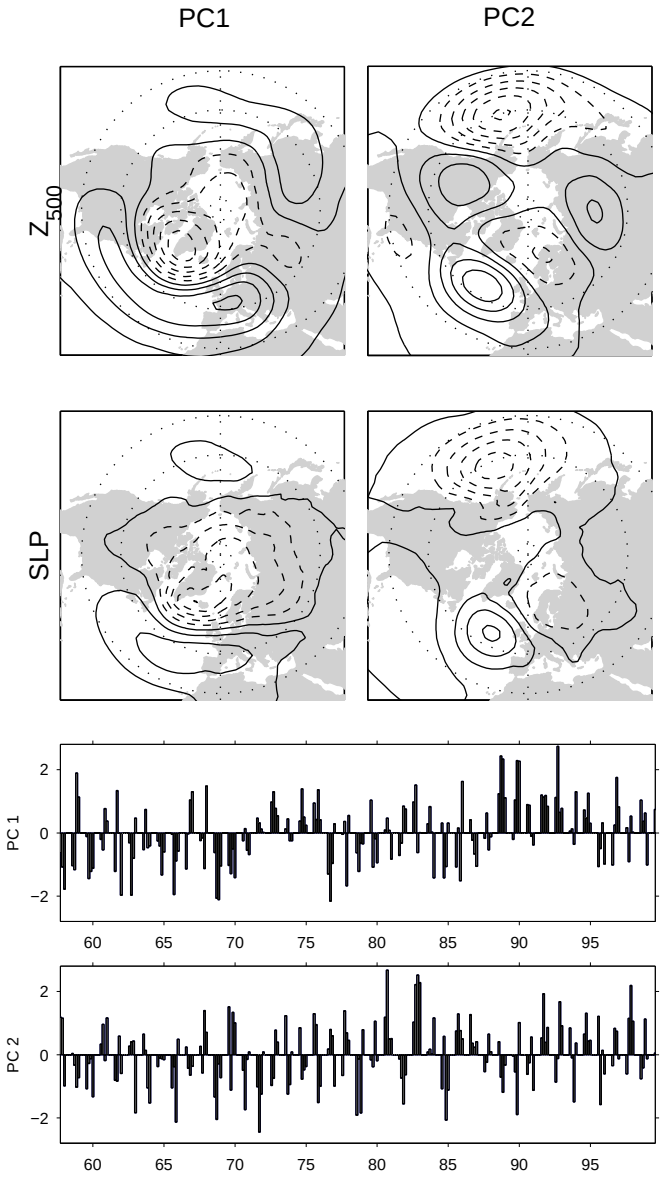

Figure 2.1: Monthly mean 500-hPa height and SLP fields regressed on standardized PCs 1 and 2 of monthly mean DJFM SLP anomalies poleward of 20°N, based on data for the period 1958-1999. Contour interval 1.5 hPa for SLP and 15 m for 500-hPa height; negative contours are dashed. Here and in all the subsequent maps the latitude circle plotted correspond to 30 and 45°N. Lower panels: Time series of the standardized PCs 1 and 2, DJFM values only.

(NAO) is defined as seasonal (December through March) means of the difference between the standardized SLP at Stykkisholmur, Iceland and Lisbon, Portugal, available at: $http://www.cgd.ucar.edu/\tilde{}jhurrell/nao.stat.html$.

Monthly values of the index are obtained by forming time series of SLP for the NCEP gridpoints located closest to the Iceland and Lisbon centers of action of the NAO. The index of the Pacific-North American (PNA) pattern is computed from the 500 hPa winter monthly anomalies at specified gridpoints following the definition given in Wallace and Gutzler (1981, hereafter WG). The depths of the Aleutian and Icelandic lows are defined as SLP anomalies (with sign reversed) averaged over areas surrounding their respective centers of action in the climatological mean SLP field in which the temporal correlation with the center exceeds 0.8. The North Pacific index (Trenberth and Hurrell, 1994) is obtained from: $http://www.cgd.ucar.edu/\tilde{}jhurrell/np.html$. Following Wallace et al. (1995) the cold ocean-warm land (COWL) pattern index is defined as the NH mean surface air temperature poleward of 20°N based on the University of Delaware dataset, based on land data only. The Southern Oscillation index (SOI) is the difference between standardized SLP time series at Tahiti and Darwin, as defined in Trenberth (1984). Monthly data of the SOI index calculated by the NCEP, and based on the University of East Anglia data are obtained from:
$http://tao.atmos.washington.edu/pacs/additional\_analyses/soi.html$. The index of the Pacific Decadal Oscillation (PDO), as defined by Mantua et al. (1997), is obtained from: $http://jisao.washington.edu/pdo/PDO.latest$. The quasi-biennial oscillation (QBO) is defined by the time series of the two leading EOFs of monthly anomalies of zonal wind at equatorial WMO stations at seven height levels in the stratosphere (70, 50, 40, 30, 20, 15, and 10 hPa), which together account for 93% of the year-round variance at those levels for the period 1958-1999. Winter (DJFM) values are selected after performing the EOF analysis on the data on data for all calendar months. The data are available on CD-ROM (Labitzke and Collaborators, 2002).

The index of the leading PC of the monthly vertically and zonally averaged zonal wind in the domain extending from 10°N to 80°N for the winters 1976-1999 (December through March), computed after linearly removing the ENSO variability, as represented by a multivariate index, is the same as in Lorenz and Hartmann (2003).

The leading EOFs of the NH DJFM monthly SLP in a run of the NCAR's Whole Atmosphere Community Climate Model (WACCM) are also included in the analysis. For a summary of the GCM's characteristics, see Sassi et al. (2002). Monthly data for the years 1958-99 are taken from the 1950-2000 run forced with observed SST's, available online at: *https* : *//dataportal.ucar.edu* : 8443/*cdp/index.jsp*.

2.2 10-day variability

For the analysis on 5- and 10-mean data of chapter 5, the NCEP-NCAR Reanalysis fields used are SLP, 500hPa geopotential height and 1000 hPa for the same 42 year period of record 1958-1999 as for monthly data.

In chapter 5 the analysis focuses on subclimatologies comprising the events characterized by the extreme high and low values of SLP PCs. The SLP PCs described in section 2.1 have monthly time resolution; in order to obtain 10-day mean indices of the patterns associated with the PCs, 10-day SLP mean maps are projected onto SLP regression maps based on the standardized monthly PCs. These time series are sorted in ascending order to identify the 10-day intervals or "dectads" in which the hemispheric SLP field projects most strongly (positively and negatively) onto the corresponding EOFs. These selected dectads will subsequently be referred to as "high index" and "low index" subclimatologies, respectively. In order to ensure that the selected subclimatologies include data from many different winter seasons, an additional criterion is imposed that no more than 2 dectads for each winter be included in a given "high index" or "low index" composite. For each of the two modes 30 of the 504 dectads in the 42-winter record are classified as high index and 30 as low index,

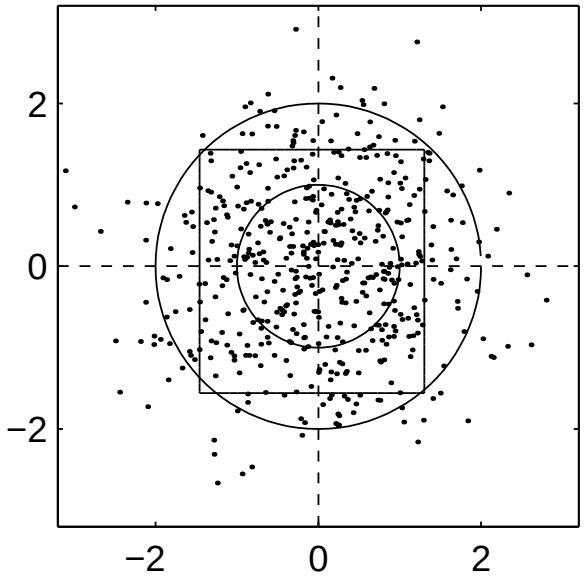

Figure 2.2: Scatterplot showing projections of DJFM 10-day mean SLP anomaly maps upon standardized EOF 1 (x-axis) and EOF 2 (y-axis) of monthly mean DJFM SLP. Circles denote radii of 1 and 2. Solid horizontal and vertical lines delimit highest 30 and lowest 30 values which are used as a basis for the composites in Sections 3 and 4.

and the remaining 444 dectads remain unclassified.

Figure 2.2 shows a scatterplot of the phase space defined by the projection of the complete set of 10-day mean data onto DJFM monthly SLP PC1 and PC2. The solid horizontal and vertical lines delimit the "high index" and "low index" subclimatologies of the data that are used in constructing many of the figures in chapter 5. Figure 2.3 shows how the selected dectads are distributed in time. To contrast the atmospheric variability observed in association with "high index" and "low index" subclimatologies defined on the basis of the polarities of PCs 1 and 2, we present a series of 500 hPa, SLP, and 500-1000 hPa thickness "spaghetti diagrams" in which specified contours for all 30 dectads of the respective subclimatologies are plotted together on the same chart. This method (sometimes referred to as *limited contour analysis*) has been used as a diagnostic tool in several previous works; for example Kimoto and Ghil (1993a)

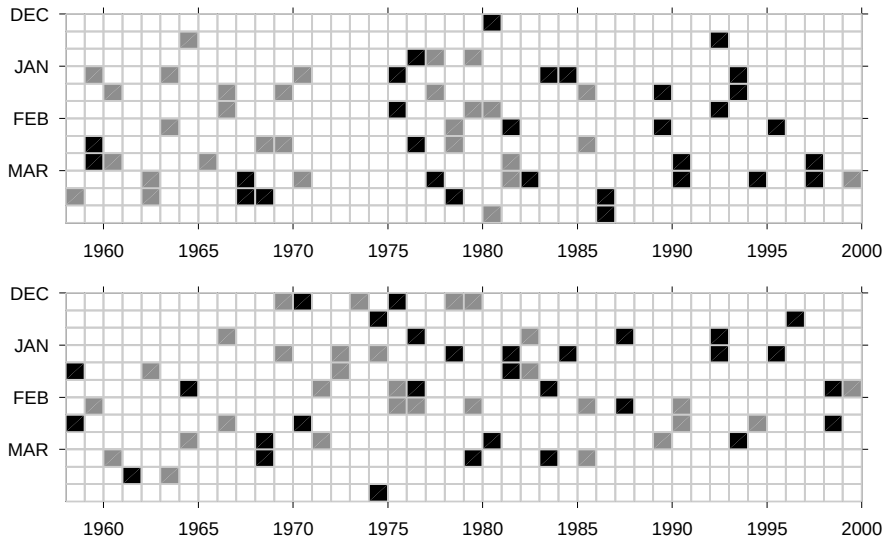

Figure 2.3: The dectads included in the "high index" (dark shading) and "low index" (gray shading). Upper panel PC1 and lower panel PC2.

used it to investigate temporal persistence of low-frequency flow patterns.

The analysis was performed on both consecutive (non-overlapping) 5-day and 10-day mean maps, both of which explicitly resolve most of the variability in the frequency range of interest, while averaging out the high frequency variability associated with baroclinic waves. The results for the two averaging intervals proved to be quite similar in most respects, so for the sake of brevity, only those for the latter are shown. No attempt is made to formally separate the variability into low- and intermediate frequency ranges. Data exclusively representative of the low frequencies (i.e., monthly mean data) are used only in the definition of the principal low-frequency patterns of variability.

2.2.1 "Spaghetti diagrams" as a tool for describing the flow variability

In this introductory example we show that spaghetti diagrams can depict changes in variability among prescribed subsets of data; in this case the stratification criterion

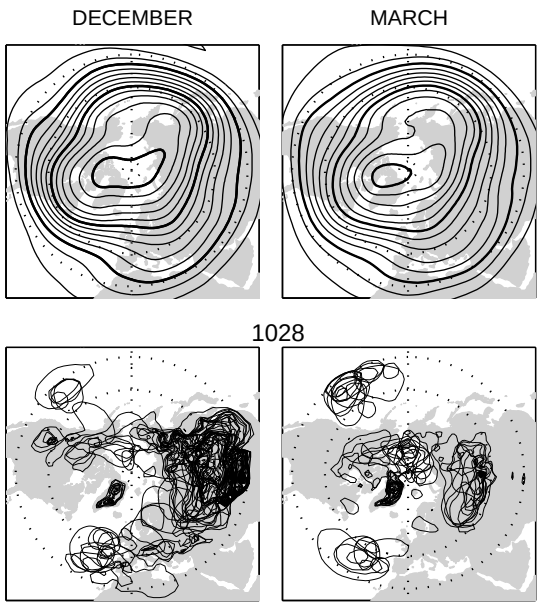

Figure 2.4: Mean 500 hPa height charts (upper panels) for the 42 maps of the 10-day means corresponding to December 1-10 and March 21-30, as indicated. Lower panels: "spaghetti plots" of the 1028 hPa contour for the same subsets as upper panels. Contour interval in upper panels: 60 m; the 5100, 5400 and 5700 m contours are bold.

is based on the climatological evolution within the winter season. The upper panels of Fig. 2.4 show the mid tropospheric average flow for early and late winter, as defined by December 1-10 and March 21-30, over the period 1958-99. In early winter, the meridional pressure gradient around 45°N is tighter over most longitudes, with the exception of the Asian continent. The variability at the surface, as exemplified by location and shape of the 1028 hPa contour, indicative of strong anticyclones, appears to be quite different in the two subsets, especially over Eurasia. This example illustrates that the variability of the flow significantly varies with different mean states, and introduces the use of "spaghetti diagrams" to picture these changes. In chapter 5 the same technique will be used on subsets based on extreme values of the two SLP PCs.

2.3 Stratification of data based on the polarity of the ENSO cycle

For the analysis presented in chapter 6, the data for the 42 year record were partitioned into warm and cold composites of the ENSO cycle based on winter averaged values of the "cold tongue index" (CTI), each containing 14 winters as documented in Fig. 2.5. The CTI is defined as the SST anomalies (relative to the 1950-1979 climatology) averaged over the area 6°N-6°S, 90°-180°W, computed after removing the global monthly mean, based on the Comprehensive Ocean-Atmosphere Dataset (COADS) described in Woodruff (2000).

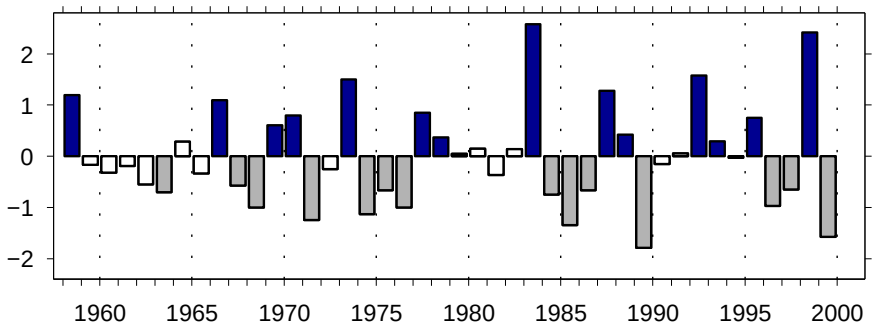

Figure 2.5: Time series of winter averaged values of the equatorial Pacific sea surface temperature "cold tongue index" for DJFM 1958-1999; The 14 warmest (blue) and 14 coldest (gray) seasons are shaded. Winters are labeled in terms of the year of January-March.

In order to more fully exploit the statistical degrees of freedom inherent in the data we made restricted use of 10-day running 30-day means, i.e. monthly means for 30-day intervals beginning Dec. 1, Dec. 11, Dec 21 ... . The running means are used in the EOF calculations and in all Monte Carlo testing, but all regression maps and profiles are based on consecutive 30-day means.

Besides primary fields from the NCEP-NCAR reanalyses, additional fields used are monthly fields of the variance of daily, 24-hour differenced meridional wind component at the 300 hPa level, kindly provided by K. M. Chang, State University of New York

at Stony Brook. For further details, see Chang and Fu (2002).

The various statistics presented in Chapter 6 (correlation coefficients, percentages of variance explained by the leading EOF, the difference between correlations in warm vs. cold composites, etc...) were compared with Monte Carlo simulations in which the data were sorted randomly into subsets consisting of 14 winters. The frequency of occurrence of the "event" in question by chance in 1,000 such random sortings, referred to as the "p-value", is indicated as appropriate. In applying this test, it is necessary to choose which of the random composites is to be labeled "warm" and which is to be labeled "cold". In all cases we made the selection that resulted in the larger p value: (i.e., in each of the 1000 randomized sortings, we identified "warm" and "cold" with the composites in which the structure of the NAM departed from its climatological-mean structure in the same sense as in the observed warm and cold years).

Chapter 3

THE TWO-DIMENSIONAL PHASE SPACE: MONTH-TO-MONTH VARIABILITY

3.1 Introduction

As outlined in chapter 1, it would simplify the climate dynamics literature if the plethora of existing patterns and their associated time series could somehow be distilled or at least placed in a common framework that would allow for systematic intercomparison. In this chapter we will show that many of the Northern Hemisphere (NH) extratropical wintertime patterns that have been identified project strongly upon the two-dimensional phase space defined by the leading empirical orthogonal functions (EOFs) of the monthly mean SLP field, here defined on the basis of winter (December through March) monthly data, 1958-1999. In a similar manner, the time varying indices of these patterns project strongly onto the leading principal components (PCs) of the SLP field.

This chapter is organized as follows. Section 3.2 describes the spatial and temporal "phase space" defined by the two leading EOFs of the wintertime monthly-mean sea-level pressure field and their associated principal component (PC) time series. Sections 3.3 and 3.4 document the linear relationship between a number of previously identified patterns in terms of their projections in space and time, respectively, upon these two-dimensional phase spaces. Section 3.5 compares the SLP EOFs with the EOFs of the geopotential height field at various levels. The next three sections extend the two dimensional phase space representation to the stratospheric quasi-biennial oscillation (section 3.6), to regimes identified in selected nonlinear analyses (section

3.7), and to model output data (section 3.8). In the attempt to associate dynamical mechanisms with directions of our phase space, in section 3.9 we show that EOFs of various other dynamically based fields (as kinetic energy and the eddy forcing terms) project strongly onto it. Section 3.10 illustrates how to apply the two dimensional phase space to describe the impacts of low frequency variability on regional scale variability of temperature and precipitation. Results are then discussed in section 3.11.

3.2 The SLP EOF1 - EOF2 phase space: definition

3.2.1 The two basis functions

The patterns chosen as basis for our two dimensional phase space correspond to the two leading EOFs of monthly mean DJFM SLP anomalies poleward of 20°N. Monthly 500-hPa height and SLP fields regressed upon their time series (PCs 1 and 2) were shown in Figure 2.1. Explaining 24% and 13% of the total variance of the field, respectively, these EOFs are well separated from one another by the criterion of North et al. (1982) and the second EOF is well separated from the third, which accounts for only 9% of the variance.

Based on the definition of Thompson and Wallace (1998), the first pattern corresponds to the Arctic Oscillation, referred to in subsequent papers as the Northern Hemisphere annular mode (NAM). The pattern formed by regressing the 500-hPa height field onto the second PC bears a strong resemblance to the Pacific-North American (PNA) pattern, defined in WG (area weighted correlation=0.88), and its associated PC time series is strongly correlated with the PNA-index (r=0.79). However, the 500-hPa pattern derived from the SLP PC2 is characterized by more prominent features over the North Atlantic and Eurasia than the pattern described by WG. The one-point Z500 regression map for its Pacific center of action (45°N, 165°W) exhibits weaker centers of action in those same regions (e.g., see Fig. 4 of Wallace and Thomp-

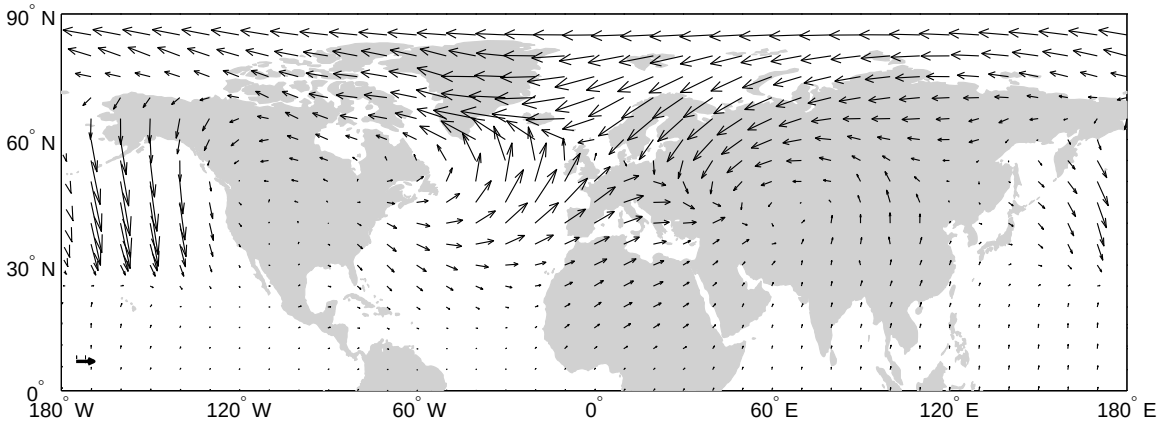

Figure 3.1: Vectorial representation of regression coefficients of monthly mean SLP upon PCs 1 (x-component) and 2 (y-component) of monthly DJFM SLP anomalies. The vector in the lower left corner corresponds to 3hPa per unit standard deviation of the PC time series.

son, 2002). A similar hemispheric pattern has been obtained by several authors using nonlinear analysis techniques: Mo and Ghil (1988) and Cheng and Wallace (1993) identified similar structures in their cluster analysis of low-pass filtered 500 hPa height anomalies (cluster W3, "wave number 3, including PNA"); Cheng and Wallace (1993) identified it as one of the three clusters of 500 hPa geopotential anomalies (their R cluster: "Rockies ridge"), and Molteni and Palmer (1990) as the first rotated EOF of 5-day averaged eddy 500-hPa height anomalies. To distinguish SLP EOF2 from WG's PNA pattern we will refer to it as the "PNA-like" pattern.

The polarity of EOF1/PC1 is chosen to be consistent with the usual sign convention of the NAM and the polarity of the PNA-like second EOF is consistent with that of WG's PNA pattern. For an overview of the relative contributions of the two patterns to the hemispheric SLP variability, Fig. 3.1 shows the SLP field regressed onto standardized SLP PCs 1 and 2, in a vectorial format. The lengths of vectors are proportional to the combined root mean squared amplitude of the SLP fluctuations attributable to the two patterns. The NAM is dominant over the Arctic and over the

subtropical Atlantic and Mediterranean while the PNA-like pattern is dominant over the Pacific sector as well as parts of the north Atlantic.

3.2.2 Methodology for spatial projections

To relate any given spatial pattern to our phase space, we calculate its area-weighted spatial correlations with EOFs 1 and 2, based on the region poleward of 20°N. An example is given for the pattern obtained as the regression of SLP upon the time series of SLP anomalies over Iceland (Fig.3.2, bottom left). For this index, the area-weighted correlation coefficients with EOFs 1 and 2 (whose patterns are also shown in the upper panels as a reference) are -0.94 and 0.18, respectively. The projection of the Iceland SLP pattern onto the phase space appears therefore as a vector close to the negative x-axis (bottom right).

Vectors that extend all the way out to the unit circle are indicative of spatial patterns that can be perfectly represented as "best-fit" linear combinations of EOFs 1 and 2 and hence lie within the same plane in multi-dimensional phase space as they do. The vector for the Iceland SLP time series extends almost all the way out to the unit circle (96% of the way, to be exact). Hence, to a very close approximation, this 1-point regression pattern lies within the phase space defined by EOF1 and EOF2 of the hemispheric SLP field.

3.2.3 Methodology for temporal projections

The same methodology can easily be applied to time series; in this case, the SLP PCs will be the basis functions, and the correlation coefficient will determine the projection of a given index upon this temporal phase-space.

Time series have often been defined as linear combinations of data at some particular locations –e.g. as in Wallace and Gutzler, 1981; the index comes first (therefore it can be described as "primitive") and the associated spatial pattern is derived from it by compositing or by performing linear regression.

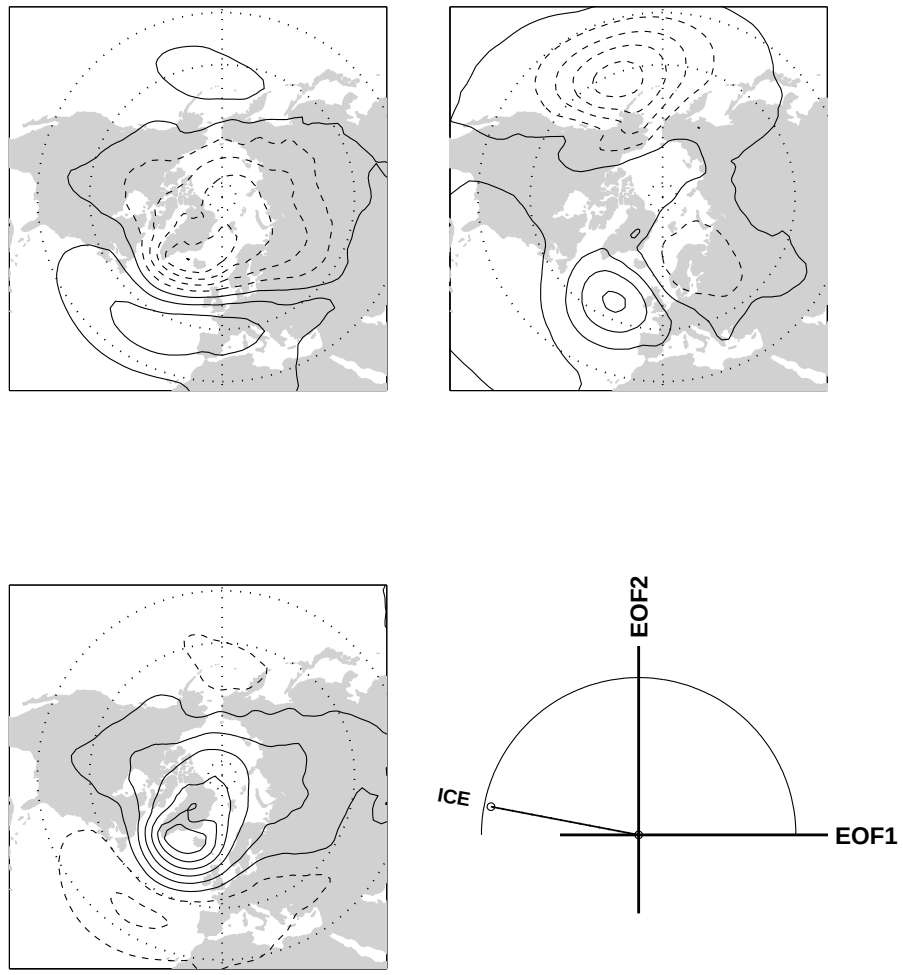

Figure 3.2: SLP regressed upon SLP PCs 1 and 2 (upper panels), and on the index of SLP anomalies over Iceland (ICE). Spatial phase space defined by EOF1 and EOF2 of monthly DJFM SLP anomalies for the period 1958-1999, with the projection of ICE. See text for further explanation.

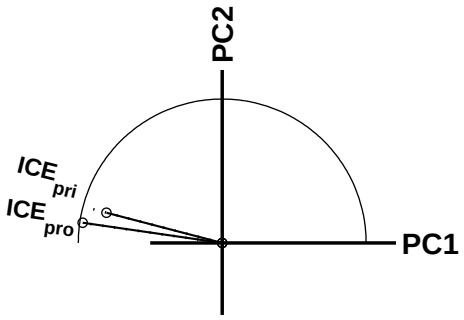

Figure 3.3: Temporal phase space defined by PC1 and PC2 of monthly DJFM SLP anomalies for the period 1958-1999, with the projection of the "primitive" and "projection" indices of Iceland SLP. See text for further explanation.

In analogy with Fourier analysis, the temporal variability of a prescribed spatial pattern $P(x)$ may be described also in terms of a "projection index" $I(t)$ formed by projecting the observed field $Z(x,t)$ onto the pattern, i.e.

$$I(t) = \int\int P(x) \cdot Z(x,t)\, dA \tag{3.1}$$

where A is area and the domain of integration is the Northern Hemisphere poleward of 20°N. Figure 3.3 shows both the "primitive" and the "projection" indices for the same Iceland SLP anomaly as in Fig. 3.2.

Projection indices and primitive indices are one and the same only for the special case of EOFs and PCs; the difference between these two categories of temporal indices will discussed in section 3.4.

3.2.4 Sampling errors

The orientation of the x and y axes in this two-dimensional phase space defined by the leading EOFs or PCs is subject to some degree of uncertainty due to the sampling variability inherent in a 42-year record. To characterize that uncertainty, we generated 1000 synthetic datasets and projected the leading EOF derived from each of them onto the two-dimensional phase space defined by EOF1 and EOF2 of

the observations. Results are shown in Fig. 3.4.[1] Based on the analysis of North et al. (1982) and the empirical results of Cheng et al. (1995) it is expected that most of the sample-to-sample variability in the structure of EOF1 will be due to mixing between EOFs 1 and 2. If this is, in fact, the case, then the points for the individual samples should tend to lie just inside the unit circle in Fig. 3.4 and, in fact, they do. The dispersion of the points about the x axis in this two-dimensional phase space is a measure of the sampling error in EOF1. The dots tend to lie along the unit circle, indicating that the leading EOFs of the subsets of the data tend to be linear combinations of the leading EOFs of the observed data. This tendency is especially strong for the first mode.

Based on these results, the standard error in the determination of the angle of EOF1 in this two-dimensional phase space is estimated to be 7°. Hence, EOFs separated by more than 14° (2 standard deviations) in this 2-dimensional phase space may be regarded as significantly different at the 95% confidence level.

This empirical estimate of the sampling error is in close agreement with the analytical estimate based on perturbation theory given in Appendix A.

3.3 Projections of spatial patterns

Figure 3.5 shows the area-weighted spatial correlations between EOFs 1 and 2 and the spatial patterns of SLP anomalies associated with selected patterns of variability, as indicated, within the domain poleward of 20°N. The vectors for the NAO and the PNA pattern extend nearly all the way out to the unit circle: they are correlated with

[1]The synthetic datasets were generated as follows. For each of the 168 observed PC time series, a random normal, first order autoregressive time series was generated, whose lag-1 month-to-month autocorrelation within a given winter matches that of the observed PC. (No attempt was made to match the observed winter-to-winter autocorrelation). EOF analysis was performed upon the synthetic dataset consisting of 168 randomly varying PCs, and the leading EOF was projected (using area-weighted spatial correlation coefficients) onto the phase space defined by EOF1 and EOF2 of the observations. In other words, for each of the points in Fig.3.4, the *x(y)* axis represents the spatial correlation between EOF1 (EOF2) for that sample and EOF1(EOF2) of the observations.

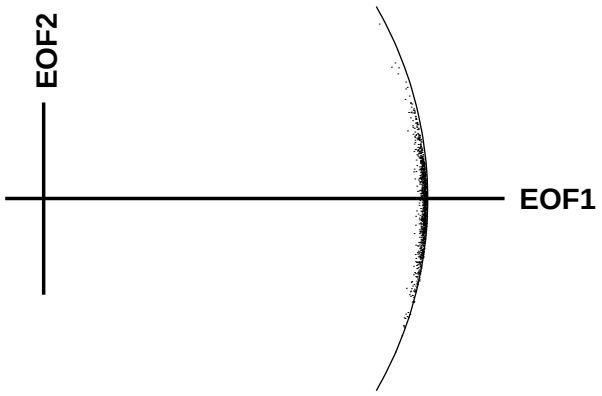

Figure 3.4: Phase space defined by EOF1 and EOF2 of monthly DJFM SLP anomalies for the period 1958-1999. The cloud of dots represents projections of the leading EOFs of 168-month datasets derived from Monte Carlo experiments, as defined by their correlation coefficients. The dots lie just inside the circle of unit radius. See text for further explanation.

the respective "best-fit" linear correlations of EOFs 1 and 2 at levels 0.99 and 0.93, respectively. These strong correlations, together with the near orthogonality of the NAO and PNA vectors is consistent with the interpretation in Ambaum et al. (2001) and Wallace and Thompson (2002) in which the NAO/PNA and the NAM/PNA-like pattern paradigms are viewed as alternative representations of the dominant modes of variability of the Northern Hemisphere wintertime circulation. The two pairs of coordinate axes differ by 15-22°, depending on whether the NAO or PNA is used to define the NAO/PNA coordinate system. The separation between the EOF1/EOF2 axes and the NAO/PNA axes is significant in terms of the criterion discussed at the end of the previous section.

The configurations of the vectors in Fig. 3.5 resemble the schematic shown in Fig. 1.7 from Wallace and Thompson (2002), but rotated clockwise so that EOF1 rather than the NAO coincides with the x axis. The 15° counterclockwise rotation of the NAO relative to the x axis is just sufficient to eliminate the weak Pacific center of action in EOF1, leaving a sectoral North Atlantic pattern. In a similar manner,

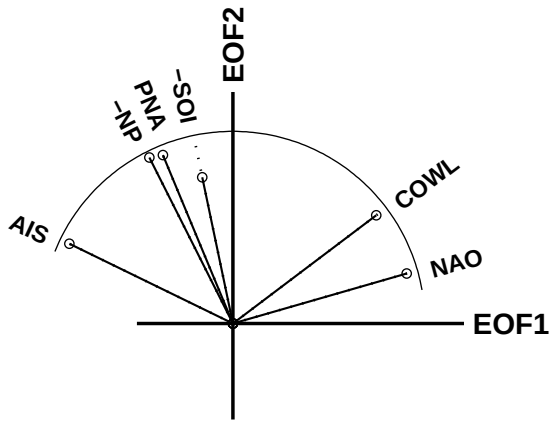

Figure 3.5: Projections (area-weighted spatial correlations) of patterns associated with various indices on the phase space defined by the two leading EOFs of monthly DJFM NH SLP anomalies, north of 20°N. For reference, a circle of unit radius is shown in the plots. Positive values of the EOFs denote polarities indicated in Fig. 1.

the counterclockwise rotation of the PNA pattern relative to the y axis weakens the Atlantic / Eurasian wavetrain in EOF2, but in this case the cancellation is incomplete (i.e. the PNA pattern as defined in WG lies slightly outside this two-dimensional phase-space). The SLP regression pattern for Trenberth and Hurrell's (1994) North Pacific SLP index, the area-weighted sea level pressure over the region (30°N-65°N, 160°E-140°W) which corresponds to the region covered by the climatological mean Aleutian Low, lies closer to the phase space: it is correlated with the best fit linear combination of EOF1 and EOF2 at a level of 0.97 compared to 0.94 for the pattern derived from WG's PNA-index. The spatial patterns of both SLP and 500-hPa height defined by WG's PNA index and Trenberth and Hurrell's North Pacific SLP index are correlated with one another at a level of 0.97. Hence, it is clear that the two indices are representing the temporal variability of the same three-dimensional pattern.

Vectors that lie within the first quadrant in Fig. 3.5 denote polarities of EOFs 1 and 2 in the same sense as in Fig. 1, commonly referred to as the "high index" polarity. Angles between the NAO and PNA vectors are indicative of anomalously strong

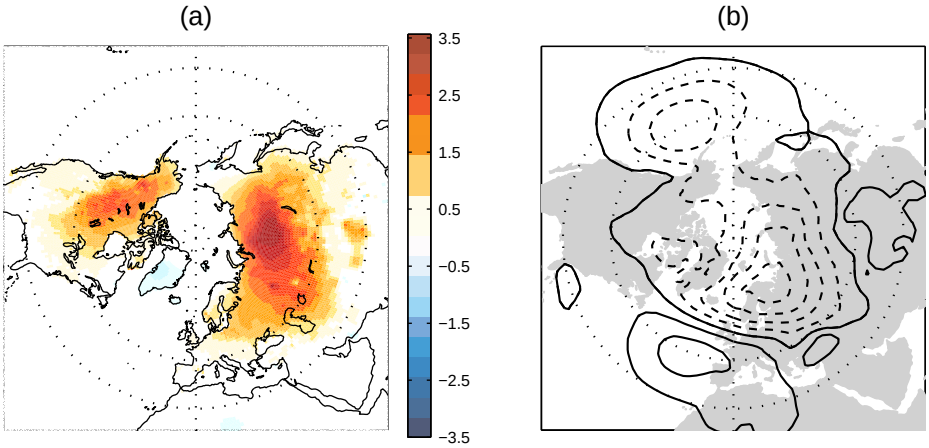

Figure 3.6: Surface air temperature (a) and sea level pressure (b) regressed upon an index of hemispheric mean land surface air temperature. SLP contour interval 1 hPa; negative contours are dashed.

Icelandic and Aleutian lows. Angles in the quadrants extending counterclockwise from the PNA and clockwise from the NAO are indicative of a negative correlation or "seesaw" between the depth of the Icelandic and Aleutian lows. The Aleutian-Icelandic seesaw (AIS) investigated by Honda and Nakamura (2001), Honda et al. (2001) lies nearly entirely within this phase space, at angles (150°, −30°).

The SLP signature of the Southern Oscillation, obtained by regressing SLP poleward of 20°N upon the time series of the Southern Oscillation index (SOI), does not project as strongly upon EOFs 1 and 2 of the monthly data as the other patterns considered in this section do.

The "cold land - warm ocean (COWL) pattern", defined by regressing SLP onto the monthly time series of hemispheric mean land temperature (Wallace et al., 1995), is correlated with the best fit linear combination of EOFs 1 and 2 at a level of 0.93. The orientation of the COWL pattern, near the middle of the first quadrant in Fig. 3.5, is consistent with the observed tendency for the Icelandic and Aleutian lows to be deeper than normal during those months in which hemispheric mean temperature

is abnormally warm. These relationships are clearly evident in maps of SAT and SLP regressed upon hemispheric mean land SAT, shown in Fig. 3.6.

3.4 Projections of time series

Figure 3.7a shows the temporal correlations between the projection indices and PC1 and PC2 of the SLP field in a vectorial format. The angles and lengths of the vectors are comparable to those for the spatial correlations shown in the previous figure. That the correlations are very close to 1 implies that the time variability of these patterns can be well represented by linear combinations of PC1 and PC2 of NH SLP.

Many of the patterns in the climate dynamics literature are defined on the basis of "primitive indices". For example, the NAO, the PNA pattern and the Southern Oscillation are defined on the basis of station or gridpoint data at specified locations; the NP and AIS are based on SLP averaged over specified regions; the COWL SLP pattern is formed by projecting the SLP field onto the time series of hemispheric mean land temperature. The correlation coefficients between an expanded set of primitive indices and the leading PCs of the SLP field are shown in Fig. 3.7b. The angles for the primitive indices are very similar to those for the respective projection indices, but the correlations with PC1 and PC2 are generally weaker, either because the primitive indices are based on highly simplified representations of the patterns (as in the case of the NAO, PNA, and AIS), or because they are only indirectly related to the NH SLP field (as in the case of the COWL pattern).

The relationship between the PNA pattern defined by WG and the NP index defined in Trenberth and Hurrell (1994) provides an example of the subtle, but sometimes important distinctions between projection indices and primitive indices. Both patterns are defined on the basis of their primitive indices, which are correlated with one another at a level of 0.86. The corresponding projection indices based on their

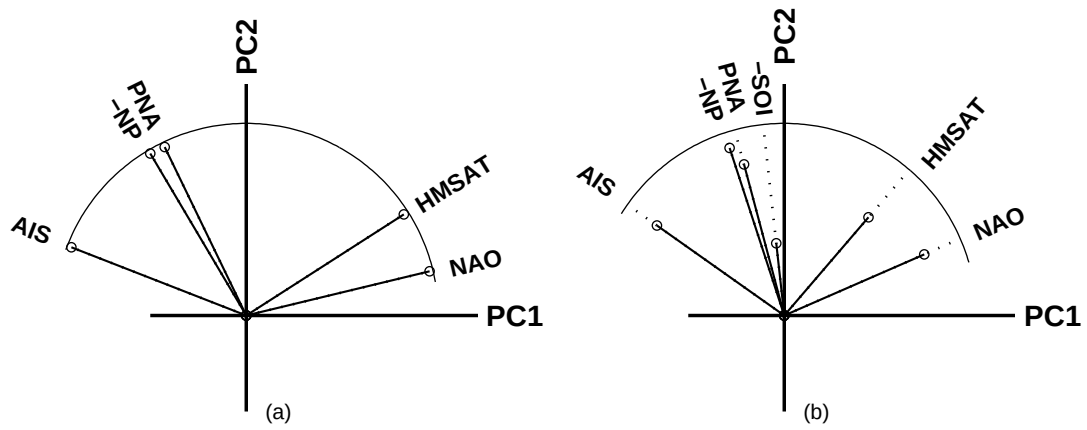

Figure 3.7: Projections of various indices on the phase space defined by the two leading PCs of monthly DJFM NH SLP anomalies. a) temporal correlations of projection indices and b) temporal correlations of primitive indices with the SLP PCs. Positive values of the PCs denote polarities indicated in Fig. 1.

SLP patterns are correlated with one another at a level of 0.99. Hence the primitive indices do not fully reflect the almost complete redundancy between the patterns whose variability they are designed to represent.

To investigate whether the primitive indices contain any information concerning spatial patterns of SLP variability that is linearly independent of the leading EOFs we formed residual time series, from which the variability associated with PC1 and PC2 was removed by a least squares best fit. Results for the NAO and PNA indices are shown in Fig. 3.8. The negative center of action over Scandinavia in the pattern for the NAO residual index indicates that the isobars in the pattern based on the primitive index curve more cyclonically over that region than the isobars in the NAO as represented in the 2D phase space. The negative center over the North Atlantic in the pattern based on the WG PNA residual index reflects the failure of the WG PNA index to capture the negative correlations between geopotential height in the Pacific and Atlantic sectors. With the exception of these regional features, regression maps based on the primitive indices and the best fit linear combinations of PC1 and PC2

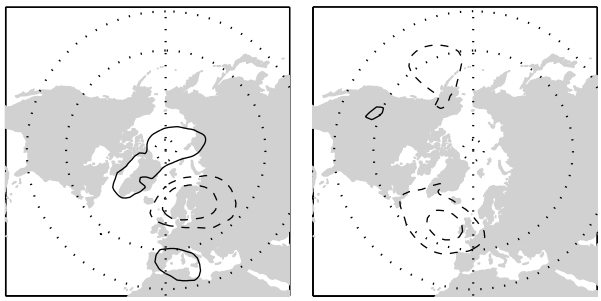

Figure 3.8: Monthly mean SLP fields regressed on residual time series formed by subtracting from the primitive indices of NAO (left panel) and PNA (right panel) the variability associated with PC1 and PC2. See text for further explanation. Contour interval 1.5 hPa; negative contours are dashed.

are virtually identical.

Primitive indices are of interest because relatively long time series of data are available only at specific locations, corresponding to observing stations or proxy records; however, projection indices are the optimal indicators of the temporal variability of the patterns. Whenever reliable gridded data are available for constructing them, the projection indices, which incorporate information from the complete gridded fields, offer a more faithful representation of the time variability of the patterns.

3.5 Projections of EOFs of the geopotential height field

The leading EOFs and PCs of geopotential height on various pressure levels also bear a close relationship to the two leading SLP patterns. Figure 3.9 shows relationships between the two leading EOFs and PCs of the 500 and 50-hPa height field and the first two SLP EOFs/PCs. The 500-hPa height PCs are strongly correlated with the SLP PCs, but when projected onto the phase space of SLP PCs they are rotated clockwise by an angle of $\sim 25^{\circ}$. The pattern obtained by regressing SLP onto the leading PC of 50-hPa height is virtually identical to the leading EOF of SLP, but the temporal correlation coefficient between the corresponding PCs is, of course, much

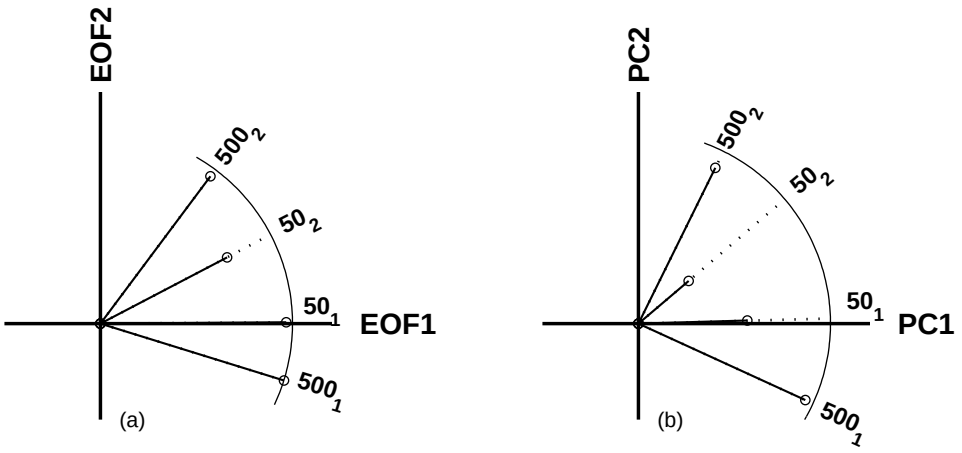

Figure 3.9: As in Figs. 3.5 and 3.7 but for the leading EOF/PCs of 50- and 500-hPa height, as indicated.

weaker.

The subtle changes in the PCs of the geopotential height field from level to level are documented in more detail in Fig. 3.10. Panel (a) shows the clockwise rotation of the leading PC of middle and upper tropospheric geopotential height relative to PC1 of SLP.

Panel (b) shows the relative prominence of the leading EOFs at each level. The fraction of the variance explained by the leading PC is generally higher in the stratosphere than in the troposphere, and it exhibits a distinct minimum in the middle to upper troposphere. It is evident from the figure that the level-to-level differences in the fraction of variance explained by EOF1 are not a reflection of a tradeoff of variance among the leading EOFs. Rather, they are suggestive of a greater complexity of the anomalies in the middle and upper tropospheric geopotential height field compared to those in the SLP and stratospheric geopotential height fields; i.e., the larger number of spatial degrees of freedom.

Consistent with the smaller fraction of the variance explained by the leading EOF of the 500-hPa height field compared to that of the SLP field, the rms error in the

angle of the x axis in the two-dimensional phase space was found to be larger in the Monte Carlo test described in Section 3.2 (17° versus 7°). This result is consistent with the large sampling variability of the 500-hPa height EOFs reported by Cheng and Wallace (1993) (their Fig. 2).

Figure 3.10c shows the fraction of the geopotential height variance at each level that is explained by PCs 1 and 2 of SLP. In combination, the two SLP PCs explain ∼30% of the geopotential height variance at levels all the way up to 100-hPa. Note the secondary maximum in the fraction of the variance explained by SLP PC1 at the 100-hPa level.

Figure 3.10d shows spatial and temporal correlation coefficients between the leading EOF/PC of the geopotential height field at each level and the least squares best fit of the two leading EOF/PCs of the SLP fields. The spatial correlations are nearly perfect at all levels. The temporal correlations decrease monotonically with height, remaining quite strong throughout the depth of the troposphere, and declining more rapidly with height in the lower stratosphere.

3.6 The tropospheric response to the QBO

Thompson et al. (2002b) showed that the stratospheric quasi biennial oscillation can induce a surface signature which projects upon the structure of the annular mode. Here we extend this result, considering a two degrees of freedom definition of the QBO.

As in Wallace et al. (1993), the evolving state of the QBO is represented in terms of a vector rotating in the two-dimensional phase space defined by the standardized leading PCs of the equatorial stratospheric zonal wind profile, as computed from standardized time series of 10, 15, 20, 30, 40, 50 and 70 hPa monthly zonal wind anomalies. This vectorial representation can be understood as follows. When a westerly regime first becomes established at the 10-hPa level while easterlies remain strong at the 50 and 70-hPa levels, PC1 exhibits peak (by definition, positive) values and the phase

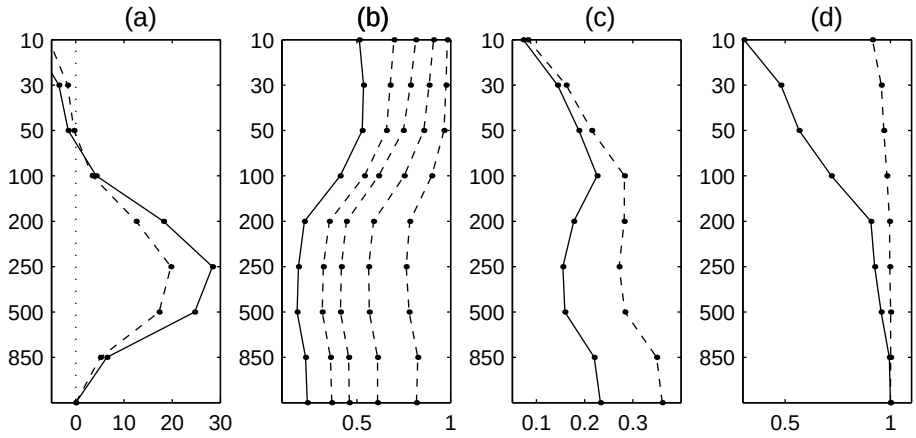

Figure 3.10: Leading EOFs of the geopotential height field at 10 vertical levels. (a) Clockwise angle (degrees) from the x axis of the phase space of Fig. 3.5 defined by the leading mode at each level (temporal phase space solid, spatial phase space dashed). (b) Fraction of the variance explained by the first, the first two, the first three, the first five and the first ten EOFs at each level. (c) Fraction of the variance of monthly mean of geopotential height at each level explained by the leading SLP modes solid SLP PC1, dashed SLP PC1+PC2). (d) Correlation between the best fit linear combination of the two leading SLP EOF/PCs and the first EOF/PC at each level (temporal solid, spatial dashed).

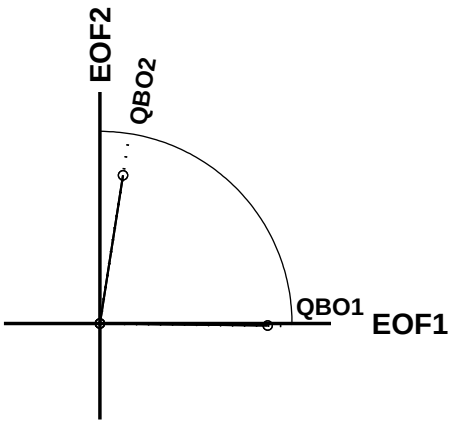

Figure 3.11: As in Fig. 3.5, but for the two leading EOFs of monthly anomalies of stratospheric equatorial wind which define the state of the QBO.

vector points in the positive direction along the x axis. During the next 6-7 months, while the westerly wind regime is propagating downward to near the 30-hPa level, the vector rotates counterclockwise through 1/4 cycle until it points upward, in the positive direction of PC2.

Figure 3.11 shows the patterns of the SLP pattern induced by the QBO, projected upon the two-dimensional phase space defined by PCs 1 and 2 of SLP. It is evident that the induced SLP patterns project strongly on the phase space of EOFs 1 and 2 of SLP. PC1 of the QBO induces a NAM-like SLP response, and PC2 induces a more PNA-like response. As the phase angle of the QBO rotates counterclockwise, the angle of the tropospheric response rotates counterclockwise in SLP phase space. Hence, for example, as a westerly regime descends, the SLP response evolves from a NAM-like pattern in the positive polarity to a more PNA-like pattern in its positive polarity, and subsequently to a NAM-like pattern in its negative polarity, etc.

Although the SLP patterns induced by the QBO are almost perfect replicas of the SLP EOFs, it should be noted that the temporal correlations between the QBO and SLP PCs in the monthly data are quite modest: (0.18 and 0.16, respectively for PCs 1 and 2). If the PCs are averaged over winter (DJFM) seasons, the correlations between

the individual PCs rise to 0.25 and 0.19. The corresponding multiple correlation (0.31), calculated by applying the Pythagorean theorem to the seasonal correlations, is a measure of the skill of QBO PC1 and PC2, in combination, in predicting the state of the SLP field, as defined by its two leading PCs. The ENSO-related correlations are much higher: the equatorial Pacific "cold tongue index" is correlated with DJFM means of PC2 of monthly (wintertime) mean SLP at a level of 0.46 (0.55).

3.7 Representation of non linear regimes

We have shown that the two-dimensional phase space described by the combination of the SLP EOF1/PC1 and EOF2/PC2 is equivalent to the phase space based on the leading two EOFs/PCs of any other level in the troposphere, even if their respective axes are rotated with respect to each other (as shown in Fig. 3.9, for the 500 hPa level). Most of the non linear analysis studies (see section 1.1.3) identify regimes after reducing the extratropical variability to that represented by the leading two EOFs/PCs of a given tropospheric level (e.g. 500 hPa). Some of the studies that do not use a priori this assumption find that their resulting clusters end up fully projecting onto the same two-dimensional phase space.

Therefore, the two-dimensional phase space identified by the leading SLP EOFs/PCs is also able to represent most of the non linear regimes identified in literature.

3.8 Representation of model output data

The methodology described in this chapter is also well suited for assessing and comparing the performance of climate models with regard to their ability to simulate the naturally occurring patterns of climate variability. For example, Fig. 3.12 shows the projection of the leading EOFs of the DJFM NH SLP anomalies of two WACCM runs forced by observed SSTs onto the phase space defined by the corresponding EOFs of observed data. The two runs differ only with respect to the initial conditions. Both

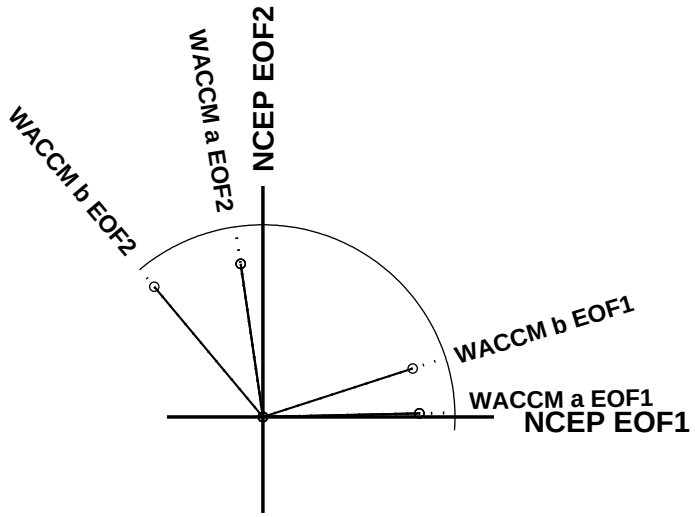

Figure 3.12: Projections of the two leading EOFs of DJFM NH SLP monthly anomalies of two WACCM runs on the phase space defined by the corresponding EOFs of the NCEP data (1958-1999).

pairs of patterns exhibit correlations of ∼0.8 with linear combinations of the observed EOFs. They also exhibit comparable fractions of the variance of the hemispherically averaged monthly SLP as their observational counterparts. (23% and 26% vs. 24% for EOF1; 13% and 12% vs.13% for EOF2). Analogous statistics for an array of models (or model runs) would provide a useful overview of the relative prominence and degree of realism of the most important patterns of simulated variability. A comparison of the simulated structures with the observed EOFs can be therefore a useful tool to test the degree of similarity between internal or forced variability of GCMs and observations.

3.9 Some dynamical diagnostics

In Molteni et al. (1988) the leading EOFs of the eddy component of the 500-hPa height field are used as basis functions. In contrast to the leading EOF of the total 500-hPa height field, the leading EOF of the eddy field shown in Fig. 3.13, lies in the

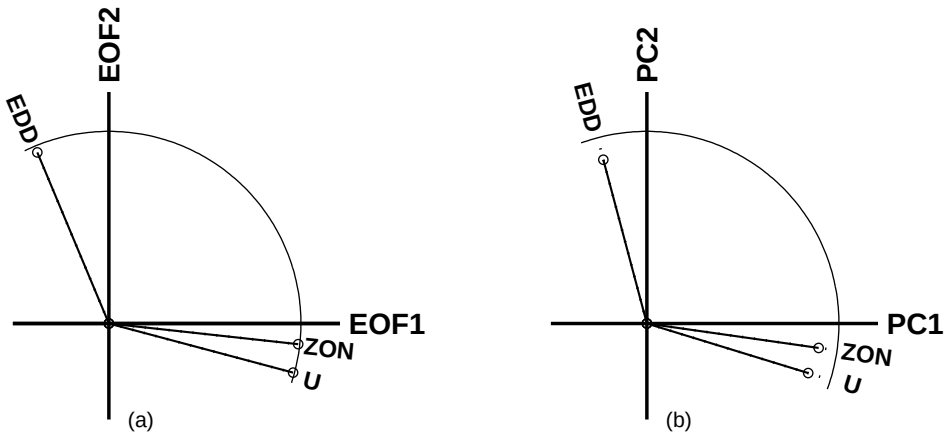

Figure 3.13: As in Fig. 3.5, but for the leading EOF of the zonal and eddy component of the 500 hPa field, and for the leading PC of vertically and zonally averaged zonal wind (U) as defined in Lorenz and Hartmann (2003).

second quadrant, in virtually the same direction as the PNA pattern in Fig. 3.5. The PC time series of this pattern is well correlated with WG's index of the PNA pattern (r = 0.81). Not surprisingly, the leading PC of the zonally symmetric component of the 500-hPa height field lies close to the x axis (i.e., the NAM), as does the leading PC of vertically and zonally averaged zonal wind as defined in Lorenz and Hartmann (2003).

The analysis presented so far is purely statistical; however, it appears that the two directions of our phase space can be associated with the two different dynamical processes described in section 1.2: baroclinic wave/mean flow interaction along the x-axis and barotropic instability of the zonally asymmetric flow along the y-axis. Here we show that the NAM and a PNA-like mode also emerge as leading modes when considering fields of other atmospheric variables like the fluxes of zonal momentum. As discussed in section 1.2, the annular mode is associated with zonal wind dynamics and maintained by high frequency transients, while the PNA pattern arises from barotropic instability of the zonally varying climatological mean flow. We chose therefore to compute the leading EOF of monthly anomalies of the concatenation of two

components of the horizontal **E** vector, as defined in Hoskins et al. (1983): $\overline{v'^2} - \overline{u'^2}$, and $\overline{u'v'}$. Basically, $-\mathbf{E}$ can be viewed as the effective horizontal flux of zonal momentum through the atmosphere, due to the transients. The first term acts in the presence of horizontal variations of $\overline{u}$, or meridional variations of $\overline{v}$, as in the case of barotropic instability which is responsible for the existence of the PNA pattern. The second term is responsible for energy conversion in the presence of meridional gradients of $\overline{u}$ (i.e. a jet), therefore is important in the zonal index dynamics, especially based on baroclinic eddy feedback. To highlight the contribution of baroclinic eddies we apply a high pass filter to u' and v' before computing monthly means of **E**, whereas for the low frequency component we directly use monthly mean values of u' and v'. Fig. 3.14 shows the mid tropospheric signatures of EOF1 for the monthly averaged high frequency[2] and for the monthly mean concatenated components of $\mathbf{E}$[3], explaining 7.8% and 21.5% of variance of the respective fields. As expected, we recover patterns similar to the annular pattern, and the PNA pattern, in association with the forcing of **E** deriving from the two different frequency ranges. From the horizontal momentum flux fields, we have obtained patterns that strongly project upon the phase space and closely match those of Fig. 3.13. Analogous results can be obtained for kinetic energy (Fig. 3.15), whose EOF1s explain 14% and 21% of the monthly averaged high pass and monthly mean detrended fields, respectively.

3.10 Regional climatic impacts

Our two-dimensional frame can be applied to describe the contributions of the large scale flow to the regional variability of temperature, precipitation, or other fields of interest to users.

In combination, the two leading SLP PCs account for substantial fractions of the

[2]The high pass filter is a 10-day high pass filter, as in Blackmon and Lau (1980).

[3]Both components were detrended before the EOF analysis, in order to remove the effect of the very long term variability.

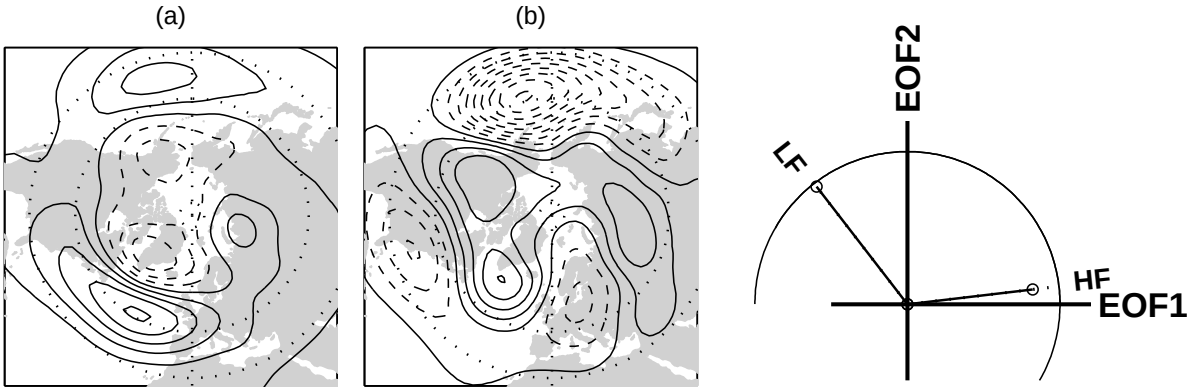

Figure 3.14: 500 hPa geopotential height regression maps of the leading EOF of the detrended 300 hPa (a) monthly mean high pass filtered (HF) and (b) monthly mean (LF) concatenated fields of $\overline{u'v'}$ and $\overline{-u'^2} + \overline{v'^2}$; their projection upon the SLP phase space. a, b: contour interval 10 m.

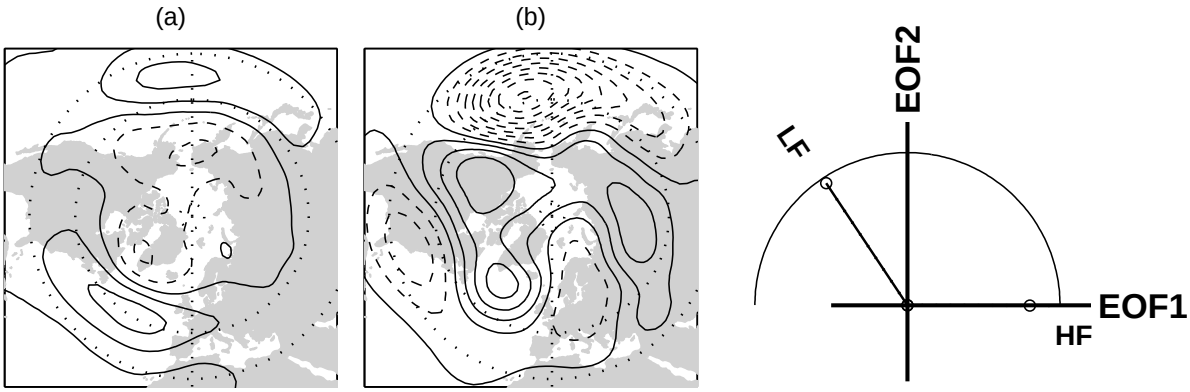

Figure 3.15: Same as Fig. 3.14, but for detrended kinetic energy $(u'^2 + v'^2)$. a, b: contour interval 10 m.

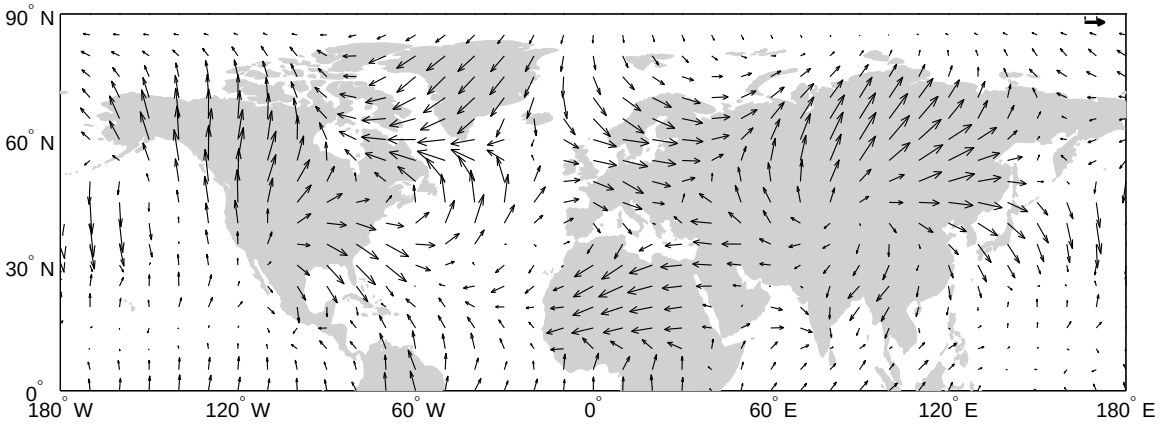

Figure 3.16: Vectorial representation of correlations between monthly mean 850-hPa temperature and PCs 1 (x-component) and 2 (y-component) of monthly DJFM SLP anomalies. The vector in the upper right corner represents a correlation coefficient of 0.5.

variance of winter monthly mean surface air temperature and precipitation throughout most of the NH. Lower tropospheric temperature (Fig. 3.16) is strongly correlated with PC1 over Europe, North Africa, parts of East Asia and the eastern United States and eastern Canada, and with PC2 over the high latitude oceans and western North America.

Precipitation (Fig. 3.17) exhibits a more complex pattern. For example, from the inset it is evident that over Scotland the high index of the NAO, which corresponds to an angle of $\sim 15^\circ$ in the phase space, is conducive to heavy precipitation, but along the east coast of England the relationship is weak and in the opposite sense. Trigo et al. (2002) observed a similar relationship for cloud cover. In the south of England and Ireland the negative polarity of EOF2, which favors an anomalous southerly flow, is dominant. Some of this regional variability is attributable to the structure of the SLP EOFs, but part of it represents a response to more regional terrain features. Westerly wind anomalies, as observed in association with the high index polarity of the NAO, favor enhanced precipitation over England, with the notable exception of the low lying

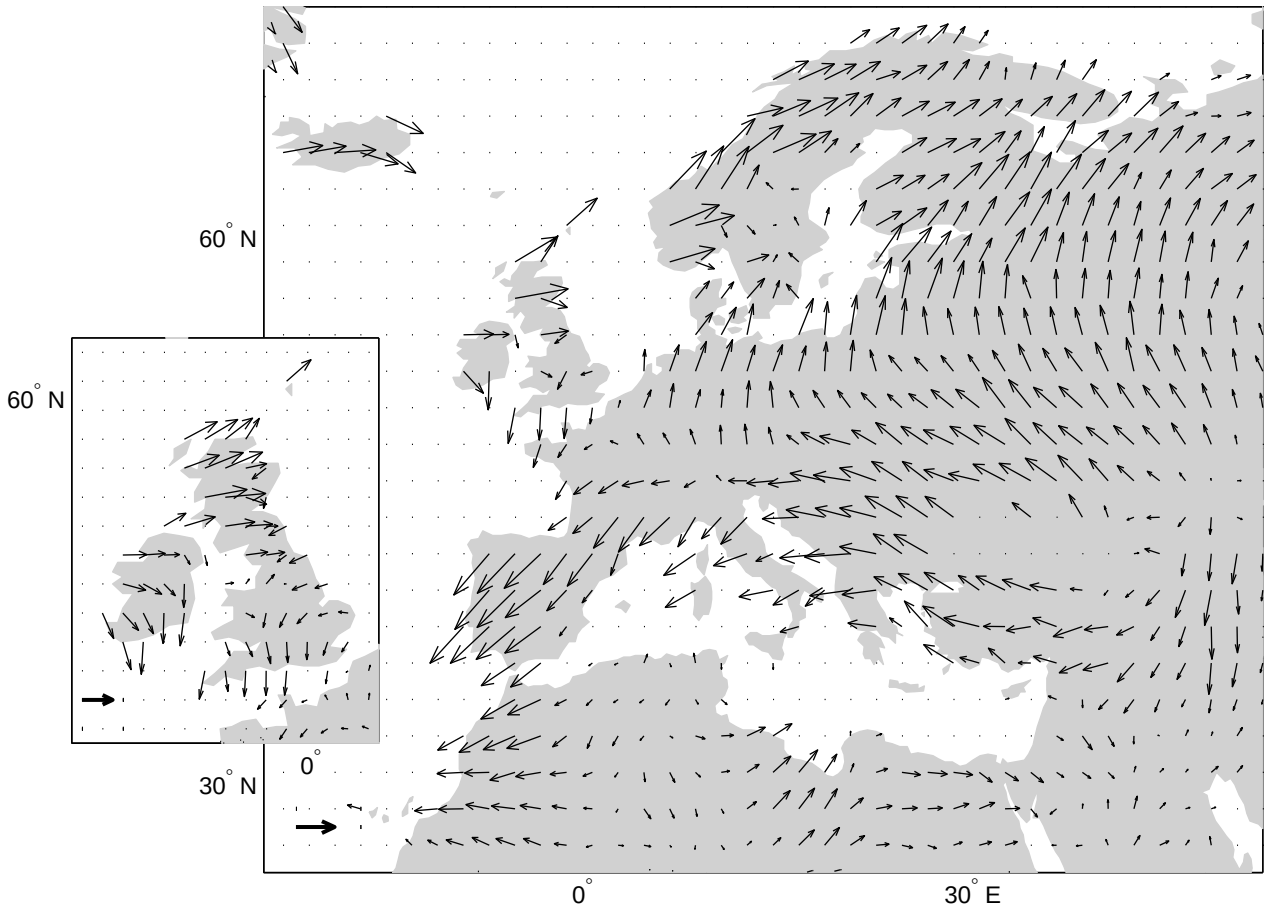

Figure 3.17: Vectorial representation of correlations between monthly mean SLP PCs 1 (x-component) and 2 (y-component) and monthly precipitation anomalies over Europe (2°x2°), and British Isles at a higher resolution (1°x1°). The vector in the lower left corner corresponds to a correlation coefficient of 0.5.

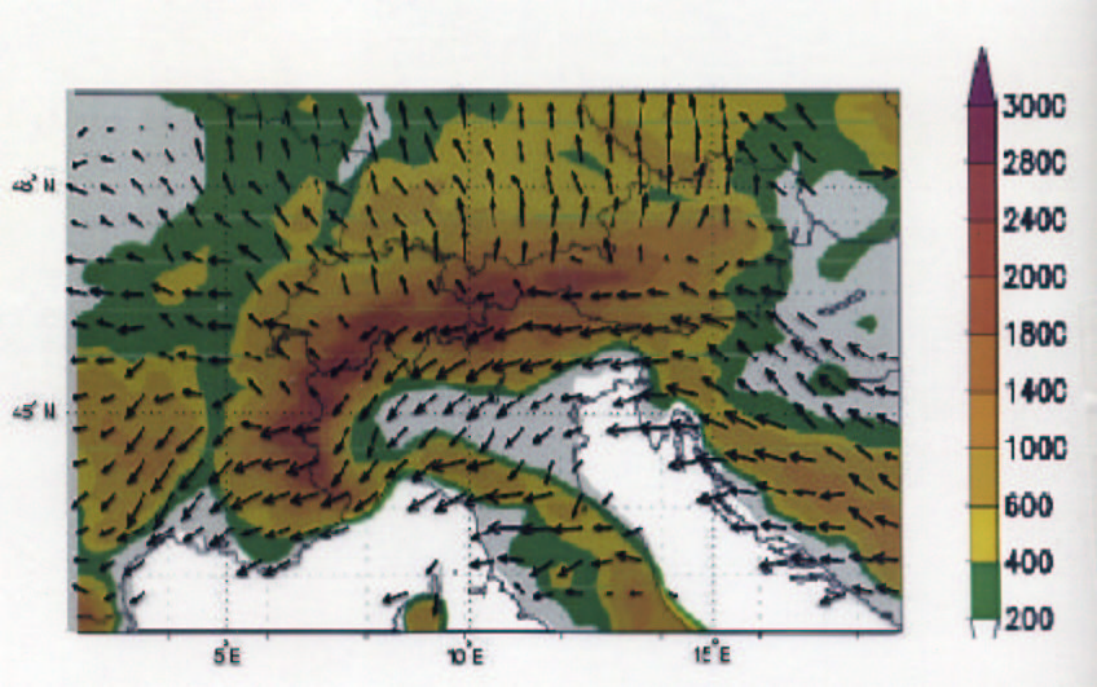

Figure 3.18: As in Fig. 3.17 but for precipitation over the region of the Alps for DJFM 1971-1992 based on the Frei and Schär dataset (here presented at the resolution of 0.6°x0.42°). The vector in the upper right corner corresponds to a correlation coefficient of 0.5.

eastern coastal region, where easterly rather than westerly wind anomalies favor above normal precipitation. The strong gradients across the Alps and Scandinavia in the larger figure are also indicative of terrain induced fine structure that is more clearly revealed in regional maps. An example is presented for the region of the Alps, using a very high resolution dataset. This region, extending from 42 to 50°N, and from 2 to 19 °E, is characterized by a complex orography, and is represented by just a few gridpoints of the Reanalysis. Figure 3.18 shows the clear and distinctive signature of the interaction of the regionally complex orography with the large scale flow. Several subregions show in fact quite different linear relationships between the SLP PCs and local precipitation. Analyses of this kind are advantageous when models (especially climate models) lack the ability to properly simulate the small scale features of the

terrain.

3.11 Discussion

The main message of this chapter is that a significant fraction of the structure inherent in the variability of the NH wintertime geopotential height, temperature, and precipitation fields on monthly time scales can be represented in terms of just two planetary-scale patterns. Depending upon how these two patterns are juxtaposed at any given time, the associated SLP and SAT patterns can assume a variety of forms, as illustrated in Fig. 3.19. For example, phase angles near 45°/225° denote a strengthening or weakening of the Icelandic and Aleutian Lows accompanied by anomalous warmth or coolness over both Eurasia and North America poleward of 40°N; angles near 135°/315° denote a "seesaw" between the intensities of the two lows accompanied by anomalous warmth of one continent and coolness of the other; angles near 0°, 90°, 180° and 270° denote more regional patterns, with SLP anomalies focused on a single ocean and the associated SAT anomalies over the downstream continent. On the basis of linear combinations of these two patterns it is possible to reconstruct the SLP patterns associated with the NAO, PNA, AIS teleconnection pattern, and the COWL pattern. Although the structure of the two leading EOFs of the geopotential height field varies with height, these changes are principally due to rotation of the patterns within a common two-dimensional phase space; i.e., the leading EOFs at different levels are linear combinations of the same two basic patterns. The two leading SLP PCs account for over 90% of the variance of the two leading geopotential height PCs at levels up to 500 hPa and over 80% at levels up to 200 hPa.

The SLP patterns associated with the leading PC of other fields than geopotential height can also be represented in the two-dimensional phase space. The spatial pattern derived by projecting the SLP field onto the time series of PC1 of lower tropospheric temperature (850 hPa) is almost identical to the pattern of SLP EOF1.

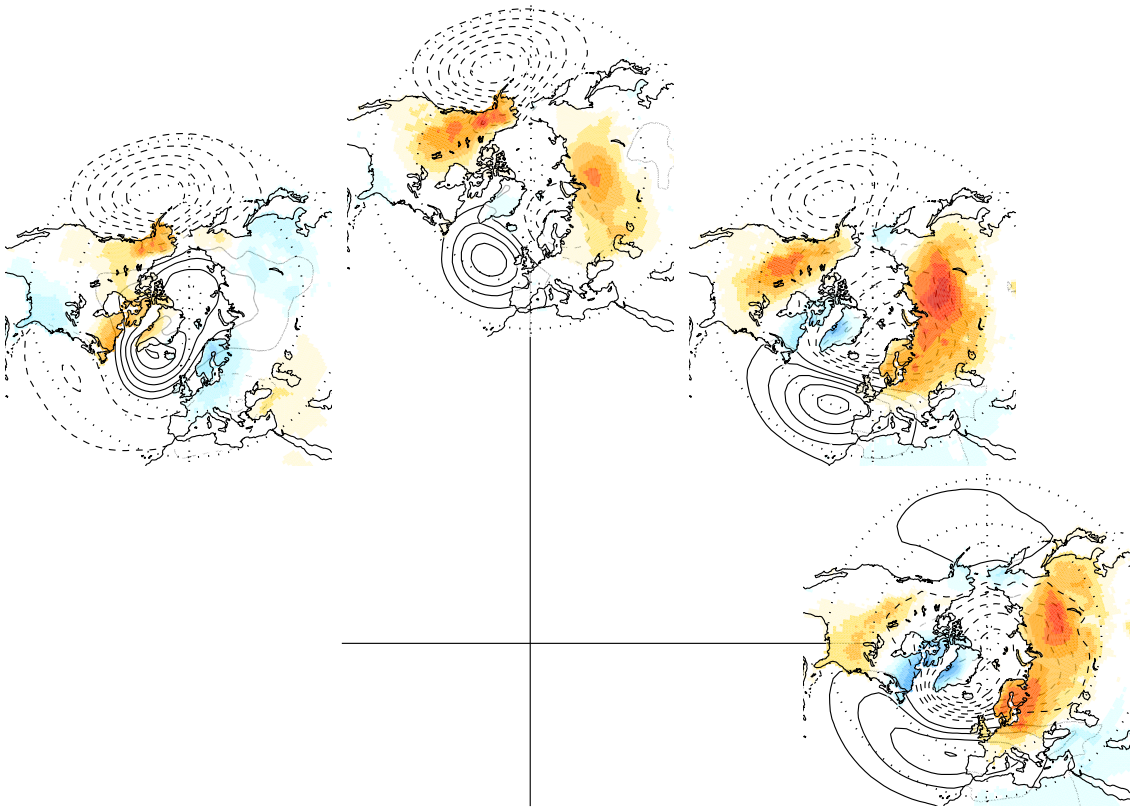

Figure 3.19: SLP (contours) and SAT (shading) patterns associated with one standard deviation anomaly of the time series of the linear combinations of SLP PC1 and PC2 corresponding to angles of 0°, 45°, 90° and 135° with the SLP PC1 axis. SLP contour every 1hPa, SAT shading every 0.4 degree C; warm colors indicate positive anomalies.

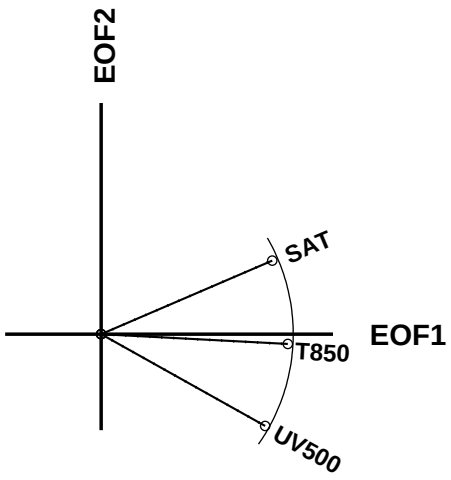

Figure 3.20: Projections (area-weighted spatial correlations) of patterns associated with the leading EOF of SAT, T850, and the concatenated fields of 500 hPa u and v, with the phase space defined by the two leading EOFs of monthly DJFM NH SLP anomalies, north of 20°N.

The SLP patterns corresponding to the leading PC of surface air temperature and to the concatenated u and v components of the 500 hPa wind project almost perfectly onto the phase space as well. These relationships are documented in Fig. 3.20. The correlation coefficient between the time series of temperature and wind PC1 and their respective best fit linear combination of SLP PC1 and PC2 are 0.82 and 0.89, respectively.

The results presented in section 3.6 have practical implications for seasonal to interannual climate prediction. The influence of the QBO (as represented by 50-hPa zonal wind) on PC1 of SLP (i.e., the NAM) has been pointed out by Baldwin et al. (2001), and the implications for wintertime climate prediction have been discussed by Thompson et al. (2002b). We have shown that indices of the QBO also exhibit some skill in predicting the second (PNA-like) PC of SLP, and that the QBO can be a useful predictor of SLP even in winters when the 50-hPa zonal wind over the equator is in the process of reversing between westerly and easterly regimes.

Using PCs and EOFs as axes for our phase space offers the advantage that the leading patterns are orthogonal to one another in both the time and space domains. Alternatively, the coordinate axes could be chosen to correspond with NAO and PNA patterns, as suggested by Ambaum et al. (2001). An objective way of defining this "NAO/PNA" phase space is to perform a varimax rotation of PC1 and PC2, which, by construction, yields the most spatially localized linear combinations of the EOFs. The non-orthogonal axes obtained through a varimax rotation in this two-dimensional phase space are located about halfway between the EOF1/EOF2 and the NAO/PNA sets of axes (not shown). Our choice of SLP as opposed to, say, 500-hPa height for defining the phase space is motivated by the fact that the eigenvalues are more clearly separated, yielding a sharper, more reproducible definition of the coordinate axes.[4] It is also notable that EOF 1 of SLP is virtually identical to the SLP pattern observed in association with the leading EOF of lower tropospheric temperature and the geopotential height at the lower stratospheric levels.

On the basis of rotated principal component analysis of the interannual variability of the 500-hPa height field Kushnir and Wallace (1989) concluded that only two modes stand out above the background continuum: the NAO and the PNA pattern. The consistency between the conclusions of our study and theirs, despite the differences in methodology, lends credence to the notion that true hemispheric "teleconnection patterns" are much more limited in number than the acronyms used to label them. Much of the redundancy is due to the reliance on subjectively defined indices as a basis for naming and characterizing patterns of variability. When the corresponding spatial patterns and projection indices are considered, the linear dependence of many of these so-called "modes" becomes readily apparent. On the other hand, we would not go so far as to claim that EOFs of order higher than the second are dynamically

[4]In the Monte Carlo test described at the end of section 3, for our sample size of 168 months, the rms error in the definition of the axes is 17° for the 500-hPa EOFs, compared to 7° for the SLP EOFs. This result is consistent with the algebraic derivation of the sampling error in eigenvectors given in the Appendix.

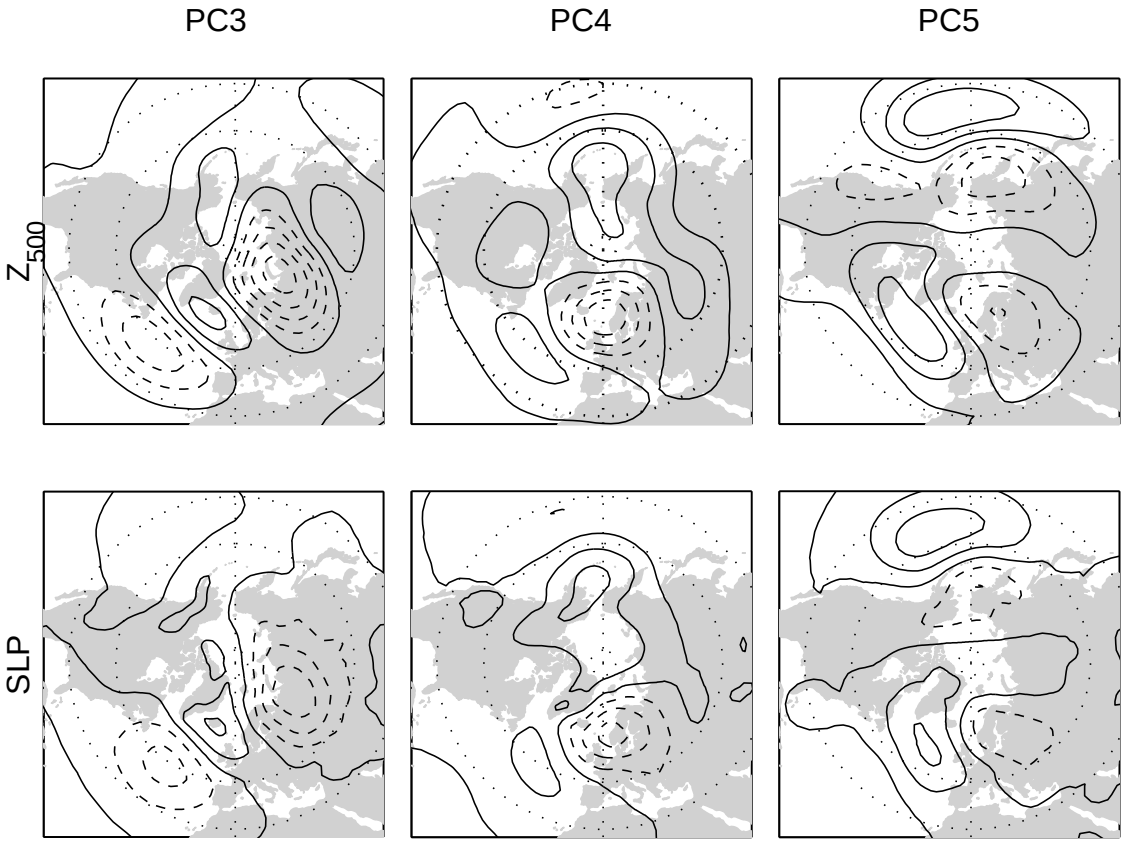

Figure 3.21: 500 hPa and SLP fields regressed upon time series of PCs 3-5 of the DJFM NH SLP anomalies poleward of 20°N. Contour interval 1.5 hPa for SLP and 15 m for 500 hPa height; negative contours are dashed.

unimportant. For example EOF3 of SLP (Fig. 3.21) is associated with an upper level wavetrain extending from the tropical Atlantic to Indonesia all the way across Eurasia along a great circle route. EOFs 4 and 5 capture variability over the Pacific sector related to the "North Pacific Oscillation" of Walker and Bliss (1932) and the "Western Pacific pattern" of WG. Collectively, these three patterns account for $\sim$ 25% of the month-to-month variance.

Chapter 4

THE TWO-DIMENSIONAL PHASE SPACE: FREQUENCY DEPENDENCE AND TRENDS

4.1 Introduction

After the description of the monthly variability, as represented in our two-dimensional phase space, we investigate in this chapter its frequency dependence.

Table 4.1 shows the ratio of the interannual to the intraseasonal variances of monthly mean DJFM data, and the one-month lag autocorrelation, for each of the first 10 monthly DJFM NH SLP PCs. By both measures, the two leading patterns are substantially redder (i.e. exhibit a larger fraction of temporal variance in the lower frequencies of the spectrum) than subsequent patterns and are therefore of particular interest from a climate perspective.[1]

To clarify the contributions from different frequencies to the variance explained by our phase space, in this chapter we will contrast the structure of the intraseasonal and interannual variability of NH SLP. We will also show that the spatial pattern of SLP trends over the Northern Hemisphere projects strongly upon the two dimensional phase space defined in the previous chapter.

This chapter is comprised of four sections. Section 4.2 discusses distinction between patterns of intraseasonal and interannual variability, in relation to the two-

[1]It is interesting to note that the next reddest mode (the 6^{th}, not shown) exhibits a vertical structure reminiscent of the NAM, but the node is located farther north and, as for the NAM, the associated zonally averaged zonal wind perturbations amplify with height into the stratosphere. Also, the one-month autocorrelation value of the leading PC, highest at the surface among tropospheric levels, is maximum at lower stratospheric levels.

Table 4.1: Ratio of the interannual to the intraseasonal variances (row 1) and one-month lag autocorrelation of monthly DJFM SLP PCs 1 to 10 (row 2).

	$PC1$	$PC2$	$PC3$	$PC4$	$PC5$	$PC6$	$PC7$	$PC8$	$PC9$	$PC10$
var ratio	1.01	0.77	0.33	0.46	0.37	0.63	0.39	0.45	0.40	0.39
autoc	0.45	0.31	0.07	0.21	0.10	0.22	0.09	0.15	0.06	0.06

dimensional phase space defined by the two leading PCs of the monthly data. Section 4.3 shows that trends in wintertime SLP and land surface air temperature over the last few decades project strongly onto the two-dimensional EOF phase space. A discussion of the results is given in section 4.4.

4.2 Frequency dependence

This section deals with four different aspects of the frequency dependence of the two leading EOFs of the SLP field:

- their combined contribution to the total hemispherically integrated variance
- the orientation of the two-dimensional phase space that they define
- their orientation within that phase space
- their relation to the global SLP field.

Table 4.2 shows the hemispherically integrated variance of the monthly, seasonal, and 5-year mean wintertime (DJFM) variability of the SLP field, and the fraction of that variance explained by the two leading PCs. In the second column the monthly mean SLP PCs are averaged, and in the third column new PCs are defined on the

Table 4.2: SLP variance north of 20°N of monthly, seasonal, and 5-year averaged data: ratio between area-weighted variance of averaged data and original monthly variance (first column); percentage of the variance explained by the combined leading two SLP PCs: averaged monthly PCs (second column), and PCs of averaged data (third column).

	v/v_m	$(PC1+PC2)_m$	$PC1+PC2$
monthly	1	36	36
seasonal	0.39	49	51
$5-yr\ mean$	0.15	72	74

basis of data averaged, as indicated, for each row. In both columns the fraction of explained variance increases with averaging interval. That the percentages in the two columns are similar implies that the two dimensional phase spaces defined by the monthly, seasonal, and 5-year mean EOFs must also be quite similar.

4.2.1 Patterns of temporal variance

Another way of documenting the increasing prominence of the NAM and the PNA-like pattern with increasing time scale of the fluctuations is through a comparison of the spatial patterns of temporal variance. The combined variance of EOFs 1 and 2 of monthly mean SLP is shown in Fig. 4.1, together with the total variance of the monthly, seasonal, and 5-yr running mean SLP field. The shape of the leading EOFs of monthly mean SLP is evident in all three total variance maps, and it is particularly prominent in those representative of the lower frequency variability. The corresponding residual fields, shown in the bottom row of Fig. 4.1, were formed by regressing out the pattern in Fig. 4.1a from the three total variance patterns. They lack the focused "center of action" that characterize the variance maps in which all EOFs are included.

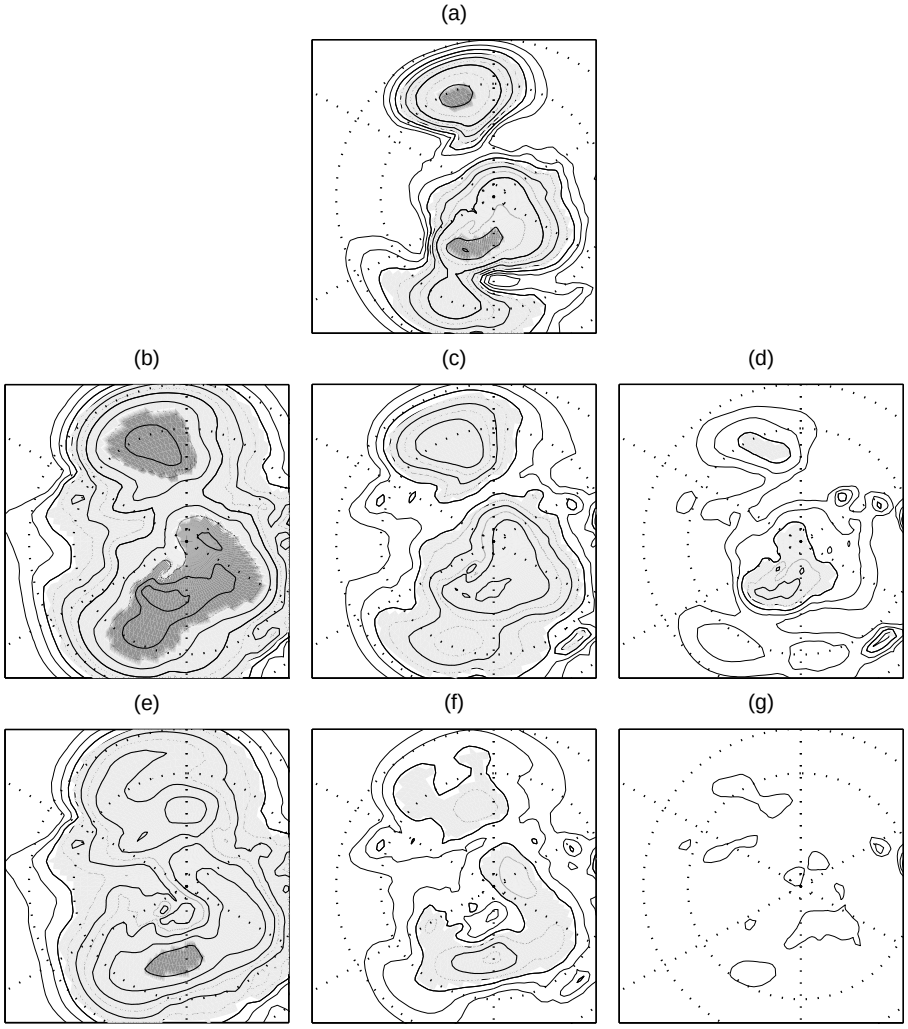

Figure 4.1: Variance maps of SLP data: (a) month-to-month variance explained by combined monthly PCs 1 and 2; total variance of observed (b) monthly, (c) seasonal mean, (d) 5-year mean data. (e,f,g): residual variances in (b,c,d) after removing the contribution of PCs 1 and 2. Contours: 6, 12, 20, 30, 42, 56, 72 hPa^2; the 6 and 42 hPa^2 contours are bold; additional light contours: 2 4 9 hPa^2.

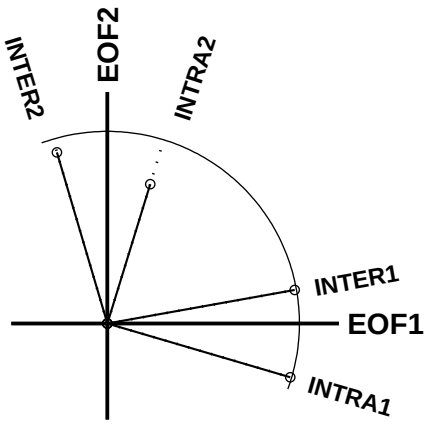

Figure 4.2: Projections (area-weighted spatial correlations) of patterns associated with EOFs of intraseasonal and interannual SLP fluctuations for the NH north of 20°N on the phase space defined by the two leading EOFs of monthly DJFM NH SLP anomalies, north of 20°N.

4.2.2 Intraseasonal vs. interannual phase spaces

To study how the spatial structures of variability depend on frequency, we compare here the EOFs of seasonal (DJFM) mean and intraseasonal (departures of monthly DJFM means from their respective winter season means) SLP fields, and we relate them to phase space defined by the monthly data. Fig. 4.2 shows the projections of the leading intraseasonal and interannual EOFs onto the plane of the monthly EOFs.

The interannual and intraseasonal EOF1s are seen in Fig. 4.2 to be linear combinations of the corresponding monthly EOFs, rotated counterclockwise by 16° and clockwise by 10°, respectively, relative to the leading EOF of monthly mean SLP. Hence, they differ from one another by 26°. In only 6% of a set of the Monte Carlo simulations, designed as described in Section 3.2.4, was the angular separation as large as the observed. Hence, the differences appear to be real.

The patterns of EOF1 for the interannual versus the intraseasonal Northern Hemisphere variability are compared in Fig. 4.3 a,d. The former is NAO-like, whereas the

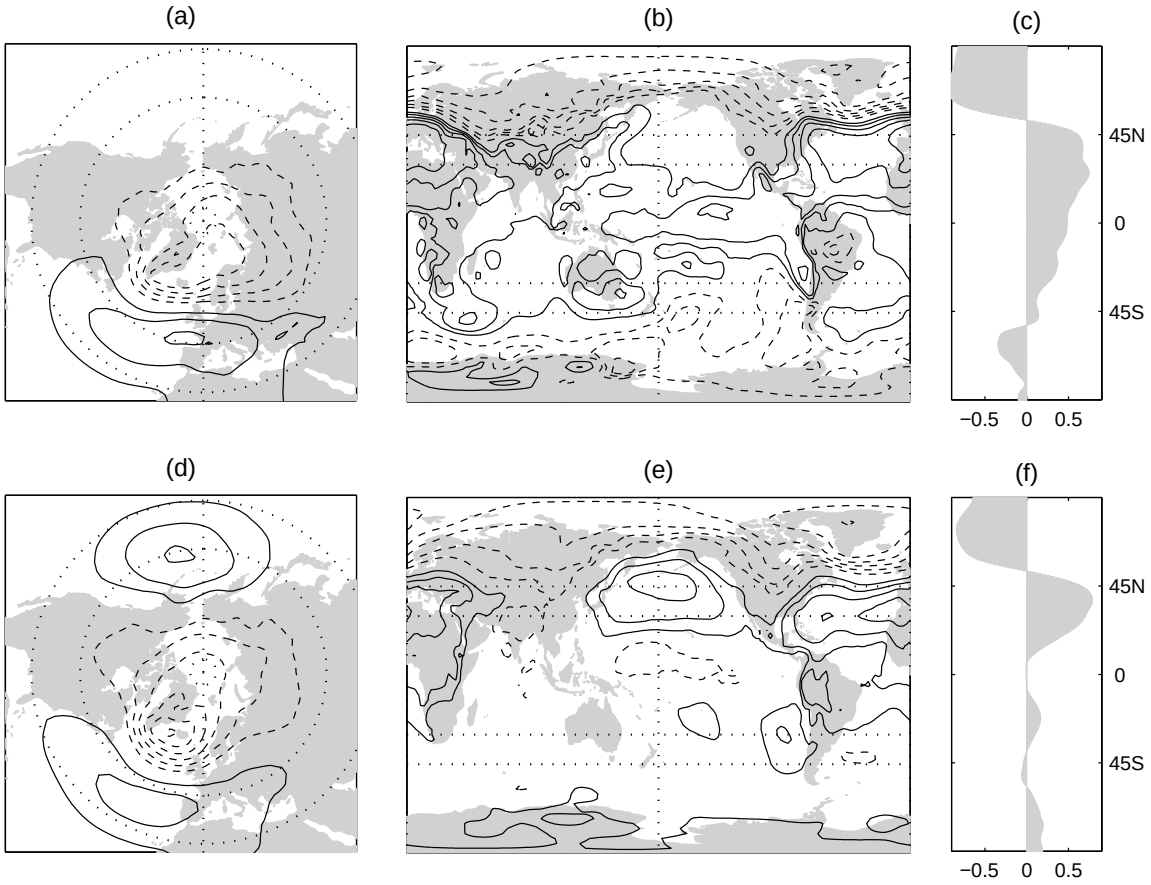

Figure 4.3: The leading EOF of (a) winter averaged and (d) intraseasonal NH SLP. a,d: hemispheric regression maps ; b,e: the corresponding global correlation maps for SLP; c,f: meridional profile of zonally averaged SLP correlation with PC1 of NH SLP. Contour intervals: 1 hPa (a,d), 0.15 (b,e). The zero contour is omitted.

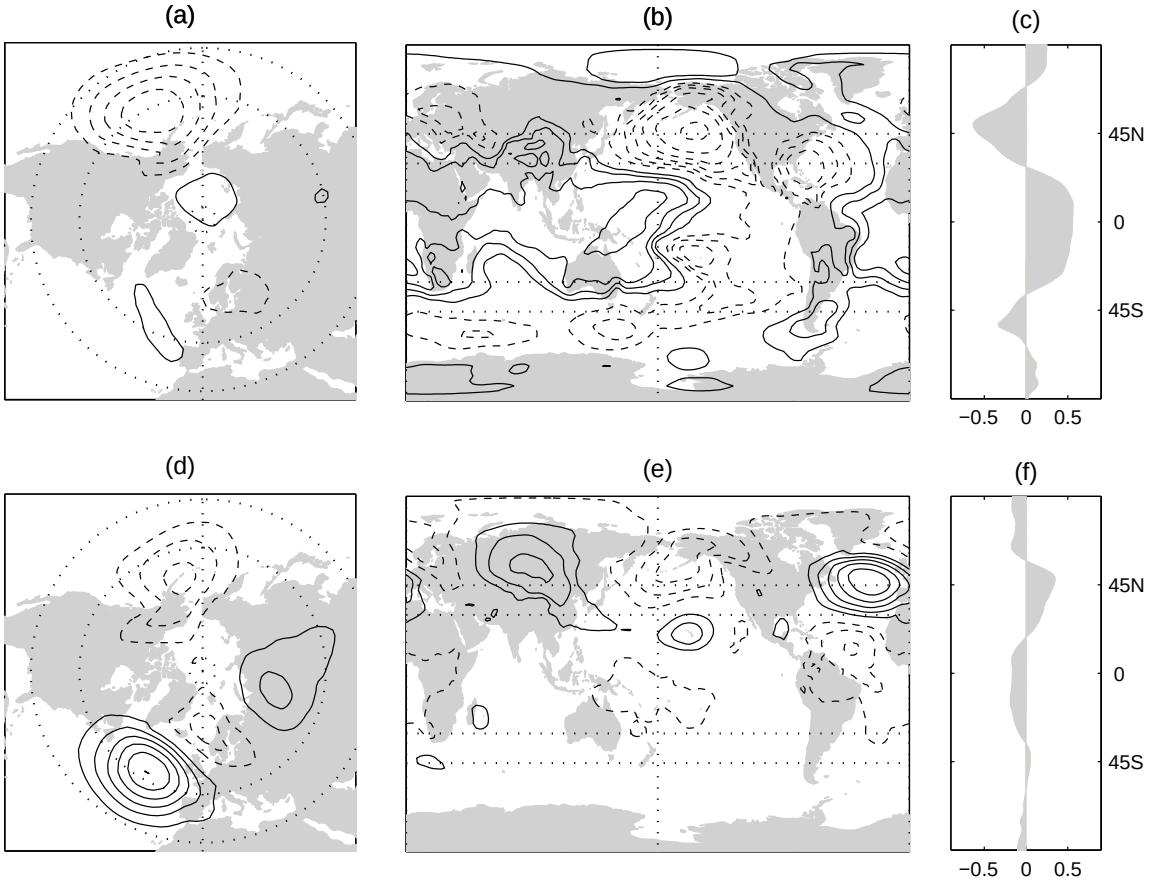

Figure 4.4: As in Fig. 4.3 but for the NH SLP PC2.

latter exhibits a strong Pacific center, as in the NAM. Pronounced differences are also evident in the correlation between PC1 and SLP over the remainder of the globe, as shown in Fig. 4.3 b, c, e and f. Correlations with the tropics and Southern Hemisphere are much stronger on interannual time scales, particularly in zonally averaged SLP.

Figure 4.4 shows corresponding patterns for EOF2. The pattern of the interannual variability is localized over the Pacific sector and it is clearly linked to the distinctive signature of the Southern Oscillation (Trenberth and Shea, 1987)), with a temporal correlation coefficient of -0.61 with the Southern Oscillation index. As is the case for

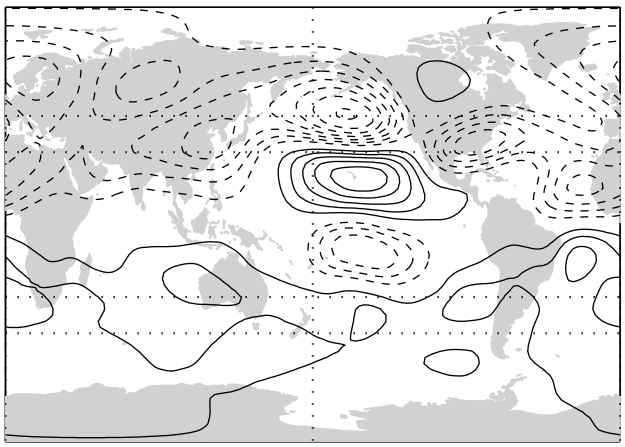

Figure 4.5: Global regression map of the 200 hPa streamfunction field upon the interannual NH SLP PC2.

EOF1, significant correlations extend into the tropics, suggestive of a global structure. The corresponding global regression pattern for 200-hPa streamfunction for interannual PC2 (Fig. 4.5) exhibits distinctive equatorially symmetric anticyclonic gyres over the Pacific sector, also reminiscent of the pattern associated with ENSO. In contrast, the intraseasonal pattern is suggestive of Rossby wavetrains trapped in extratropical northern latitudes. The extratropical atmospheric SLP signature of the pattern that Mantua et al. (1997) refer to as the Pacific Decadal Oscillation (PDO), formed by regressing SLP onto the leading PC of Pacific sea surface temperature poleward of 20°N (not shown), is also localized in the Pacific sector, consistent with the signature of the interannual EOF2.

The EOFs of detrended interannual data (Fig. 4.6) exhibit similar structural features to their counterparts of Figs. 4.3 and 4.4, but the amplitude of EOF1 in the tropics is significantly reduced.

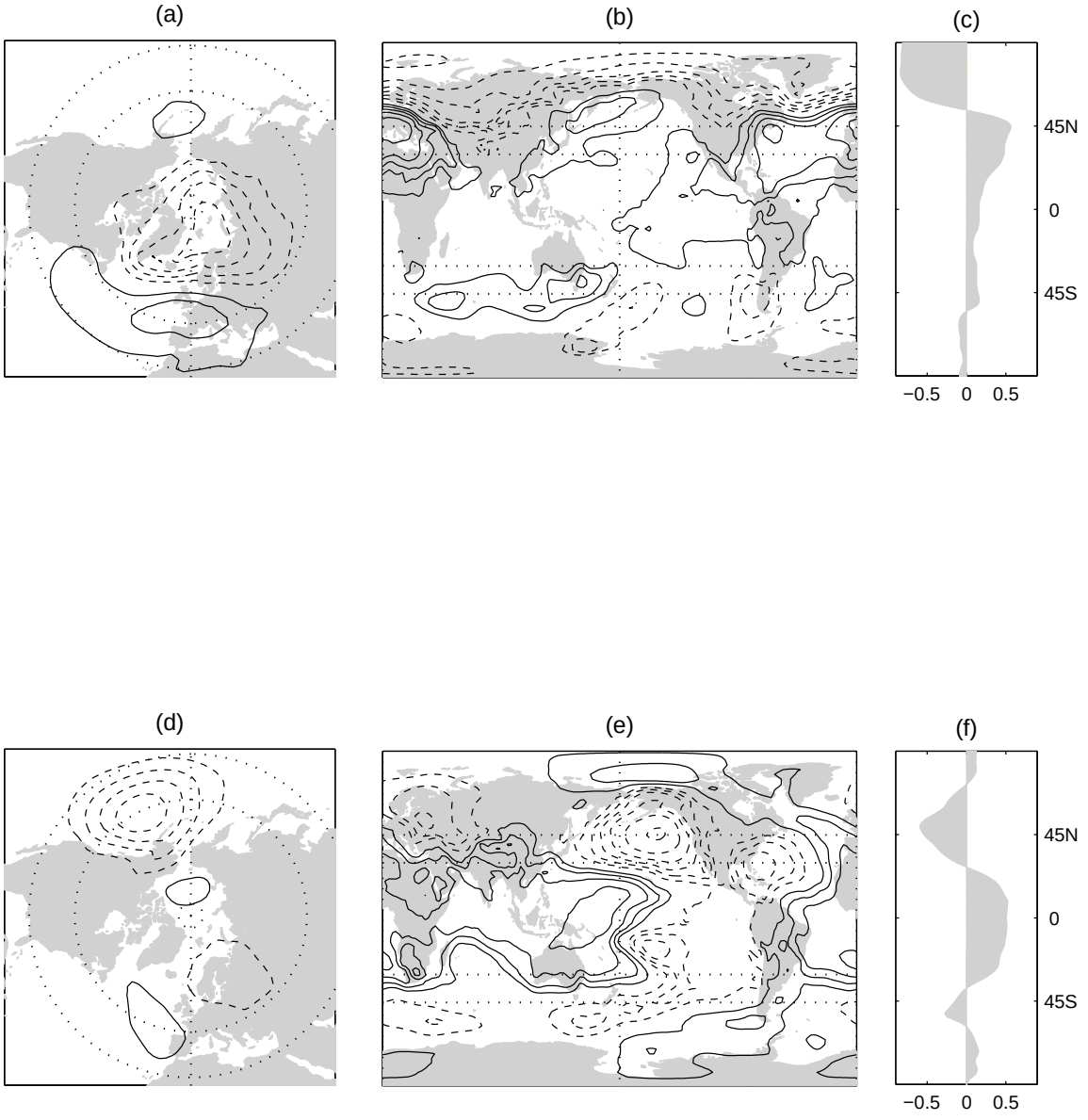

Figure 4.6: As in panels a-c of Figs. 4.3 and 4.4, but for EOFs of interannual detrended data.

4.3 SLP and SAT trends

SLP trends over different periods and regions have been documented in several recent studies. Trenberth and Hurrell (1994) noted a decrease of the Aleutian low pressure in the decade from 1976 to 1988; Walsh et al. (1996) reported a decrease in SLP over the Arctic from 1979 to 1994, and Gillett et al. (2003) documented the global 1948-1998 SLP trend. SAT trends have been documented in numerous studies, including Houghton et al. (2001).

This section documents the relation between the observed hemispheric SLP and SAT trends and the trends detected in the time series of the two SLP leading PCs. Averaged over the Northern Hemisphere, the mean squared amplitude of the observed SLP trend since 1958 (estimated by summing over all grid points, weighting by the cosine of latitude) is larger than any of the 1000 synthetic trends generated by randomly scrambling the chronological order of the winters. Based on a conventional t-test taking into account the lag-1 autocorrelation inherent in the time series, the trends in PC1 and PC2 of SLP are significant at the 99% and 95% levels, respectively. The linear combination of PC1 and PC2 that exhibits the largest trend is significant at the 99.9% level.

In projecting the SLP trend pattern upon the two-dimensional phase space, the SLP data were linearly detrended before computing the EOFs in order to ensure that the phase space is not in any way influenced by the existence of the linear trend.[2] The result is shown in Fig. 4.7. In agreement with previous studies of Hurrell (1995) and Thompson et al. (2000) the pattern of SLP trends projects strongly upon the NAO and upon PC1, the index of the NAM. The angle in this two-dimensional phase space coincides almost perfectly with that of the NAO.

The spatial patterns of the observed trends in SLP and SAT, their projection

[2]The EOFs of detrended data are rotated clockwise by an angle of about 10° in the phase space of Fig. 3.5.

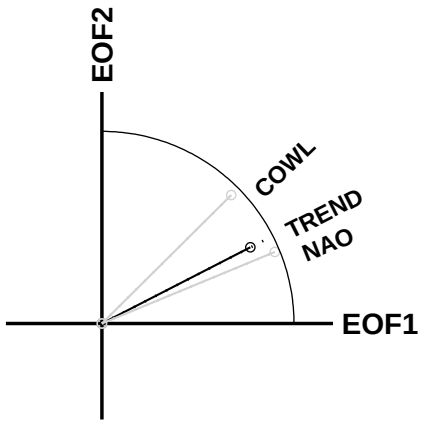

Figure 4.7: As in Fig. 3.5a, but for the spatial pattern of the observed SLP trend projected on the EOFs of the detrended monthly SLP field. For reference, projections of the NAO and COWL patterns are also shown in gray.

upon the least squares best fit linear combination of the two leading PCs of the SLP detrended dataset, and the residual trend are shown in Fig. 4.8. The resemblance between the spatial pattern of the SLP trend and its projection upon the PCs is quite striking. The residual trend does not exhibit a coherent, planetary-scale structure, and its hemispherically averaged mean squared amplitude is typical of those in trend patterns derived from the temporally scrambled data.

The lower panels of Fig. 4.8 show corresponding results for SAT. The large fraction of the regional SAT trends that can be accounted for on the basis of the trends in the SLP PCs is indicative of the strong dynamical controls on regional wintertime SAT trends. The pattern of residual trend is patchy, with warming in some areas and cooling in others.

4.4 Discussion

We have shown that the structure of leading EOFs of the interannual and intraseasonal variability of SLP are different in two respects:

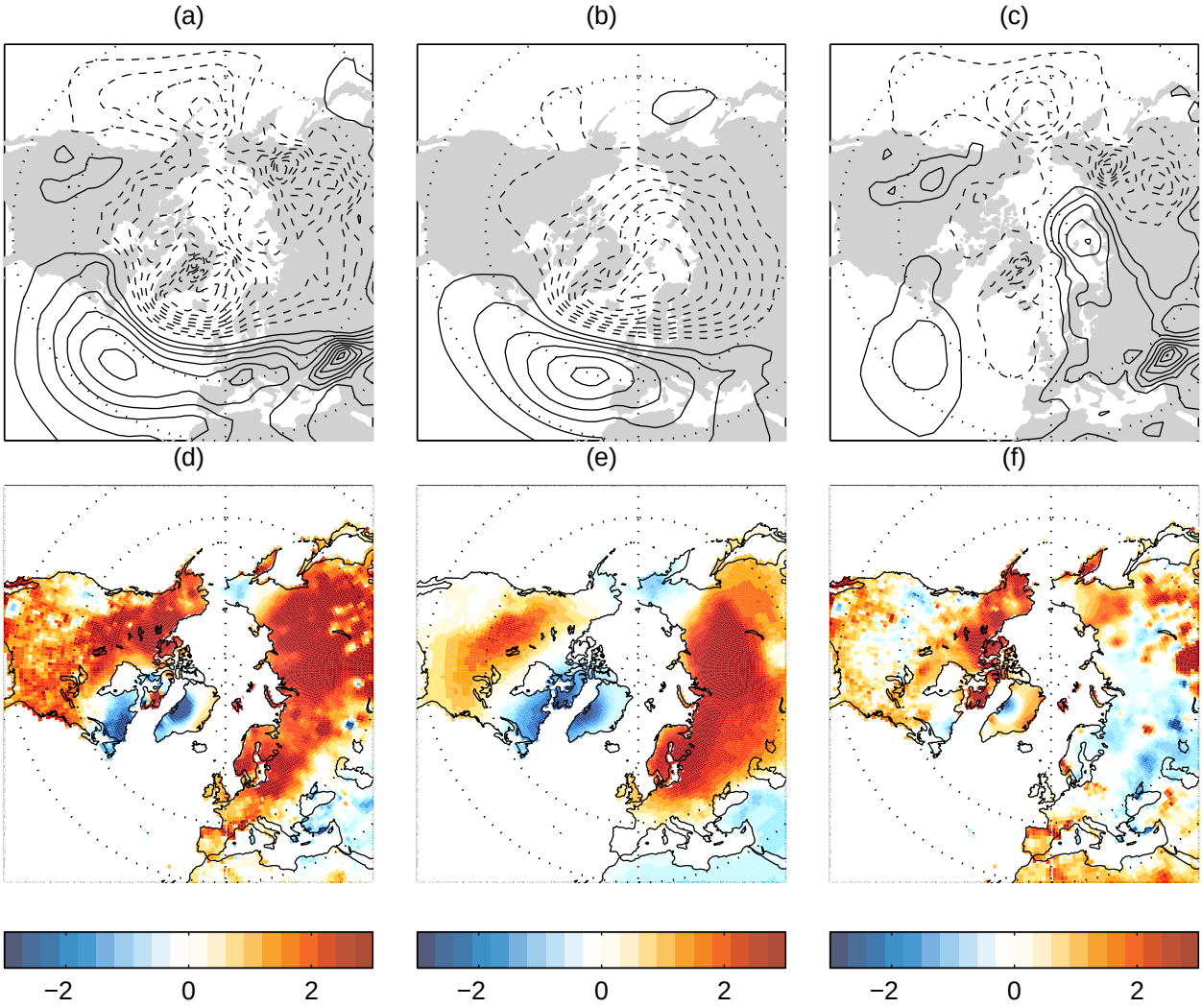

Figure 4.8: (a-c) SLP and (d-f) wintertime (DJFM) 1958-99 SAT trends (per 42 years). (a) and (d) Linear trend. (b) and (e) The component of that trend that is linearly congruent with the two leading PCs of the detrended SLP field. (c) and (f) The residual trend. SLP contour interval 1 hPa; the zero contour is omitted.

1. the interannual EOFs tend to be localized over Atlantic Arctic and Pacific sectors, whereas the first intraseasonal EOF has a more annular hemispheric structure, and the second is suggestive of a coupling between the PNA wavetrain and another wavetrain emanating from the Atlantic sector and extending across Eurasia;

2. the intraseasonal EOFs are largely trapped within the NH extratropics, whereas the interannual EOFs appear to be hemispheric expressions of global patterns.

That the interannual patterns tend to be more global than the intraseasonal ones suggests that they are partially shaped by tropical forcings or feedbacks. The obvious candidate in the case of EOF2 is ENSO dynamics involving equatorial Pacific sea surface temperature anomalies. The tropical connection in the case of EOF1 is less clear. Consistent with results of Koide and Kodera (1999), we find that its tropical SST signature, as revealed by linear regression analysis (not shown), is much weaker and less distinctive than that of EOF2. It is also conceivable that the hemispheres could be linked on the interannual time scale by way of the lower stratosphere. Placing the hemispheric results in a global context is a challenge for future research.

The overall results of this and the previous chapter emphasize the strong contribution of the two leading PCs of the NH SLP field to the wintertime low frequency variability. Together, these patterns account for over one third of the variance of the monthly mean SLP field, around half of the variance of the wintertime mean SLP field, over 2/3 of the variance of 5-winter mean SLP field, and virtually all the coherent, planetary-scale structure in the 1958-99 winter SLP trend pattern. Analogous statistics based on Trenberth and Paolino's (1980) data for the period of record 1925 to 1999 are shown in Table 4.3.

The increasing prominence of these patterns as one progresses from intraseasonal to interannual to interdecadal time scales suggests that they play an important role in the wintertime SLP and SAT variability on time scales of centuries and longer.

Table 4.3: As in Table 4.2, but for 1925-1999 SLP data.

	v/v_m	$(PC1+PC2)_m$	$PC1+PC2$
monthly	1	34	34
seasonal	0.38	43	44
$5-yr\ mean$	0.12	52	52

This suggests that the two leading EOFs might be even more prominent in ensemble simulations of 20^{th} century climate variability such as those performed for the Model Intercomparison Projects (AMIP, CMIP). Furthermore, one might expect trends in these modes be important in experiments simulating anthropogenic climate change.

Chapter 5

THE TWO-DIMENSIONAL PHASE SPACE: INFLUENCE ON WEATHER

5.1 Introduction

The low frequency variability of the atmospheric circulation has a direct impact on weather. In section 3.10 we showed how the component of the low frequency variability described by our two dimensional phase space affects monthly mean wind, temperature and precipitation fields. A more indirect influence occurs through impacts on the amplitude and structure of the higher frequency variability embedded in the lower frequency variability. This indirect influence has a significant effect upon the frequency of episodic events such as floods and heavy snowfall, and extreme temperatures.

To study the indirect influence of our two dimensional phase space on weather, we document in this chapter the varied expressions of the hemispheric circulation observed in association with contrasting polarities of the two basis functions. The two patterns associated with the monthly PCs are projected upon 5- and 10-day mean data (as described in section 2.2), and ensembles characterized by extreme values of the PCs are compared, with respect to the shapes and variability of contours, the structure of blocking and teleconnections, and the occurrence of extreme cold events.

This chapter is organized in six sections. After introducing the four ensembles studied in section 5.2, section 5.3 contrasts the variability of specified contours of 10-day mean 500-hPa height, sea-level pressure, and 1000-500 hPa thickness fields observed in association with the "high index" and "low index" polarities of the SLP

EOFs 1 and 2. Sections 5.4 and 5.5 show examples of contrasting patterns, teleconnections and blocking, respectively, observed within the contrasting subclimatologies, defined in accordance with the polarities of the principal patterns of variability. After a discussion of the implications for regional climate impacts in section 5.6, section 5.7 offers a discussion of the results.

5.2 The 10-day mean ensembles

We introduce here four ensembles characterized by extreme high and low values of PC1 and PC2, as defined in chapter 2. Figure 5.1 shows 500 hPa mean maps for the "high index" and "low index" subclimatologies of PC1. The mean map of the high index subset of PC1 (H1) shows a well defined polar vortex centered over Greenland/northeastern Canada, with strong zonal flow at subpolar latitudes. The contrasting low index subclimatology (L1) is characterized by a weaker polar vortex with three fewer contours at the low end of the range. A pronounced blocking anticyclone is evident centered over the southern tip of Greenland. Consistent with results of DeWeaver and Nigam (2000) this feature exhibits a northwest-southeast tilt, in contrast to the flat ridge over western Europe in the H1 subclimatology, which exhibits a northeast-southwest tilt.

Figure 5.2 shows the corresponding maps for high index and low index subclimatologies based on EOF2 (H2 and L2). While the distinctions between the high and low index polarities of EOF1 mainly relate to the different intensities of the polar vortex, those in EOF2, shown in Fig. 5.2, relate to the planetary-wave configuration. In the high index subclimatology (H2), the polar vortex exhibits a secondary center over the North Pacific, the Asian jet extends nearly all the way across the Pacific and ridges lie along the west coasts of both continents. L2 is characterized by troughs over the east coasts of the continents and weak ridges over the central Pacific and Scandinavia. The most prominent feature in the standard deviation maps is the higher

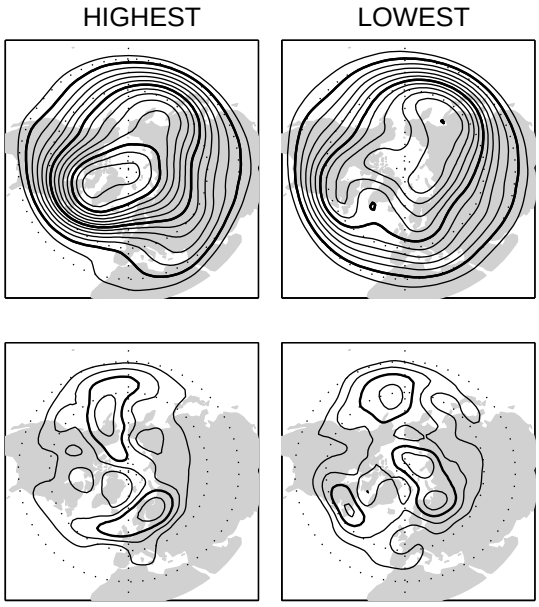

Figure 5.1: Composite mean (upper panels) and standard deviation (lower panels) of 500 hPa height for the 30 10-day mean maps with the most positive and the 30 10-day mean maps with the most negative values of PC1 of SLP, as indicated, subject to the limit of 2 dectads per winter. Contour interval in upper panels: 60 m; the 5100, 5400 and 5700 m contours are bold. Contour interval in lower panels: 20 m; the 110 m contour is bold.

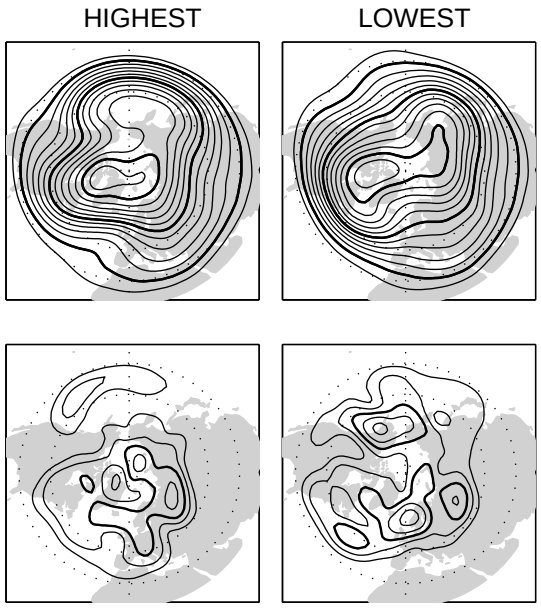

Figure 5.2: As in Fig. 5.1 but for PC2.

variability over Alaska in L2, consistent with Palmer's (1988) composites based on the PNA pattern.

5.3 Variability of selected contours

This section presents a qualitative analysis of the changes of variability among the four ensembles, through the use of "spaghetti diagrams", described in section 2.2.1.

5.3.1 Flow patterns associated with EOF 1

Figure 5.3 compares a series of specified 500-hPa height contours extracted from 10-day (dectadal) mean maps for the H1 and L1 subclimatologies. In H1 the core of the polar vortex at the 500-hPa level is almost always centered on the Canadian side of the Arctic, whereas in L1 it is usually centered on the Siberian side. Contours higher than 510 dam rarely intrude into the core region of the vortex in H1, while

heights in excess of 528 dam are frequently observed throughout the Arctic in L1. The signature of Greenland blocking is clearly evident in most of the L1 dectads and many of these events are characterized by pronounced upstream troughs over southeastern Canada and/or downstream troughs over Eastern Europe. In H1 the 528 and 540 contours assume the form of tight bundles from the Rockies eastward through Europe, whereas in L1 they exhibit much more diversity from sample to sample and some of them intrude into substantially lower latitudes. Contrasts between H1 and L1 subclimatologies are not as pronounced over the east Asian and Pacific sectors. The 540 dam contours crossing over Japan form tight bundles in both subclimatologies, but the L1 bundle is noticeably farther south. Dectads with high amplitude ridges over Alaska are observed in both H1 and L1.

The patterns for the outer contours in the polar vortex exhibit a somewhat different behavior. In H1 the 558 dam contour often shows indications of a trough over the Middle East with a broad upstream ridge over Europe, whereas this configuration is rarely observed in L1. In association with that same ridge, the 570 dam contour frequently intrudes into Europe in H1, but rarely in L1. On the other hand, owing to the larger variability over the Mediterranean region in H1, the southernmost 570 dam contours extend at least as deep into North Africa and the Middle East in H1 as they do in L1.

Figure 5.4 shows analogous plots of the 1028 and 992 hPa sea-level pressure (SLP) contours. The former surrounds strong anticyclones at the earth's surface in the 10-day mean fields and the latter surrounds strong cyclones. The H1 subclimatology is characterized by a higher frequency of occurrence of >1028 hPa anticyclones over the subtropical eastern oceans and an almost complete absence of them over higher latitudes. Many of the North Atlantic anticyclones in H1 extend eastward into Europe and the Middle East. SLP often drops below 992 hPa in the Davis Strait, over the far North Atlantic and the European sector of the Arctic and much less often in the vicinity of the Aleutian Low. L1 is characterized by a high frequency of occurrence

of >1028 hPa anticyclones that encompass parts of the Arctic and a relative absence of them at lower latitudes. The Siberian High is evident in both H1 and L1, but it extends farther westward toward Europe in L1. Inspection of analogous results for the 1036 hPa contour (not shown) indicates that the Siberian High also tends to be somewhat stronger during L1, in agreement with results of Gong and Zhu (2001). SLP drops below 992 hPa in the vicinity of the Aleutian Low and over temperate latitudes of the North Atlantic more frequently during L1 than during H1.

Figure 5.5 shows spaghetti diagrams for four 1000-500-hPa thickness contours. Thicknesses below 492 dam are observed most frequently over northeastern Canada and Greenland during H1 and over eastern Siberia and Mongolia in L1. The 510 contour exhibits somewhat greater variability over the American and Atlantic sectors in L1 than in H1, but contrast between the overall level of variability in L1 and H1 is less dramatic than in the case of the 500-hPa height contours shown in Fig. 5.3. In agreement with the conjecture of Namias (1951), the area occupied by Arctic air masses, as defined by the outer edge of the envelopes of the 510 and 522 dam contours, is larger during L1 than during H1. The 540 dam contour intrudes noticeably deeper into the Middle East in H1, consistent with the lower surface air temperatures observed over this region during H1 (Thompson and Wallace, 2001).

5.3.2 Flow patterns associated with EOF 2

Figure 5.6 is the analog of Fig. 5.3, but for PC2. The shapes of the 500-hPa height contours for H2 show a tendency for a pronounced ridge aligned with the Rockies that separates the Arctic and Pacific lobes of the polar vortex, and a flatter ridge over the Atlantic, as best exemplified by the 522 and 540 dam contours. The trough immediately downstream of the Atlantic ridge sometimes resides over central Europe and at other times resides farther to the east over Russia. The charts for L2 exhibit a greater diversity of the 540 dam contour shapes, especially over the Pacific and western Europe where pronounced short wavelength ridges are often observed,

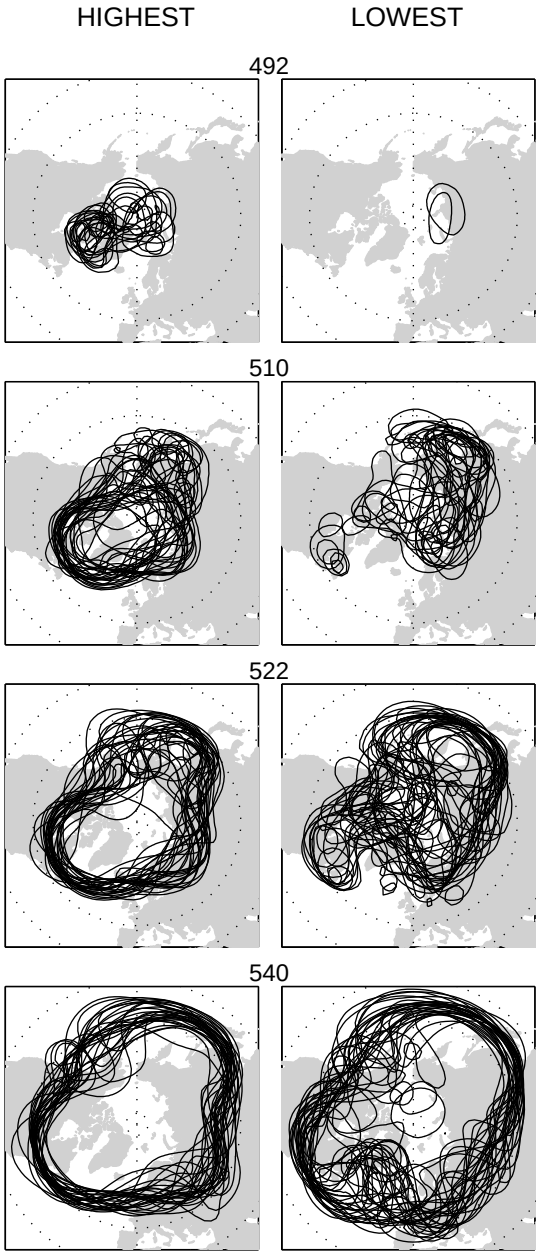

Figure 5.3: "Spaghetti plots" for specified 500 hPa contours for the contrasting polarities of PC1: the 30 dectads with the highest value of SLP PC1 versus the 30 dectads with the lowest values of SLP PC1, which represent roughly the top and bottom 6% of the frequency distribution of PC1.

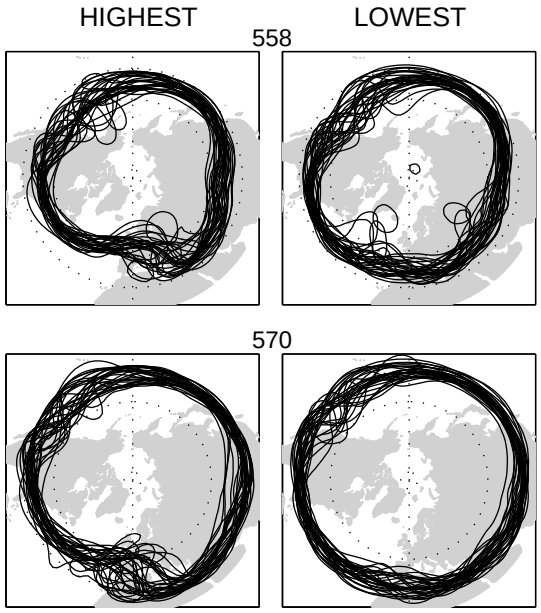

Figure 5.3: continued.

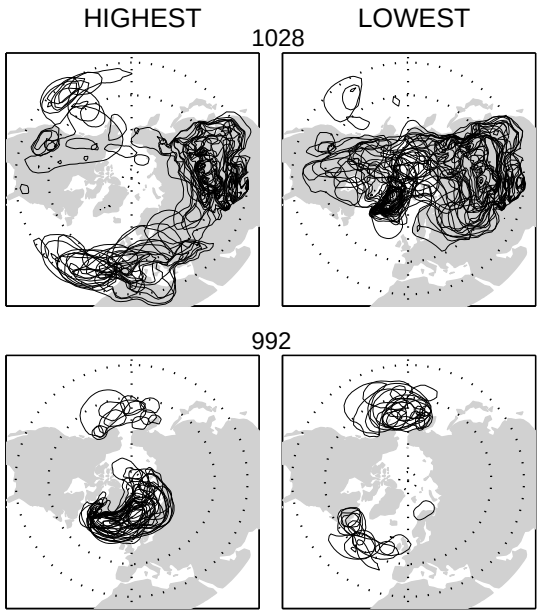

Figure 5.4: As in Fig. 5.3, but for selected SLP contours, as indicated.

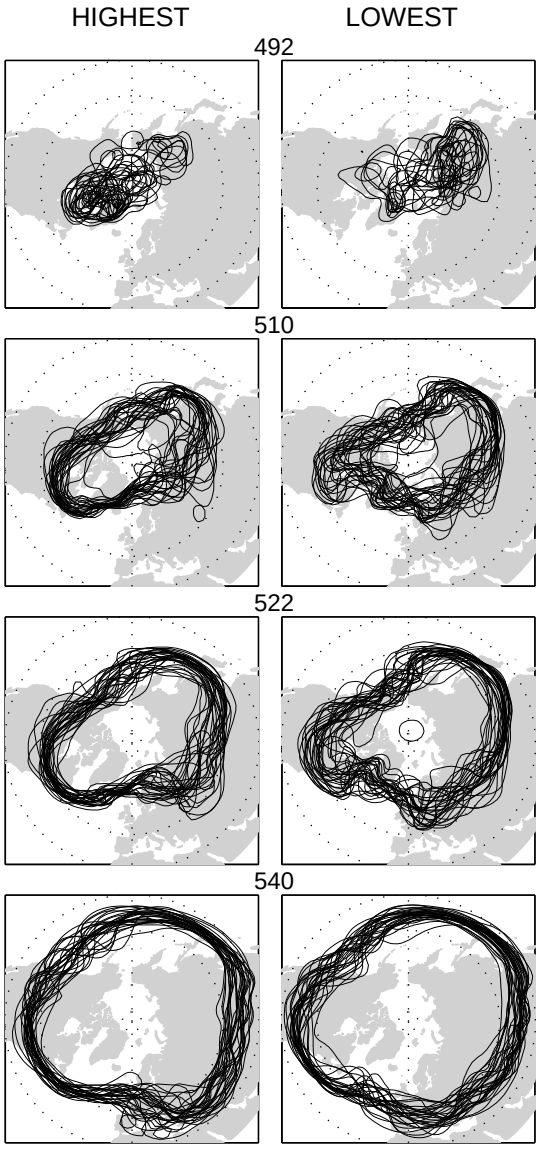

Figure 5.5: As in Fig. 5.3, but for 500 hPa-1000 hPa selected thickness contours, as indicated.

coincident with the variance maxima in Fig. 5, sometimes accompanied by sharp downstream troughs. Hence, the weak westerly flows over these regions in the mean L2 map (Fig. 5.2) represent averages of flow patterns with pronounced, but varied, meridional structure.

5.4 Contrasting teleconnection patterns

To further illustrate how low frequency variations in the atmosphere's primary patterns of variability influence the structure of the embedded variability we constructed a series of regression maps of 500 hPa height upon PC1 and PC2, each based on subclimatologies of the data defined in accordance with the rankings of the other PC. Figure 5.7 shows contrasting regression maps for PC1 as obtained from high-index and low index subclimatologies of PC2, denoted by H2 and L2, respectively, and Fig. 5.8 shows regression maps for PC2 obtained from the H1 and L1 subclimatologies. The PCs used in this analysis are defined on the basis of the entire dataset.

The PC1 regressions based on H2 and L2 exhibit substantial differences with respect to the flow configuration over the Pacific sector: the pattern for H2 exhibits a north-south dipole reminiscent of the pattern in the Atlantic, while the pattern for L2 exhibits a pronounced wavetrain oriented along a "great circle route". Both PC2 patterns are PNA-like over the Pacific sector, but they are quite different in the remainder of the hemisphere. In H1 the Pacific / North American (PNA) wavetrain bends southeastward into the subtropical Atlantic and seems to rebound, forming a second wavetrain with strong centers of action over the North Atlantic and European Russia. In contrast, the PNA wavetrain in L1 is directed eastward across southern Canada toward western Europe. The tendency toward more equatorward turning over North America in H1 is consistent with the contrasting "steering flow" configurations in the upper panels of Fig. 5.1. The difference in zonal wavelength is consistent with the Rossby dispersion relation for zonal flow with variable intensity. The patterns in

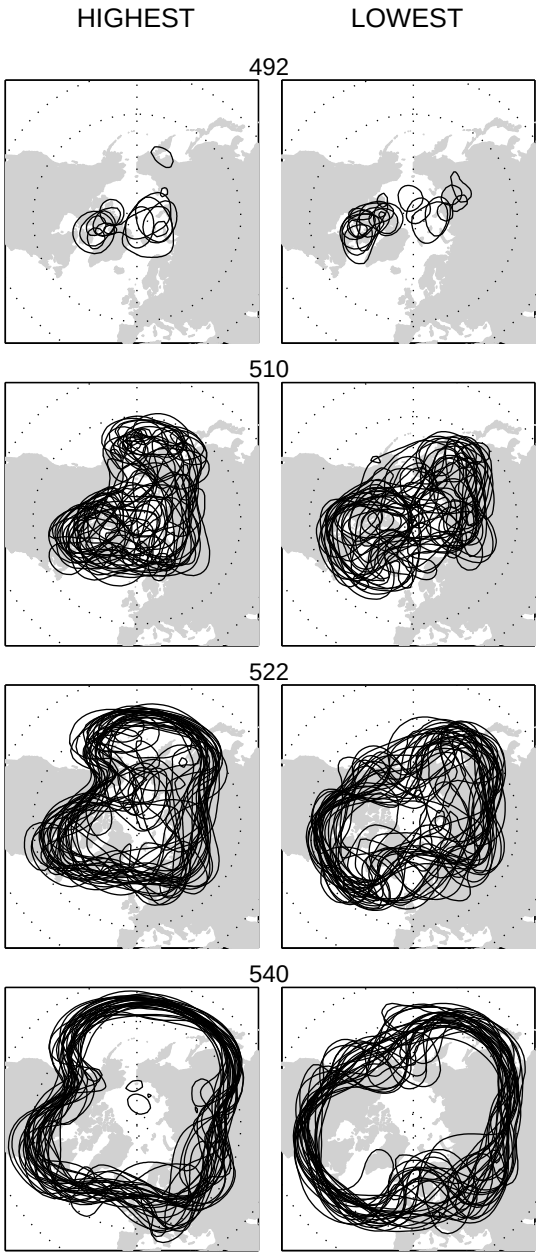

Figure 5.6: As in Fig. 5.3, but for PC2.

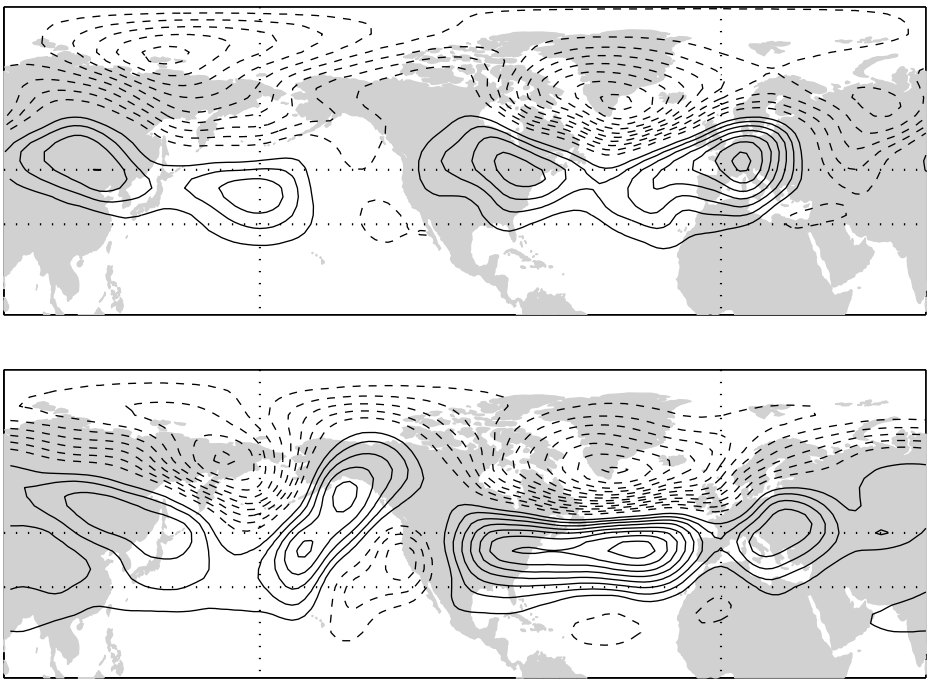

Figure 5.7: 500-hPa height anomalies regressed upon standardized time series of SLP PC 1 based on the subclimatologies of the data consisting of the 30 dectads with the highest (upper) and lowest (lower) values of SLP PC2. Contour interval 15 m; negative contours are dashed. The zero contour is omitted.

Figs. 5.7 and 5.8 are reproducible in subclimatologies based on the 60 (instead of 30) extreme values of PC1 and PC2 (not shown).

5.4.1 Relation between downstream features of PNA pattern and tropical heating

Figure 5.8 shows a well defined second wavetrain for the PNA observed in association with high index NAM conditions. Here we briefly discuss the possible dependence of the downstream propagation of the PNA pattern on the occurrence of anomalous heating over the tropical Atlantic. One reason for the presence of the second wavetrain associated with the PNA pattern may be the presence of deep convection over the tropical Atlantic region, where the first wave train ends. Consistent with this

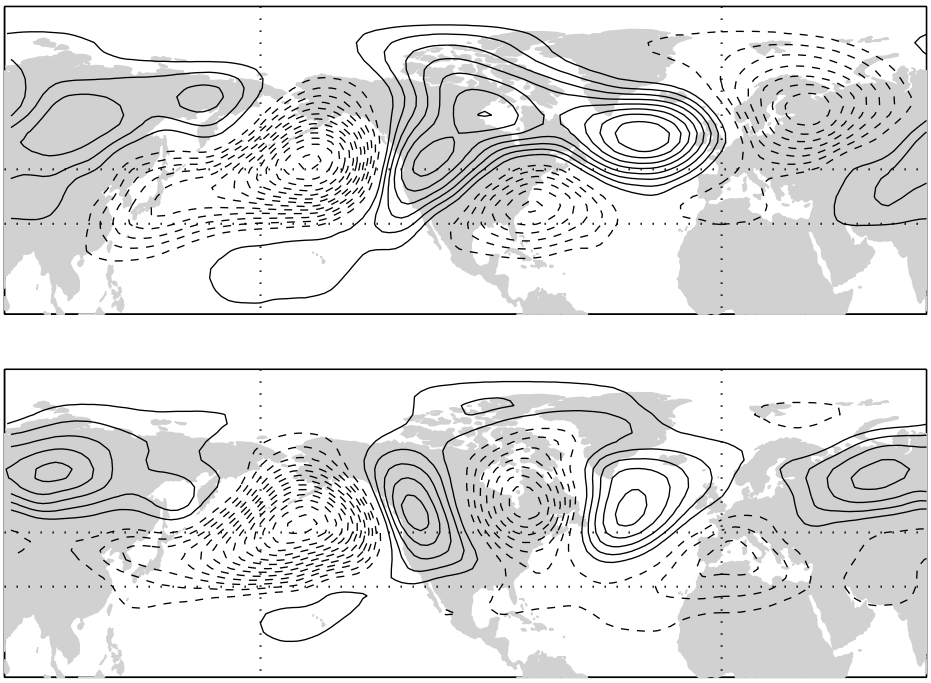

Figure 5.8: 500-hPa height anomalies regressed upon standardized time series of SLP PC 2 based on the subclimatologies of the data consisting of the 30 dectads with the highest (upper) and lowest (lower) values of SLP PC1. Contour interval 15 m; negative contours are dashed. The zero contour is omitted.

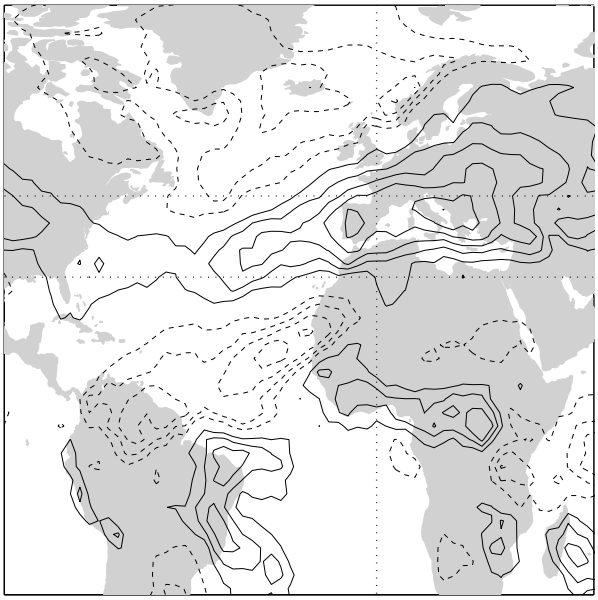

Figure 5.9: Monthly OLR anomalies regressed upon standardized time series of SLP PC1, DJFM 1979-99. Contour interval: $1.2 W m^{-2}$.

hypothesis, Winkler et al. (2001) show that the persistence of the PNA pattern, and especially of the downstream center over the Atlantic region, is strongly dependent upon the strength of the tropical diabatic heating term of their linear inverse model. For high index NAM conditions, the tropical Atlantic region exhibits anomalously high convection (or low OLR anomalies, as in Fig. 5.9). Results consistent with this hypothesis are obtained when stratifying the data according to the values of OLR anomalies over a box chosen to represent the tropical Atlantic region[1]. Figure 5.10 shows that the second wavetrain appears in association with the PNA time series[2] only in the subset characterized by low OLR anomalies over the tropical Atlantic box, while under the opposite conditions the more sectoral PNA pattern is observed.

---

[1]The region is defined as 5-25°N, 280-350°E.

[2]Note that here, in contrast with the methodology used in Fig. 5.8, the time series of the pure PNA pattern (not SLP PC2) is used for the regression maps, in order not to impose by construction the presence of the second wave train.

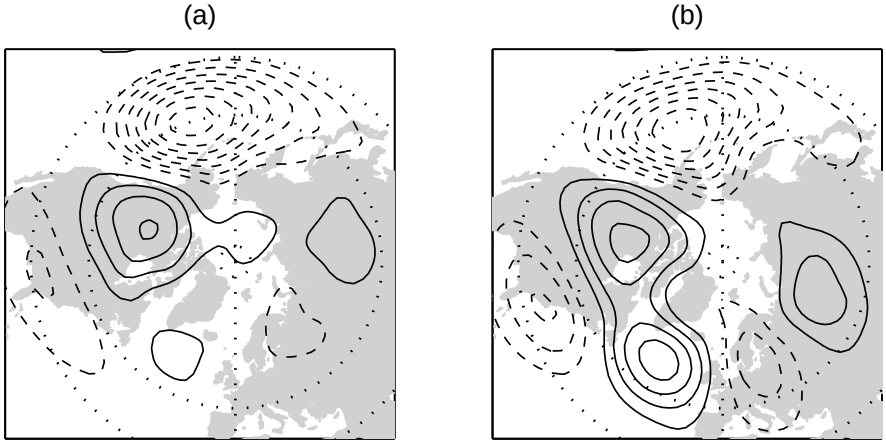

Figure 5.10: Monthly 500 hPa anomalies regressed upon standardized time series of PNA, for (a) positive (39 months), and (b) negative (40 months) values of averaged tropical Atlantic OLR, DJFM 1979-99. Contour interval: 12 m.

5.5 Contrasting structures of blocking

In order to explore how the morphology of blocking is influenced by PC1 and PC2 we constructed a series of composite charts for dectads that simultaneously satisfy two criteria: (1) their patterns of 500-hPa height anomalies project strongly upon PC1 or PC2 and (2) they exhibit the highest ranking 500-hPa height anomalies at some specified grid point. In this part of the investigation the requirement of selecting no more than 2 events per winter is relaxed.

Figure 5.11 shows results for the gridpoint (65° N, 150°W), chosen to be representative of Alaska blocking. This gridpoint lies close to the zero line of SLP and 500-hPa regression maps for both PC1 and PC2 (see Fig. 2.1), limiting the problem due to having different phases of planetary waves during opposing polarities of the PCs. Blocking anticyclones are evident over the reference gridpoint in all four panels of the figure, but the flow configurations are somewhat different in each panel. In the contrasting H1 and L1 subclimatologies, the flow configurations are similar over the Pacific sector, but quite different elsewhere in the hemisphere. L1 exhibits si-

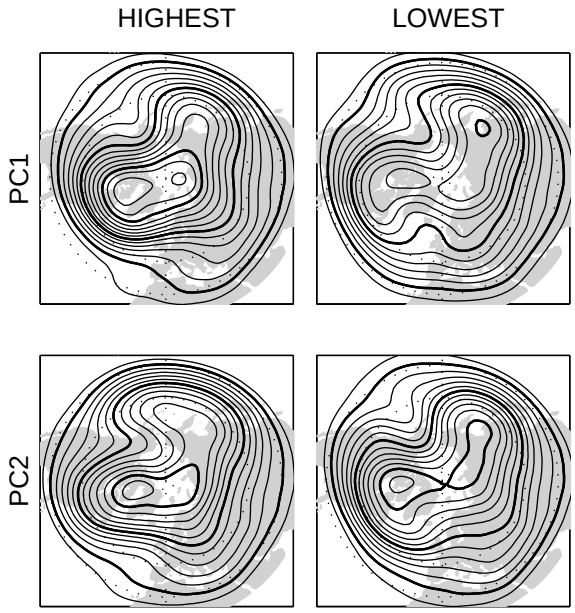

Figure 5.11: Composite mean 500 hPa height charts for the 20 dectads with the most positive anomalies at the grid point (150° W, 65° N) based on the subclimatologies of the data consisting of the 80 dectads with the strongest positive and negative values of PC1 (upper panels) and PC2 (lower panels). Contour interval: 60 m; the 5100, 5400 and 5700 m contours are bold.

multaneous blocking ridges over the Pacific and Atlantic sectors, whereas in H1 only the Alaska ridge is evident. The most striking contrast between H2 and L2 is the different flow configuration in the vicinity of the block itself. In H2 the blocking ridge is aligned with the Rockies, whereas in L2 it lies along 150 W at all latitudes. Similar distinctions are evident in Figs. 3.14 and 3.16 of Wallace and Blackmon (1983) in the cluster analyses of Kimoto and Ghil (1993b: Pacific regimes 2 and 7, Fig. 7), Cheng and Wallace (1993: cluster R vs. cluster A, Fig. 8), and in regimes 2 and 4 of Robertson and Ghil (1999, Fig. 6).

The impacts of the two types of ridges on weather conditions over western North America are dramatically different, with mild conditions in H2 and major cold outbreaks frequently occurring in L2.

Figure 5.11 shows another example, this one for the gridpoint (62.5° N, 22.5°W) over the eastern North Atlantic, contrasted with respect to the first mode only. The composite for L1 exhibits a symmetric "omega" block centered west of Great Britain which is often accompanied by cold air outbreaks over the eastern United States and western Europe (Rex, 1951). In contrast, H1 is characterized by a northeast-southwest tilted ridge which is typically associated with mild weather over Europe, but below normal temperatures over the Mediterranean and North Africa.

5.6 Regional climate impacts

Taking into account the background state of the flow has implications when evaluating the regional scale impacts of teleconnections. Figure 5.13 illustrates the slightly different signatures of PC2 in the 850-hPa temperature field over the US during events characterized by extreme positive and extreme negative polarity of PC1. Analogous diagrams for monthly SAT data (not shown) show consistent results. Fig. 5.14 is the analog of Fig. 5.13 but for precipitation over Europe. The pattern associated with PC2 during positive anomalies of PC1 is quite robust with respect to changes of the

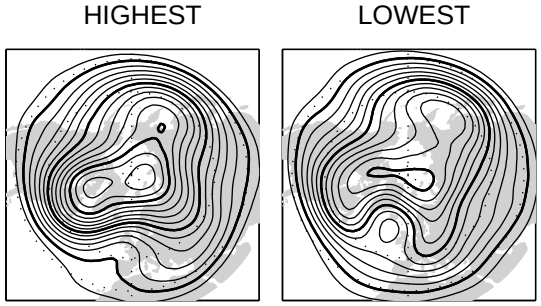

Figure 5.12: Composite mean 500 hPa height charts for the 20 dectads with the most positive anomalies at the grid point (22.5° W , 62.5° N) based on the subclimatologies of the data consisting of the 80 dectads with the strongest positive and negative values of PC1. Contour interval: 60 m; the 5100, 5400 and 5700 m contours are bold.

subset size (from 9 to 30 to 50 months, not shown). However, the signature of PC2 for negative anomalies of PC1 is more sensitive to the size of the subset, consistent with the higher variability observed over Europe during the low polarity of PC1. It is possible that the strong vortex conditions represented by high values of PC1 more strongly constrain the Pacific wave propagation, while weak vortex conditions allow a larger variety of possibilities for the Pacific wavetrains to develop downstream.

This "downscaling" approach may prove to be useful when the very fine details of a specific region are not resolved by numerical prediction models (i.e. over areas with complex orography) An example is presented in Fig. 5.15, which utilizes the same high resolution dataset over the region of the Alps as in section 3.10.

5.7 Discussion

We have illustrated how partitioning the record on the basis of the polarity of leading patterns of hemispheric variability of the SLP field yields distinctive "subclimatologies" (H1, L1, H2, L2...) whose individual maps exhibit remarkably different degrees and kinds of "case-to-case" variability. These 10-day mean ensembles can be considered as archetypical of the frequency distribution of hemispheric patterns

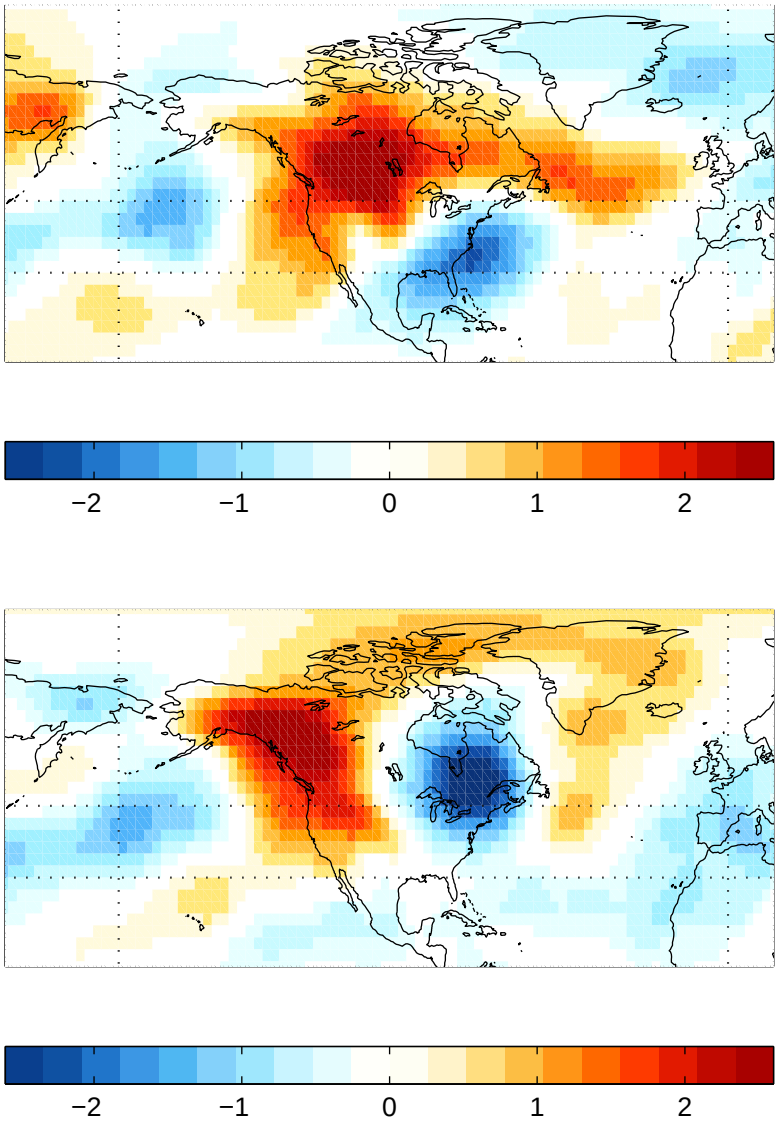

Figure 5.13: As in Fig. 5.8, but for 850 hPa temperature anomalies (K).

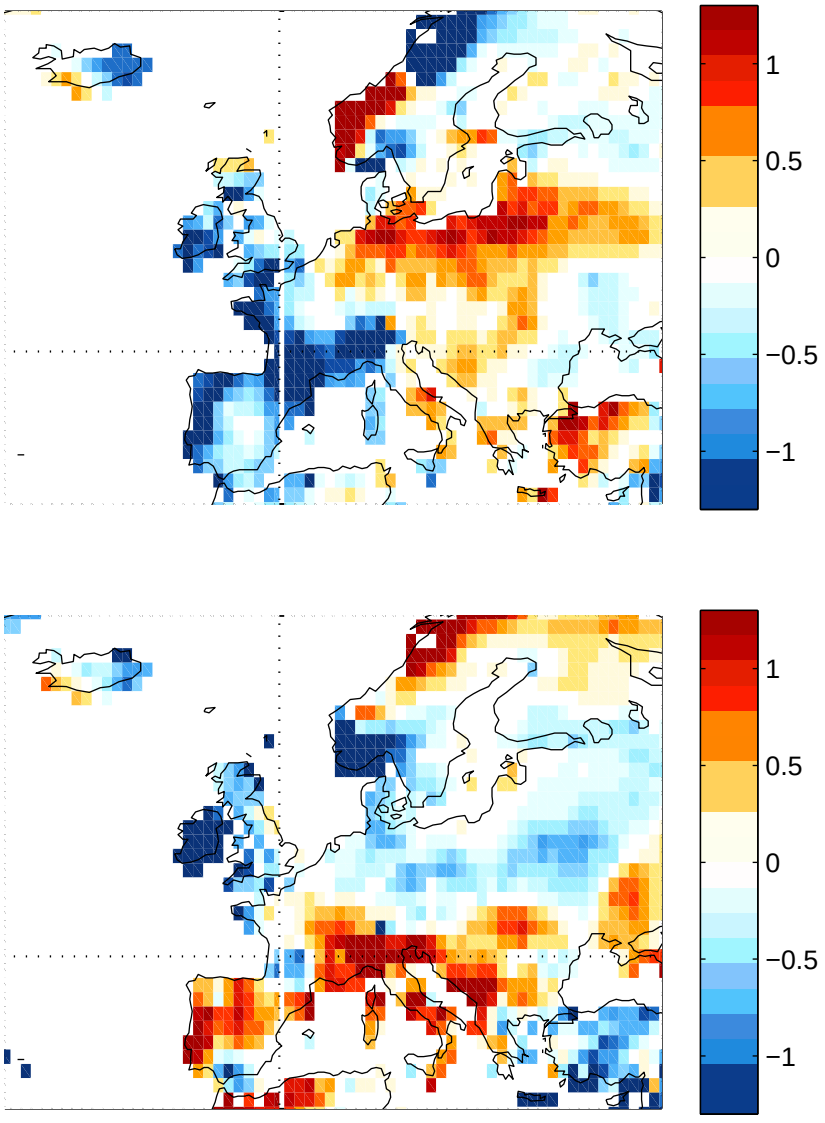

Figure 5.14: Precipitation anomalies over Europe regressed upon standardized time series of monthly SLP PC 2 for DJFM 1958-99, based on the subclimatologies of the data consisting of the 9 months with highest and lowest value of PC1. Willmott data. Units: (mm/day) (?).

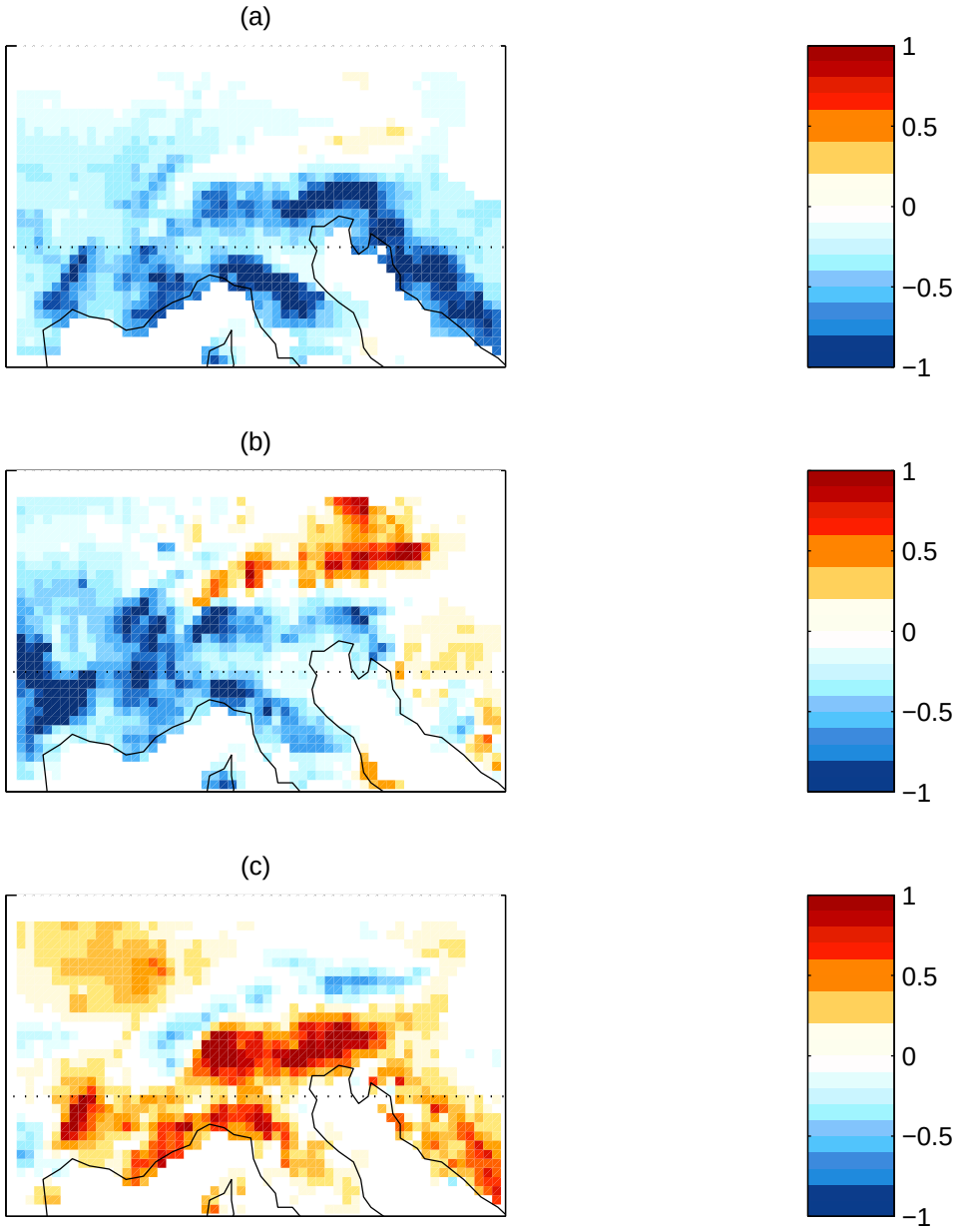

Figure 5.15: Precipitation anomalies over the Alpine region regressed upon standardized time series of monthly SLP PC 2 for DJFM 1971-1992, based on a) all months, b) the subclimatology of the data consisting of the 14 months with value of PC1 higher than 1 standard deviation, c) the subclimatology of the data consisting of the 12 months with value of PC1 lower than 1 standard deviation (mm/day).

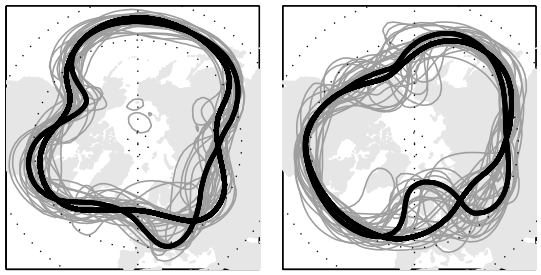

Figure 5.16: Plots of the 540 dam 500 hPa contour for the 30 dectads of "high index" and "low index" polarities of PC2, as in Fig. 5.6. The bold contours illustrate recurrent circulation types in the European sector. They represent averages over 8 contours with similar shapes in that region.

whose mean is reflected in regression maps based on the leading PCs of SLP.

The diverse flow patterns observed in each subclimatology are reminiscent of more regional "weather types" defined by Baur et al. (1944), Rex (1951), Vangengeim (1952), Girs (1974), among others. More specific weather types such the wave regimes over Europe illustrated in Fig. 5.16 tend to occur in association with high and low index subclimatologies of the PCs.

The enhanced (or reduced) variability of the flow in each of these subclimatologies is reflected in enhanced (or reduced) variability of surface weather conditions. For example, the standard deviation maps shown in Fig. 5.17 clearly show that lower tropospheric temperature tends to be more variable over most continental regions in association with the low-index polarity of both patterns.

The influence of SLP PCs 1 and 2 upon the probability of occurrence of extreme cold events (defined as negative 1000-500 hPa thickness anomalies in excess of 2 standard deviations in the 10-day mean maps) is illustrated by the composite maps shown in Fig. 5.18. The vectors represent the mean standardized values of PC1 and PC2 during cold dectads. This pattern exhibits a number of subtle regional features indicative of departures from the linear behavior exemplified by Fig. 19 of Quadrelli

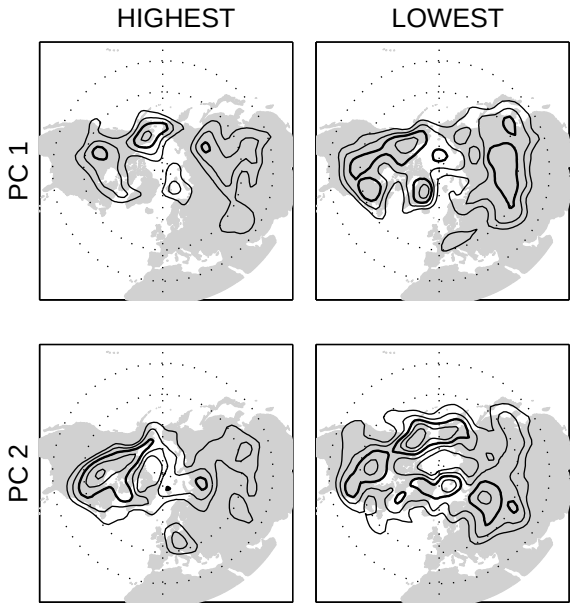

Figure 5.17: Standard deviation of 1000-500 hPa thickness for the 30 dectads with the most positive and the 30 decads with the most negative values of PC1 and PC2, as indicated. Contour interval: 10 m; the 85 m contour is bold.

and Wallace (2004a). For example, over western North America PC1 is uncorrelated with 850-hPa temperature, yet over parts of the region it tends to be negative during dectads in which temperature is well below normal.

That PC1 and PC2 have a stronger overall impact upon the frequency of occurrence of extreme cold events than would be expected on the basis of their linear correlations with monthly mean thickness is illustrated by Fig. 5.19. Within the closed contours, extreme cold is more than 20 times more likely when the PC is in its negative polarity (with standardized amplitude > 1.5) than when it is in its positive polarity. It is evident that the area enclosed by the contours substantially exceeds that expected on the basis of the linear correlations (indicated in the figure by the shading). Hence, it seems likely that the nonlinear relationships illustrated by the spaghetti diagrams contribute to the unexpectedly strong influence of PC1 upon the occurrence of extreme cold, as documented in Thompson and Wallace (2001), and

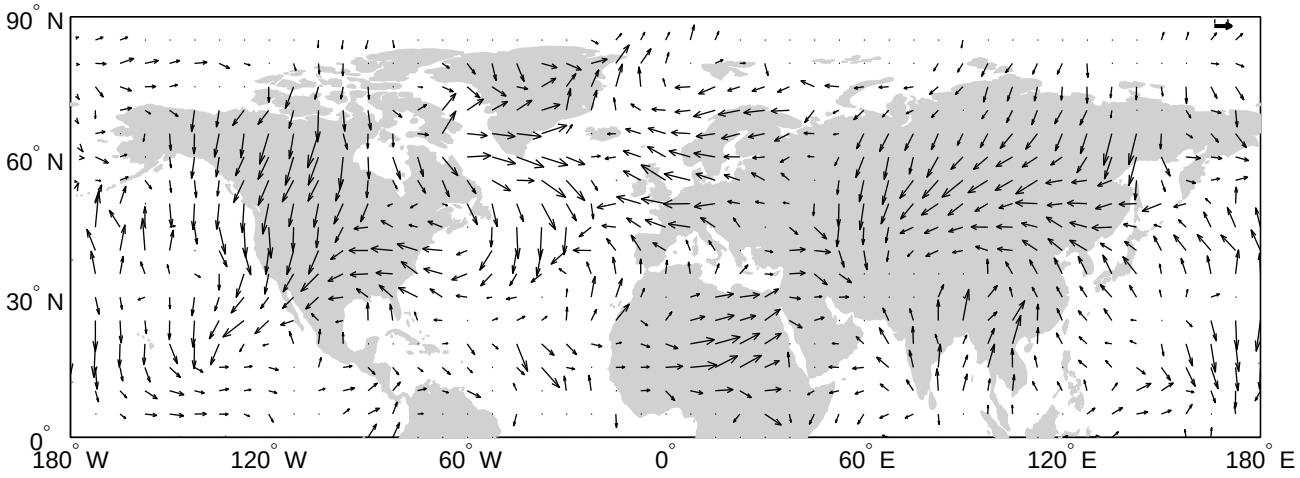

Figure 5.18: Composite map of values of standardized SLP PC1 and PC2 during extreme cold events defined as dectads with 1000-500 hPa thickness anomalies lower than 2 standard deviations. Arrows represent at each grid point the combination of PC1's (x-axis) and PC2's (y-axis) values. The length of the heavy arrows (upper right) represents one standard deviation.

presumably the same is true of PC2.

It remains to be seen whether the differences in flow variability observed for individual cases of 10-day means for contrasting polarities of the SLP PCs are representative of differences associated with lower frequency variations in the background flow upon which the dectad-to-dectad variability is superimposed. Figures 5.20 and 5.21 compare all dectads of the two winters with highest and lowest values of the *seasonal mean* SLP PCs for two specified contours. The high- and low- index ensembles do not contrast as sharply with one another as in Figs. 5.3 and 5.6, but it is notable that the distinctions between the high- and low- index seasonal ensembles of Figs. 5.20 and 5.21 are qualitatively similar to their higher frequency counterparts. On this basis it can be argued that part of the contrast between the high- and low- index ensembles is due to systematic differences between the basic state flow in high- and low-index winters. Hence, the results shown in the chapter are also broadly indicative of the varied expressions of the hemispheric flow patterns observed in association with

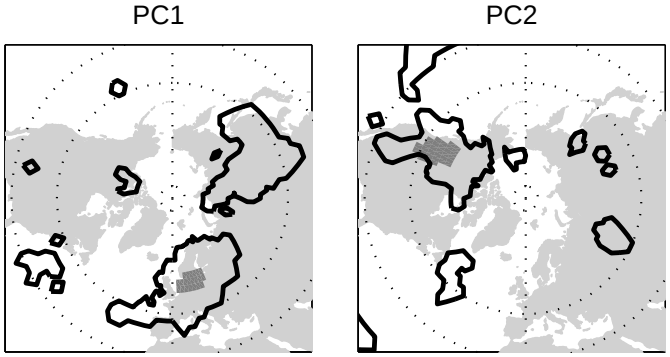

Figure 5.19: Contours enclose areas in which extreme cold events (dectads with negative 1000-500 hPa thickness anomalies in excess of 2 standard deviations) occur at least 20 times as frequently under hlow index conditions than under high index conditions of PC1 (left) and PC2 (right). Areas in which that ratio is expected to be exceeded based on the linear correlations between thickness and the PCs, assuming that the variables are normally distributed, are indicated by heavy shading.

different basic state hemispheric flow patterns.

The leading SLP PCs are more predictable on the seasonal and longer time scales than other patterns of variability: PC1 by virtue of its relation to volcanic eruptions, the equatorial stratospheric quasi-biennial oscillation, variations in the strength of the wintertime stratospheric polar vortex (Thompson et al., 2002a) and possibly to slow variations in sea surface temperature in the equatorial western Pacific and Indian Oceans (Hoerling et al., 2001), and PC2 by virtue of its relation to decadal-scale ENSO-like variability in the Pacific (Zhang et al., 1997; Mantua et al., 1997). Hence the results presented in this chapter may have some practical implications for extended range statistical prediction of extreme events.

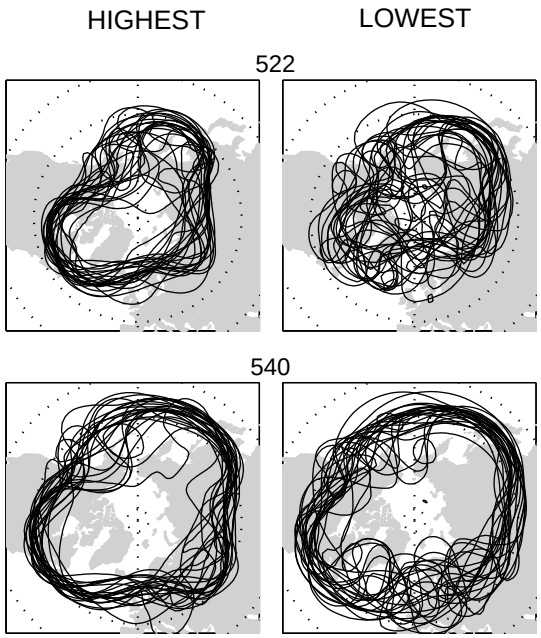

Figure 5.20: As in Fig. 5.3 but for specified 500 hPa contours for the 24 10-day means belonging to the two winters with highest values of seasonal SLP PC1 (1993 and 1989) and the two winters with the lowest values (1969 and 1960)

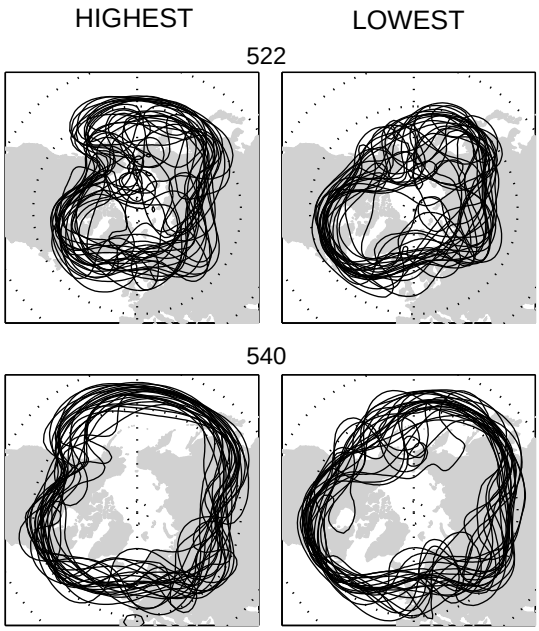

Figure 5.21: As in Fig. 5.6 but for specified 500 hPa contours for the 24 10-day means belonging to the two winters with highest values of seasonal SLP PC2 (1998 and 1983) and the two winters with the lowest values (1972 and 1989)

Chapter 6

INFLUENCE OF ENSO: NORTHERN ANNULAR MODE AND TRENDS

6.1 Introduction

Externally forced modes of variability can be viewed as modulating the basic state for the atmosphere's internal variability. While the discussion so far has focused on the internal variability of the extratropical circulation, in this chapter we study an indirect effect of tropically forced variability on our phase space: the influence of the change in climatological background flow associated with the ENSO cycle upon the structure of the first basis function, the northern annular mode. From this starting point, we will show that a series of more general results can be obtained by stratifying the data according to the polarity of ENSO, including a surprising description of the observed trends in surface air temperature.

The typical anomaly induced by ENSO is shown for the 200 hPa zonal wind in Fig. 6.1; it is clear that the mean response to ENSO has a global character, and it is not restricted to the Pacific region. It is reasonable to investigate whether the main patterns of extratropical variability will be affected by this change in the background flow. Therefore, in this chapter we will consider two subsets of the data characterized by warm and cold ENSO events as separate datasets, in which to study differences in variability. The midtropospheric mean and variance maps associated with our two subsets are shown in Fig. 6.2 for the 500 hPa geopotential height monthly field.

This chapter is comprised of 7 sections. Section 6.2 describes the main differences in structure of the NAM during warm and cold winters of the ENSO cycle; section

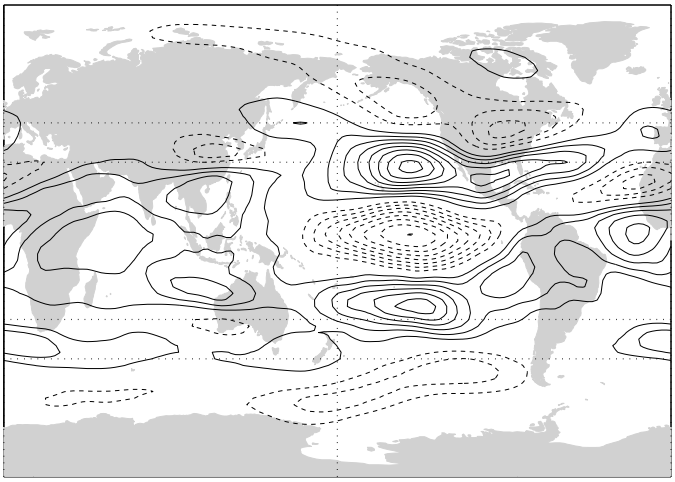

Figure 6.1: Regression map of zonal 200 hPa wind upon DJFM monthly time series of CTI. Contour interval 0.75 ms^{-1}; the zero contour is omitted.

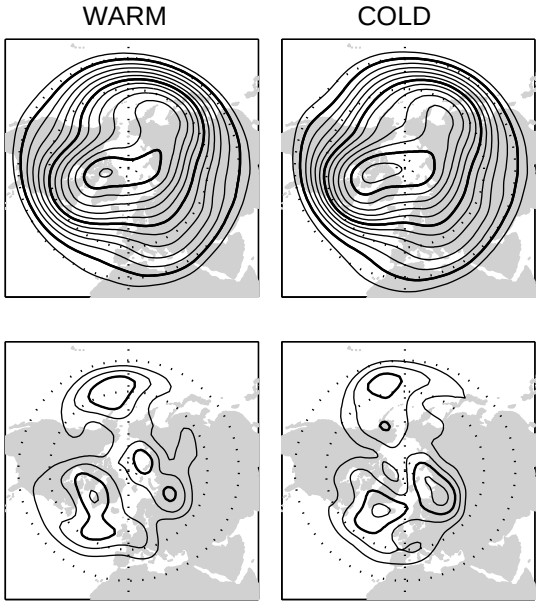

Figure 6.2: Mean and variance maps of the 500 hPa height field for the two subsets of 10 day running monthly means included in the warm and cold ENSO composites. Contour interval every 60 m, bold: 5100, 5400, 5700 m (upper panels); every 15 m, bold: 90 m (lower panels).

6.3 discusses the relation between some of those changes and the differences in the mean background flow between the two subsets; an analogy with variations associatd with the seasonal cycle is also presented. Section 6.4 briefly discusses some aspects of the relation of the southern counterpart of the NAM with the changes in the mean flow associated with ENSO. Section 6.5 investigates the frequency dependence of some of the differences seen in section 6.2, and introduces a time scale separation between interannual (wintertime mean data) and intraseasonal (departure of montthly mean from wintertime mean data) variability. This frequency separation leads to a discussion of longer term variability presented in section 6.6, where trends in the observed record are stratifed according to the polarity of the ENSO cycle. A discussion of the results is offered in section 6.7.

6.2 Influence of ENSO on the structure of the NAM

In this section we analyze the differences, mainly in structure, of the NAM, as deduced separately for the warm and cold ENSO subsets. Each result presented has been tested by comparison with statistics obtained with Monte Carlo experiments; the estimated probability of getting such a result by chance is given as a p-value, as described in section 2.3.

6.2.1 Explained variance

The leading EOF for the ENSO warm composite explains a higher percentage of the total variance of the SLP field than most of the first EOFs based on randomly chosen 14-winter composites (31.7%, p=0.07) versus 24.7% for the cold composite. In both composites the second EOF accounts for less than 15% of the variance.

The lagged autocorrelation of the daily time series of the NAM for warm and cold ENSO composites exhibits a consistent behavior, as shown in Fig. 6.3: during warm ENSO winters the NAM is more persistent, exhibiting higher autocorrelation at every

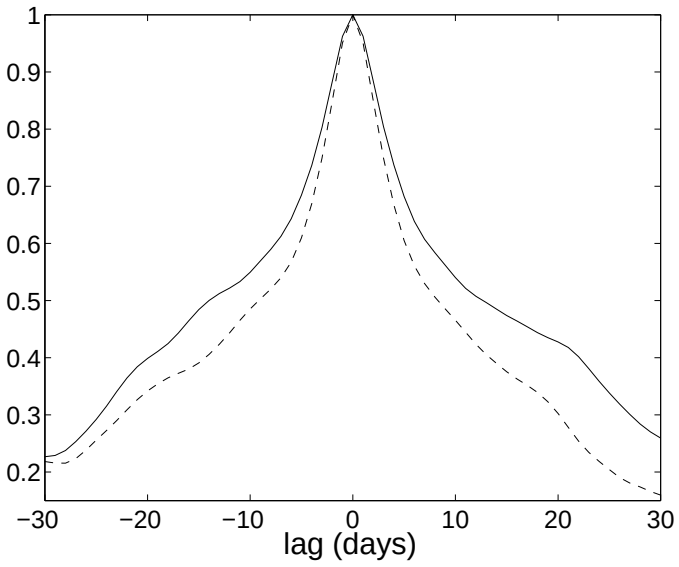

Figure 6.3: Lag correlation of a daily DJF time series of the NAM for warm (solid) and cold (dashed) winters of the ENSO cycle.

lag.[1]

6.2.2 SLP signature

The leading EOF for the cold ENSO composite exhibits a pronounced positive center of action over the North Pacific, whereas the one for the warm composite does not (Fig. 6.4).[2] This distinction is reflected in the difference in correlation between SLP raw data in 15°lat ×50°lon grid boxes centered on Pacific gridpoint P (37.5°N, 155°W) and Atlantic gridpoint A (37.5°N, 25°W): 0.41 for cold composite vs -0.16 for the warm composite (p=0.016).

---

[1]The asymmetry in shape of the autocorrelation of Fig. 6.3 is due to the inclusion of November data for the negative lags and of March data for the positive lags.

[2]The analysis was repeated in a North Atlantic Oscillation (NAO) framework. A monthly time series of the NAO was obtained by projecting area-weighted monthly SLP anomalies upon the SLP regression map associated with the DJFM seasonally averaged index of the NAO, as defined in (Hurrell, 1995). The SLP regression patterns of the NAO computed separately for warm and cold winters of the ENSO cycle (not shown) exhibit the same distinctions as the patterns derived from EOF analysis of the SLP fields, and they are of comparable strength.

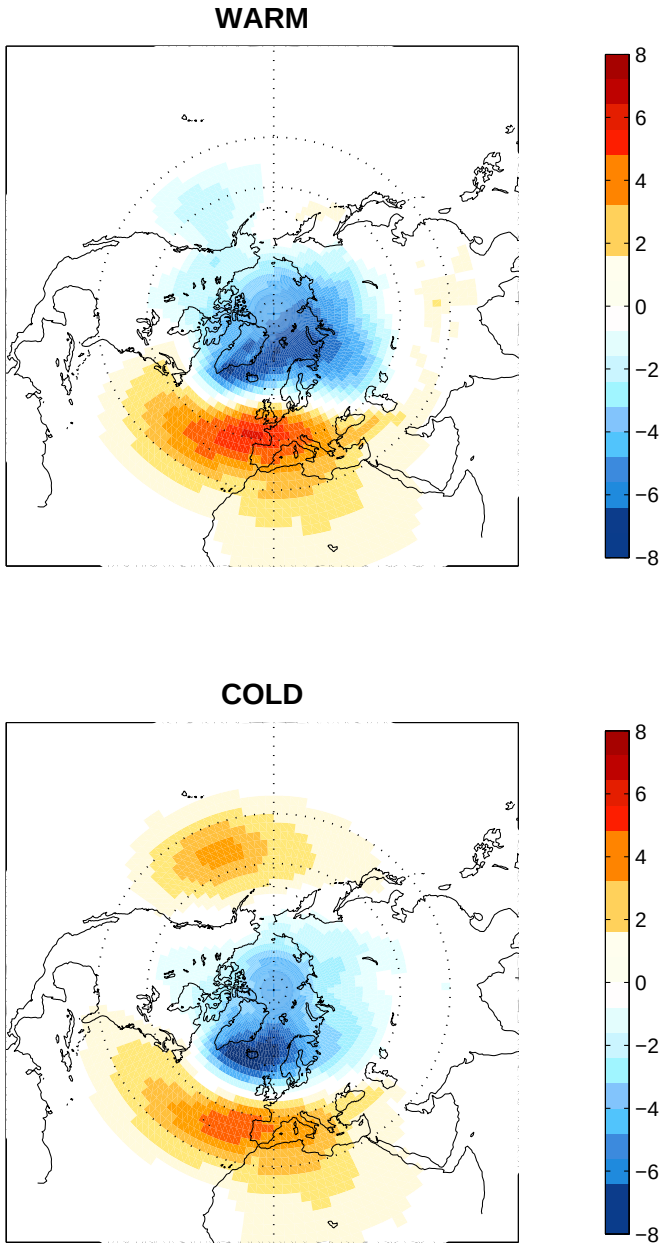

Figure 6.4: Monthly mean SLP field regressed upon standardized PC 1 of monthly mean DJFM SLP anomalies poleward of 20°N, as computed separately for the ENSO warm and cold composites, based on 10-day running 30-day mean DJFM data for the period 1958-1999. Contour interval 1.5 hPa. Negative contours are dashed, and the zero contour is omitted.

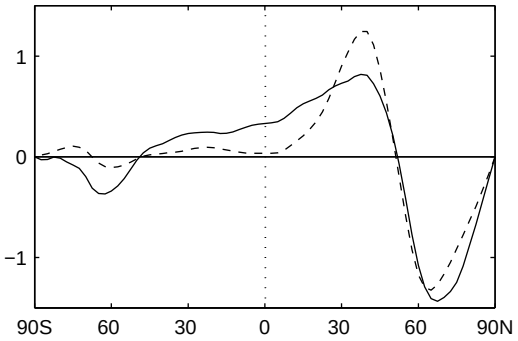

Figure 6.5: Area-weighted meridional profile of zonally averaged SLP (arbitrary units) corresponding to the SLP regression maps shown in Fig. 2; solid line the ENSO warm composite; dashed line the ENSO cold composite.

6.2.3 Tropical extent

The leading EOF for the warm composite exhibits larger amplitude in the tropics, as documented in Fig. 6.5. The fraction of the mass in the outer ring of the SLP regression pattern that lies between 20°S and 20°N is higher for the warm composite than for most randomly chosen 14-winter composites (p=0.03), and lower for the cold composite than for most randomly chosen composites (p=0.005). Consistent with this result, the outer ring in the zonally averaged SLP profile is more sharply peaked in the cold composite, and tropical (20°S-20°N) SLP exhibits a stronger anticorrelation with polar (65°-90°N) SLP in the warm composite than in most randomly chosen 14-winter composites ($-0.64, p = 0.02$).

The deeper penetration of the outer ring of the NAM-related SLP perturbations into the tropics during the warm phase of the ENSO cycle is consistent with the mean equatorward displacement of the storm tracks shown in Fig. 6.6.

6.2.4 Other fields

The structural distinctions discussed in the previous sections have counterparts in other fields, dynamically consistent with SLP. Examples include surface air tem-

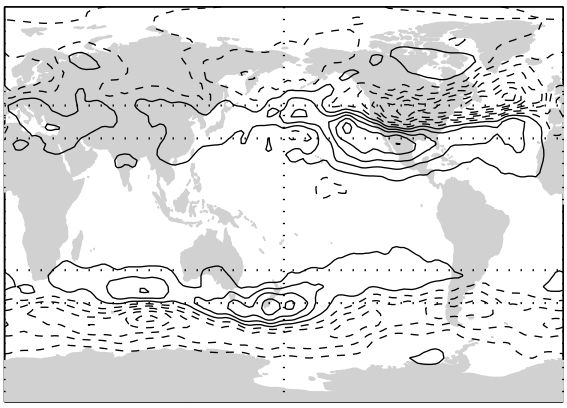

Figure 6.6: Difference between composite mean storm track fields (as defined by the variance of the running 1-day difference 300 hPa meridional wind component) for the 14 winters of the ENSO warm and cold composites: warm minus cold. Contour interval: 20 m^2 s^{-2}; negative contours are dashed; the zero contour is omitted.

perature (SAT), upper level zonal wind, and baroclinic activity, as presented in this section.

Consistent with the negative Arctic center extending farther into Siberia (Fig. 6.4), the NAM-related SAT perturbations over Siberia are stronger for the warm-ENSO subset, as shown in Fig. 6.7. Again, raw data confirm this difference: the SAT amplitude per standard deviation fluctuation of the leading principal component (PC1) of SLP averaged over the 15°lat × 30°lon box centered on (57.5°N,110°E) is 2.9°C for the warm composite as compared to 1.9°C for all winters (p=0.03). The stronger involvement of northern Siberia in the NAM during warm ENSO years is also reflected in one-point correlation maps for SLP and SAT (not shown).

Consistent with the distinction between the warm and cold composite SLP pattern, baroclinic wave activity at the jet stream level exhibits stronger NAM-related perturbations over the Pacific sector in the cold composite, as shown in Fig. 6.8. As in the Atlantic sector, the anomalies in the intensity of baroclinic wave activity lie poleward of the midlatitude center of action of the NAM.

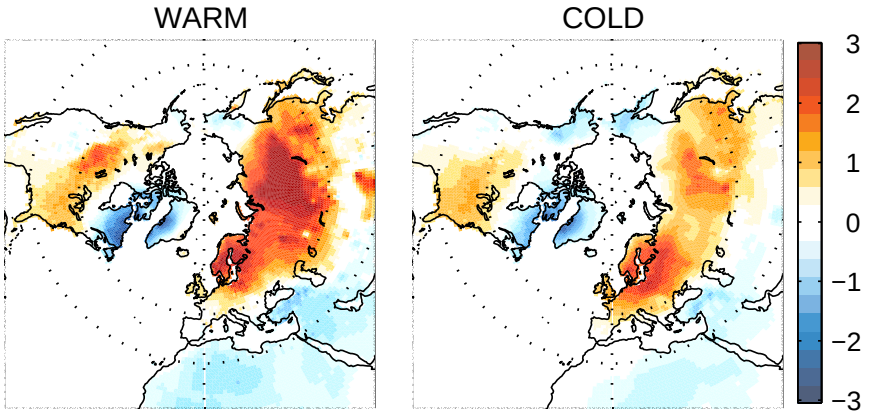

Figure 6.7: As in Fig. 6.4 but for surface air temperature (SAT).

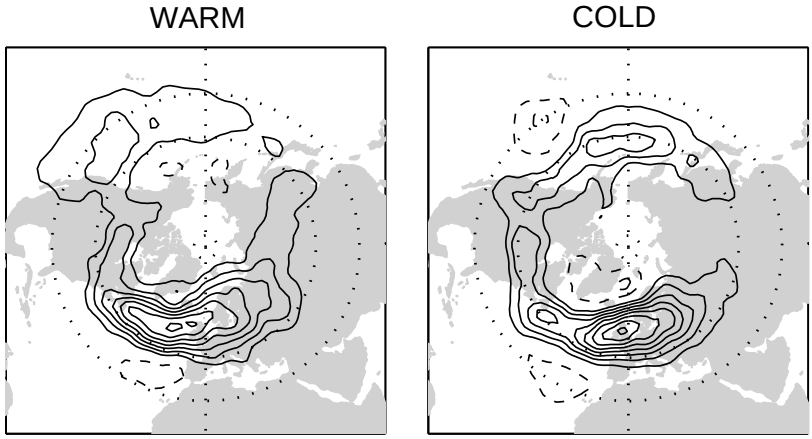

Figure 6.8: As in Fig. 6.4 but for the monthly mean storm track field as defined by the variance of the running 1-day difference 300 hPa meridional wind component. Contour interval: 40 m^2 s^{-2}; negative contours are dashed; the zero contour is omitted.

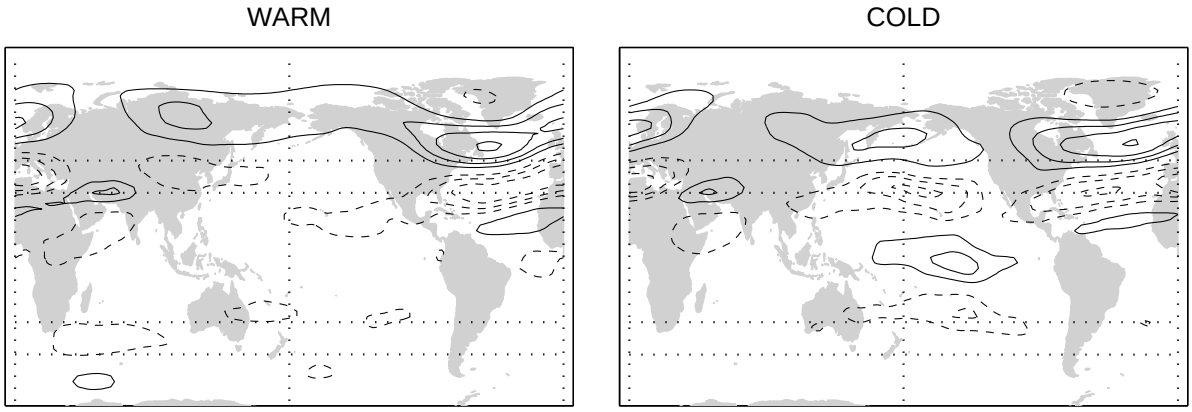

Figure 6.9: As in Fig. 6.4 but for 200 hPa zonal wind. Contour interval $1ms^{-1}$; the zero contour is omitted.

The regression maps of the 200 hPa zonal wind (Fig. 6.9) show the Pacific center of action associated with the NAM for cold events. The upper level anomaly also propagates through the equatorial region, allowed by the upper level westerly anomalies there induced by the cold ENSO event (corresponding to reversed Fig. 6.1 conditions). Recent results of Thompson and Lorenz (2004) have confirmed this interhemispheric wave propagation during cold ENSO events for the anomalies associated with the daily NAM time series, for lags of one to two weeks.

6.3 Relation of NAM changes with mean ENSO-induced changes

s The more pronounced North Pacific center of the NAM during the cold phase of the ENSO cycle, as described in section 6.2, may be attributable to the existence of a more pronounced Pacific jet exit region, as shown in Fig. 6.10. A general circulation model run with idealized bottom boundary conditions exhibits a similar correspondence between midlatitude centers of action of the annular mode and breaks in the jet in the basic state tropospheric jet stream (David J. Lorenz, University of Washington, personal communication).

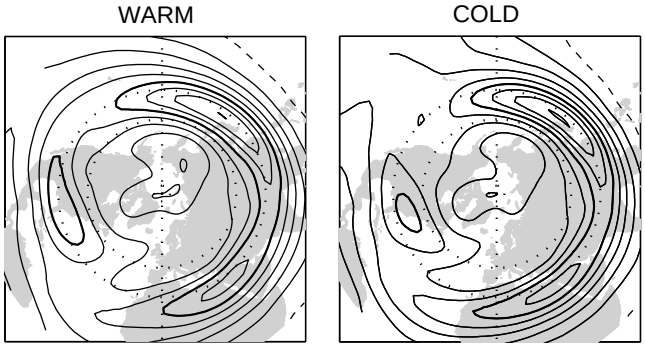

Figure 6.10: Mean of 200 hPa zonal wind for the 14 winters of the ENSO warm and cold composites, as indicated. Contour interval: 10 m s^{-1}; the 40 m s^{-1} contour is bold.

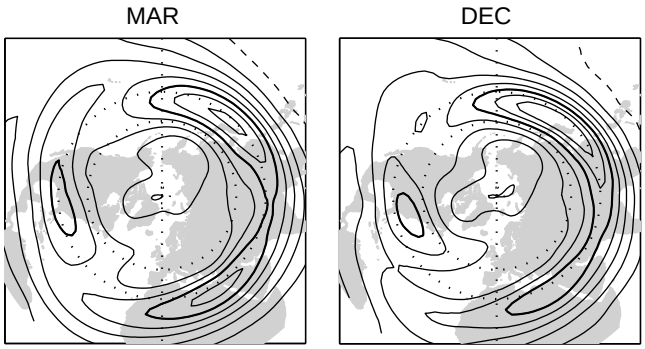

Figure 6.11: Mean of 200 hPa zonal wind for the 42 December and March months, as indicated Contour interval: 10 m s^{-1}; the 40 m s^{-1} contour is bold.

6.3.1 An analogy with the seasonal cycle

It seems reasonable to expect that the structure of the NAM should also vary with season in response to changes in the basic state. The evolution of the climatological-mean flow from early winter to late winter qualitatively resembles the change that occurs in response to a warming of equatorial Pacific sea surface temperature: the westerlies strengthen over the eastern part of the basin and the jet exit region over the Pacific sector becomes less distinct (Fig. 6.11). Figure 6.12 shows the leading

EOF of the SLP field, computed separately for March and December monthly mean SLP. In analogy with the ENSO composites, the explained variance of the March pattern is larger than that for the December pattern (29 vs. 17%), and the polar center of action extends deeper into Siberia. The Pacific center of action is evident in December, when the break between the Asian and North American jet streams is more distinct. The similarity between the ENSO and seasonal composites lends additional credence to the results presented in the previous section.

6.4 Southern annular mode differences

Here we address the question of whether the southern hemisphere counterpart of the NAM is characterized by a similar sensitivity to the mean background flow.

The southern hemisphere annular mode (SAM), as defined by the leading EOF of the monthly DJFM 850-hPa height field exhibits a dependence of its explained variance on the polarity of the ENSO cycle analogous to that mentioned in section 6.2.1: it explains 36% of the variance in the warm composite versus 29% in the cold composite.

We haven't analyzed the stuctural differences in the SAM induced by the ENSO cycle, but recent results by Codron (2004), based on observed and simulated data, confirm that the structure of the SAM does adapt to the changes in background flow observed in association with the ENSO cycle (and the seasonal cycle as well). In the southern hemisphere summer, where the variability is much more zonally symmetric than in the northern hemisphere, these changes are manifest mainly through a latitudinal shift of the SAM node following the mean jet shift (equatorward during warm events). The higher persistence in time during warm events, described for the NAM in section 6.2.1, is also confirmed for the simulated SAM.

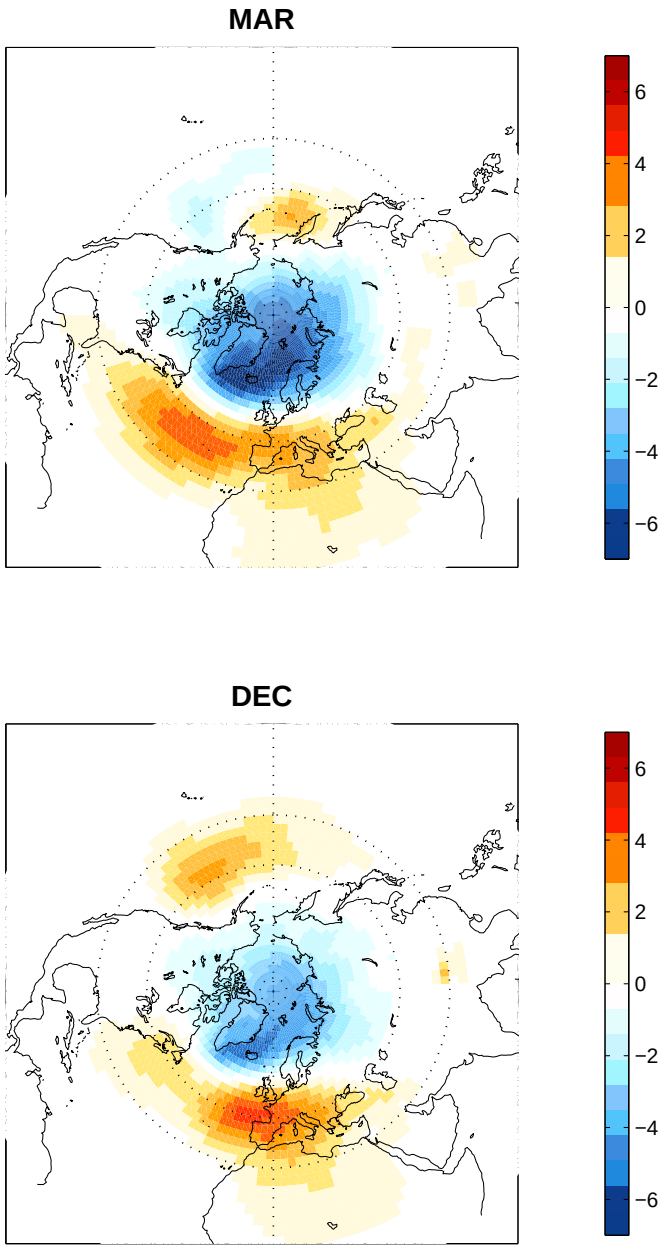

Figure 6.12: Monthly mean SLP field regressed upon standardized PC 1 of monthly mean DJFM SLP anomalies poleward of 20°N, as computed separately for the months of December and March for the period 1958-1999. Contour interval 1.5 hPa. Negative contours are dashed, and the zero contour is omitted.

6.5 Frequency dependence of the ENSO-induced changes

In analogy with the analysis performed in chapter 4 for the phase space, we present here a discussion of some differences observed in the troposphere and in the stratosphere between the warm and cold subsets.

Fig. 6.13 shows the extratropical SLP variance maps associated with the intraseasonal and interannual variability of the two subsets. On intraseasonal time scales, the cold ENSO subset exhibits higher variance, especially over the Atlantic and Eurasian sectors, than its warm counterpart. The zonally averaged profile also shows an equatorward shift of the variance maximum from cold to warm events, consistent with the mean shift of the storm tracks apparent in Fig. 6.6. On the interannual time scale the behavior is quite different: two latitudinal maxima are visible (corresponding to "dumbells" of variance in the horizontal maps), which are stretched farther apart during warm events. Moreover, the warm subset is characterized by an higher overall variance. In the next two sections we will present an example of differences in variability observed for each of these two time scales.

6.5.1 Intraseasonal variability: troposphere

We mentioned in section 6.2.2 that a significant positive correlation between east Pacific and Atlantic midlatitude SLP boxes appears during cold ENSO winters only. This behavior is particularly marked on intraseasonal time scales (Monte Carlo test, p=0.006); the 1-point regression map centered on a Pacific point is shown in Fig. 6.14. Results from GCM runs confirm the change in the correlation between Pacific and Atlantic sectors, as seen in observations: Fig. 6.15 replicates the results of Fig. 6.14, in experiments performed by Francis Codron (LMD, Paris) to study the variability of the Southern annular mode during control, warm ENSO, and cold ENSO years. The GCM is run in a perpetual March mode with fixed SSTs, and therefore reproduces only the intraseasonal component of the extratropical variability associated with the

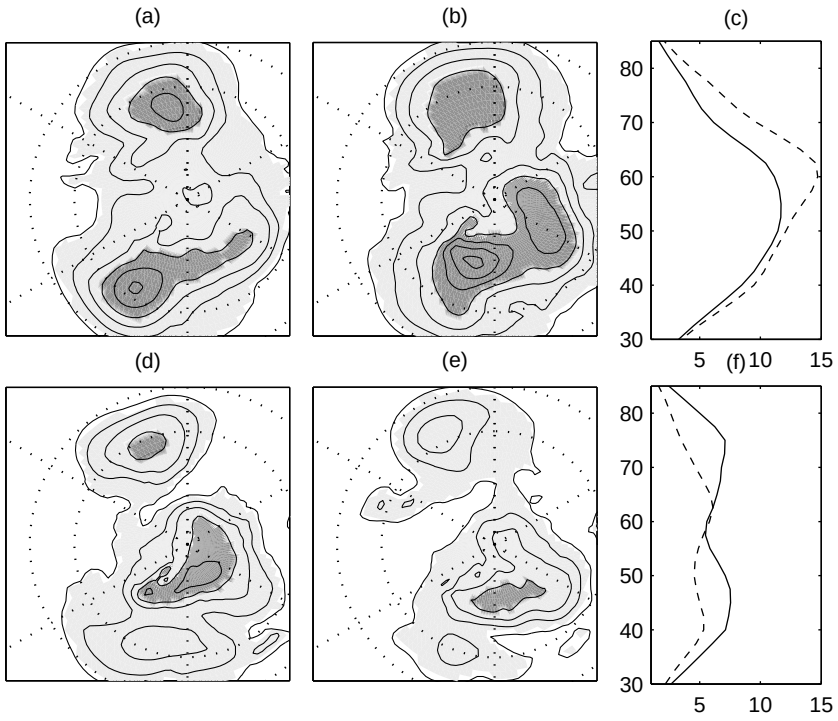

Figure 6.13: Intraseasonal (a-c) and interannual (d-f) SLP variance maps associated with the 14 warmest (a,d) and the 14 coldest (b,e) years of the ENSO cycle; (c,f): latitudinal profile of the area weighted zonally averaged SLP variance of warm (solid) and cold (dashed) composites. Map contours: 6 12 20 30 42 56 72 hPa^2.

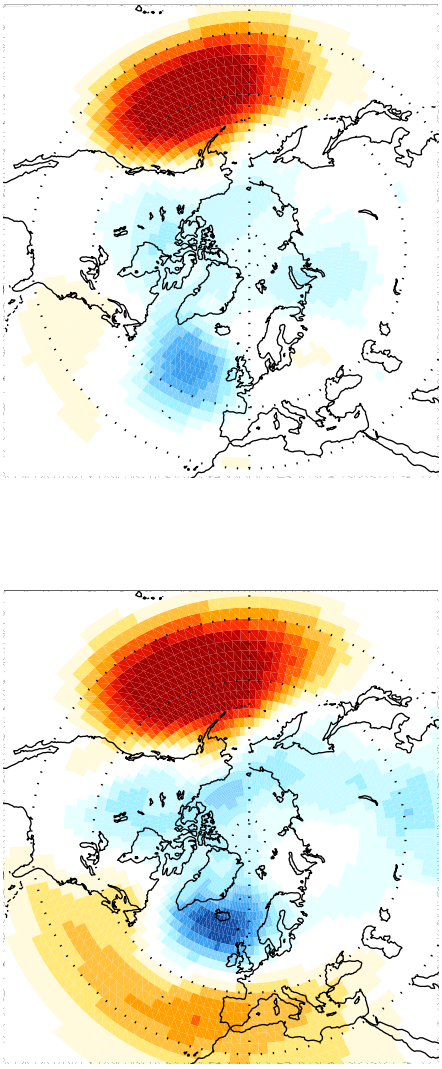

Figure 6.14: Regression maps of DJFM monthly intraseasonal SLP upon time series of intraseasonal SLP anomalies over the Pacific region (180-230°E, 35-45°N) for warm and cold ENSO composites.

SST forcing.

6.5.2 Interannual variability: stratosphere

A substantial part of the differences observed in the structure of the NAM between warm and cold ENSO years described in section 6.2 derives from its interannual component. Here we discuss the relation between surface and stratospheric levels. As shown in Fig. 6.16, the NAM shows a much more pronounced stratospheric signature during warm ENSO years; the correlation coefficient between the winter averaged NAM and 30 hPa leading PC is significant at the 98% level, based on Monte Carlo tests.

An analysis on two runs of the WACCM model forced by observed SSTs did not show an analogous sensitivity to the phase of ENSO.

That the relation of the NAM with its stratospheric counterpart is sensitive to the polarity of ENSO has implications for seasonal prediction. Results by Mark Baldwin (personal communication) confirm that the prediction of the NAM index, based on a lower stratospheric index of the annular mode, exhibits a higher skill during warm winters of the ENSO cycle.

The different behavior of the interannual NAM during warm and cold subsets may play a role in longer term trends, as discussed in the next section.

6.6 ENSO and observed trends

The SLP structure of the NAM observed during warm ENSO winters has a strong resemblance with the observed linear trend in SLP over the 1958-99 record (Fig. 4.8); the interannual SLP variability is higher during warm events (Fig. 6.13). Thus, one might question whether ENSO may have influenced the observed trends. We show in fact in this section that sea level pressure, surface air temperature and other dynamically consistent climate fields have exhibited especially strong trend patterns

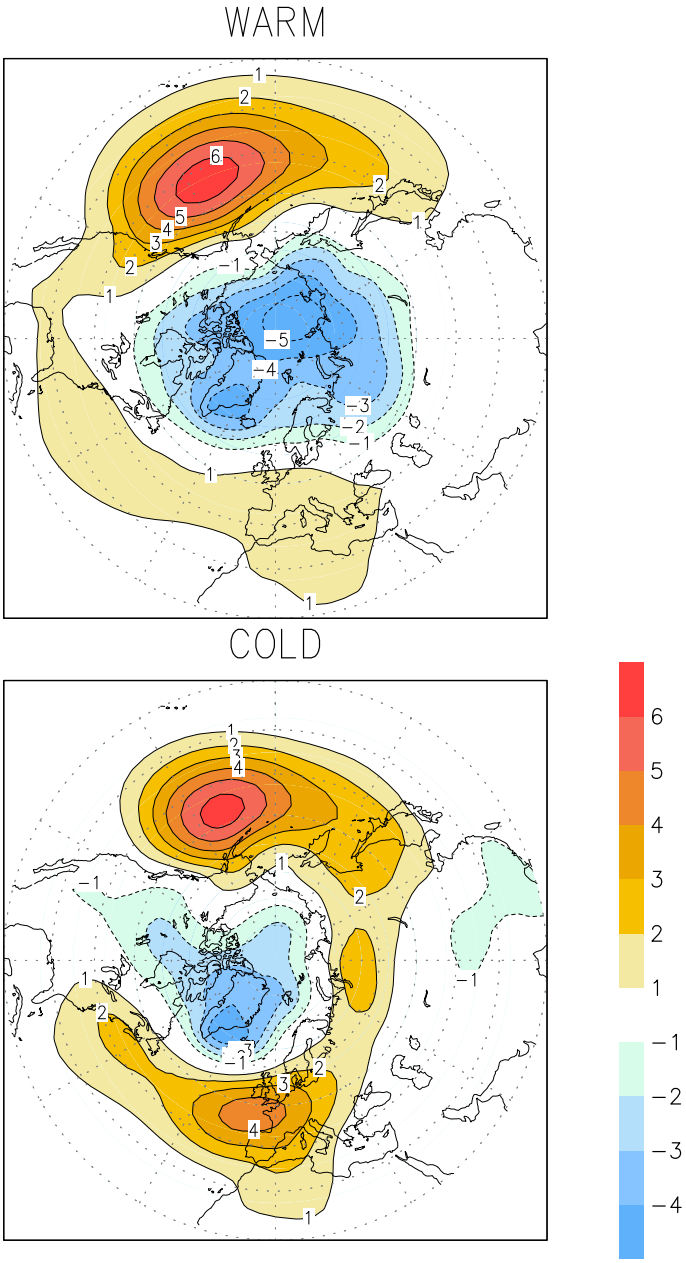

Figure 6.15: Pacific 1-point regression maps of monthly SLP for two LMDZ GCM runs with constant warm and cold ENSO SSTs, perpetual March. Courtesy of Francis Codron.

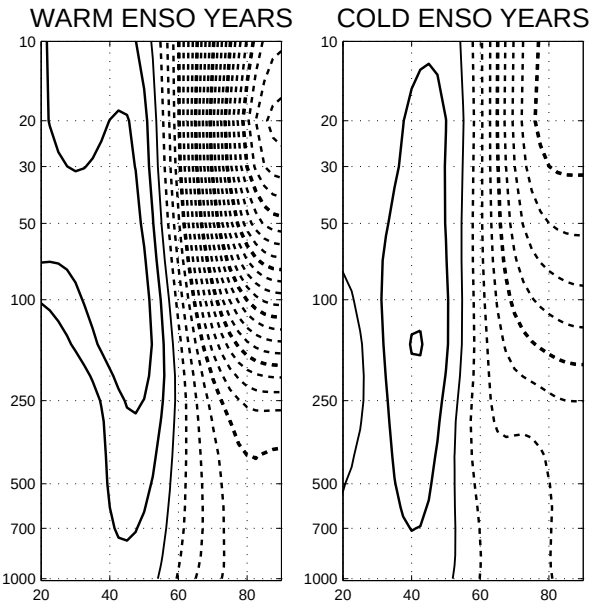

Figure 6.16: Vertical and latitudinal profile of the geopotential height regression onto the winter (DJFM) averaged NAM time series, for the subsets of the 14 warmest and 14 coldest ENSO winters of the period 1958-1999 (NCEP Reanalyses).

over the Northern Hemisphere during El Niño winters of the last 40 years.

6.6.1 Surface trends

The total wintertime linear trends observed for sea level pressure and surface air temperature during the period 1958-1999, as discussed in section 4.3, are reproduced in Fig. 6.17 (in a different color scale).

As shown in Fig. 6.18, it appears that the observed total trend of SLP and SAT of Fig. 6.17 can be almost fully explained by the linear trend observed only during the top third years of most positive values of the ENSO cycle, while the cold (as well as the remaining) part of the record does not show a trend of comparable strength.[3]

[3]The time series of CTI itself shows a trend towards more positive values over the record. However, the structure of the observed extratropical surface trends is different, in shape and intensity, from a direct CTI signature.

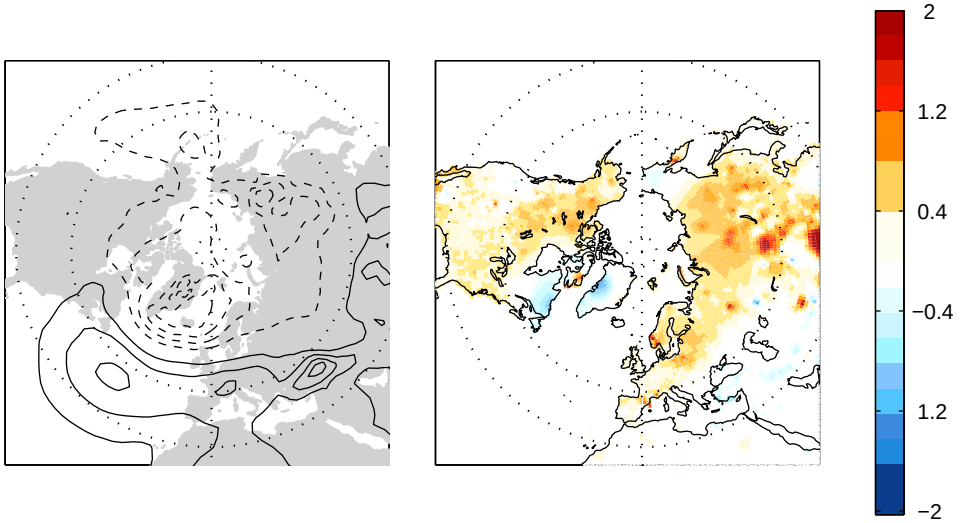

Figure 6.17: Total DJFM wintertime SLP and SAT trends over the Northern Hemisphere for the period of the record 1958-1999, as computed by linear regression. SLP contours every 0.5 hPa per 12 yrs; SAT contours: degrees per 12 yrs. SLP data: NCEP-NCAR Reanalysis. SAT data: Willmott dataset.

The fact that this "dynamically induced" pattern of SAT trend includes regions of cooling is probably a reason why the simple hemispheric mean land temperature time series does not show a more significant trend during the same 14 warmest ENSO years than in other subsets of the record.

Incidentally, we note that the southern hemisphere does not show such a different behavior of linear trends in the two different subsets.

6.6.2 Significance testing

The result shown in fig. 6.18 has been tested through Monte Carlo experiments in which SLP and SAT trend were computed for 1000 randomized 14-year subsets of the full record. The strength of each of the 1000 resulting trends, computed as root mean square of the area-weigthed pattern over the region poleward of 20°N, is used as a measure of the strength of the trend in random realizations, which is compared with

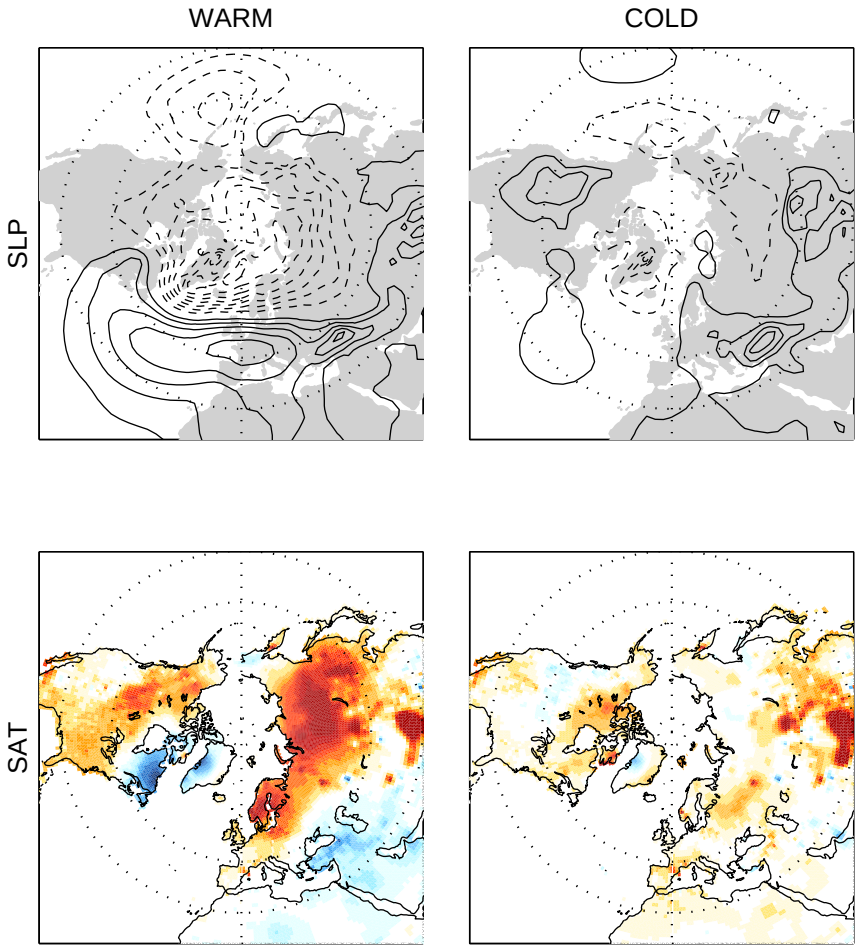

Figure 6.18: Wintertime DJFM SLP and SAT trends for the period of the record 1958-1999 as calculated separately by linear regression for the 14 warmest and the 14 coldest years of the ENSO cycle. SLP contours every 0.5 hPa per 10 yrs; SAT contours every 0.4 degrees per 10 yrs. same units as Fig. 6.17

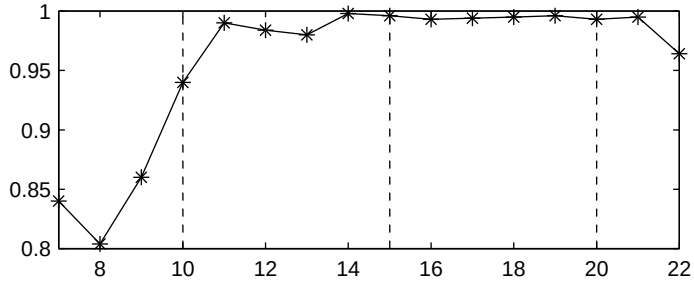

Figure 6.19: Percentile of the root mean square of surface air temperature trend patterns versus the number of years -sorted according by CTI intensity- included in the warm ENSO category, compared to Monte Carlo experiments. See text for further explanations.

the one subset comprising of the 14 years with highest CTI value. The trend exhibited by the warm ENSO subset is stronger than 995 subsets out of 1000 randomly chosen subsets. A generalized version of this Monte Carlo experiment has been performed to test the sensitivity of the results to the subset size. Figure 6.19 shows the percentile value of the SAT trend strength of the warmest N-year ENSO subset, compared to 1000 Monte Carlo N-year subsets, repeated varying the number N of years included in the warm category. The significance level of the result is well above 99% for subset sizes ranging from 14 to 21 years (that is highest CTI one third to one half of the record), above 98% for sizes ranging from 11 to 21 years, and above 80% for sizes ranging from 7 to 21 years. For the shorter sample sizes it is reasonable to expect a high sampling variability.

The robustness of the results was also tested by removing each year of the warm subset before computing the linear regression, in order to exclude the possibility of having obtained a strong trend pattern that was largely due to a single outstanding data point. The 14 resulting maps (not shown) are qualitatively similar to the one shown in Fig. 6.18 for the full subset. Removing the two strongest warm episodes of the ENSO cycle (1982-83 and 1997-98) had little effect on the results.

6.6.3 Upper level trends

Besides the large differences between the warm and cold subsets shown for the surface trends, differences in structure are observed throughout the entire troposphere and the lower stratosphere. Figure 6.20 shows the vertical structure of the trends for zonally averaged geopotential height and temperature, in the full record, and in the two different subsets.

A strong polar stratospheric cooling trend is observed only during the warm ENSO composite, in association with trends toward lower geopotential heights at tropospheric levels over the polar cap. A horizontal view is presented in Figure 6.21, for 30 hPa geopotential height.

The Monte Carlo significance level of the stratospheric strengthening of the vortex during warm years, computed as the linear trend in the zonally averaged height poleward of 65°N, averaged over the levels of 30, 50, 70 hPa is 98%. However, in this case the significance level is more sensitive to the sample size than the results for SLP and SAT at the earth's surface.

6.7 Discussion

The first result we have shown is that the NAM appears to be pliable to some degree; i.e., its structure adapts to changes in the basic state observed during opposing phases of the ENSO cycle. Probably other mean climatological changes would affect the NAM; a cursory analysis of NAM-related statistics for December and March suggests in fact that the structure of the NAM exhibits a seasonal evolution analogous in many respects to the changes observed in association with the ENSO cycle.

Our results suggest that the impacts of the NAM upon regional climate may prove to be even stronger than reported in chapters 3 and 5 if systematic changes in its structure that occur in response to variations in the basic state are taken into account in the analysis scheme. For example, one might expect the impact of the

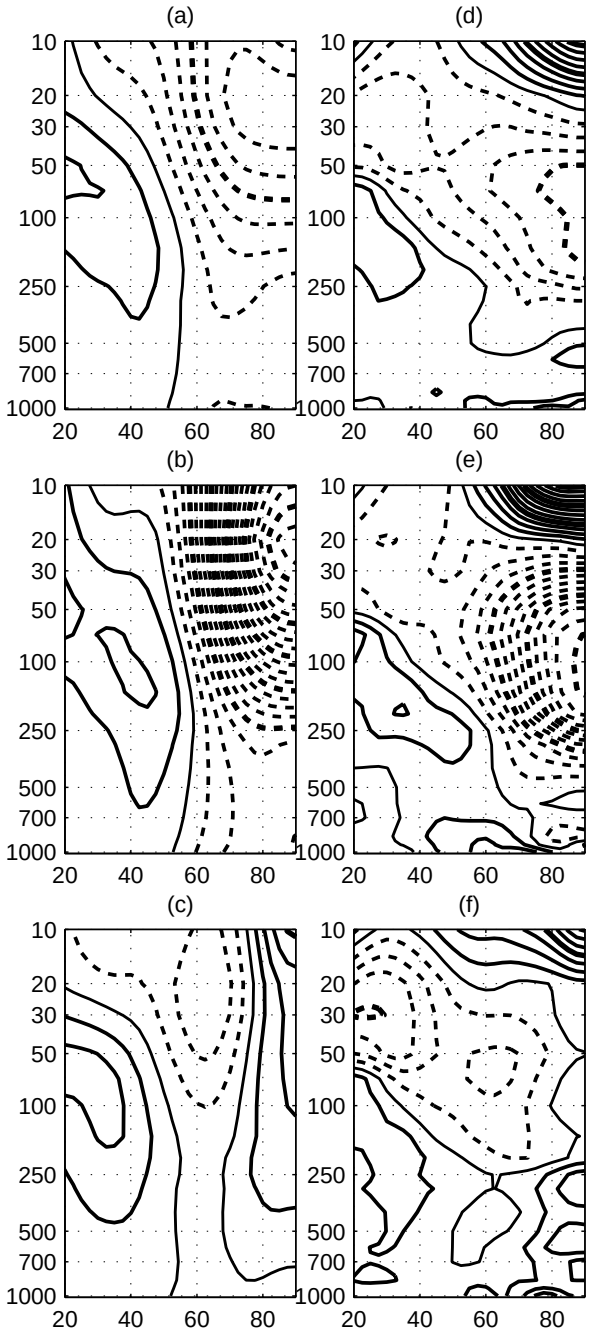

Figure 6.20: Wintertime DJFM vertical profile of zonally averaged (a,b,c) geopotential height and (d,e,f) temperature trends for the period 1958-1999. a,d: total trends; b,e: 14 warmest ENSO year trend; c,f: 14 coldest ENSO year trend.

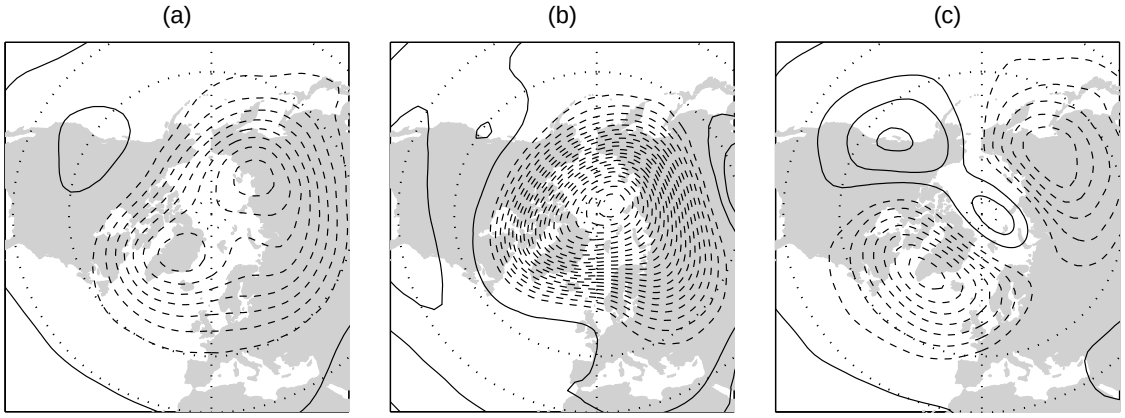

Figure 6.21: Wintertime 30hPa geopotential height trends for the period 1958-1999. a: total trend; b: 14 warmest ENSO years trend; c: 14 coldest ENSO year trend. Contours every 10 m per 12 years.

NAM upon winter temperatures over much of Siberia to be stronger during warm phases of the ENSO cycle than during cold winters, and the reverse to be true for rainfall over the British Isles.

The second major result is the extension of the idea of changes in mean background flow affecting the variability to explain differences in observed trends. We hypothesize that the trends observed in the period 1958-1999 were stronger during the subset of the record characterized by warm ENSO events. This result is quite striking, but nonetheless it is unluckily subject to the caveat of dealing with just a "one realization"-ensemble (the observations). In the context of "climatic change", say due to anthropogenic greenhouse forcing, the intriguing hypothesis underlying it is the possibility of having different dynamical responses to the same external forcing if the mean states of the atmosphere are different enough during the warm and cold phases of ENSO.

Our result does not contradict recent observations by Hoerling et al. who argue that the NAO trend is forced by a warming of tropical Pacific and Indian SSTs; the positive ENSO phase is indeed associated with warmer anomalies of SSTs over

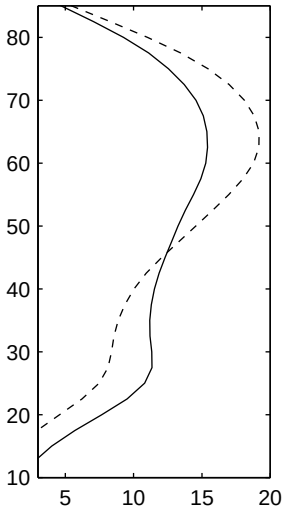

Figure 6.22: Latitudinal profile of winter (DJFM) mean zonally averaged 50 hPa zonal wind during warm (solid) and cold (dashed) ENSO years.

the tropical Pacific and Indian areas that they identify as key regions of warming associated with the extratropical NAO trend.

Besides the tropical forcing, we want to mention the role of stratospheric dynamics as a possible cause of the non linear kind of behavior documented in the previous subsections. ENSO itself has been shown to directly influence the stratospheric polar vortex (van Loon and Labitzke, 1987). Its signature in the polar vortex appears to be weakly nonlinear, with stronger anomalies observed during warm than during cold ENSO winters. The polar vortex tends on average to weaken during warm ENSO events, as shown in Fig. 6.22. However, the pattern obtained by regressing the stratospheric geopotential height field upon the CTI index does not look stationary in time (Fig. 6.23), and Labitzke and Collaborators (2002) postulated that the effect of ENSO upon the vortex is limited to the winters of years in which the QBO is in its easterly phase and there are not volcanic eruptions. This hypothesis looks certainly difficult to test on the observation record, because of the lack of a sufficient number of degrees of freedom. However, if a warm ENSO event can weaken the vortex

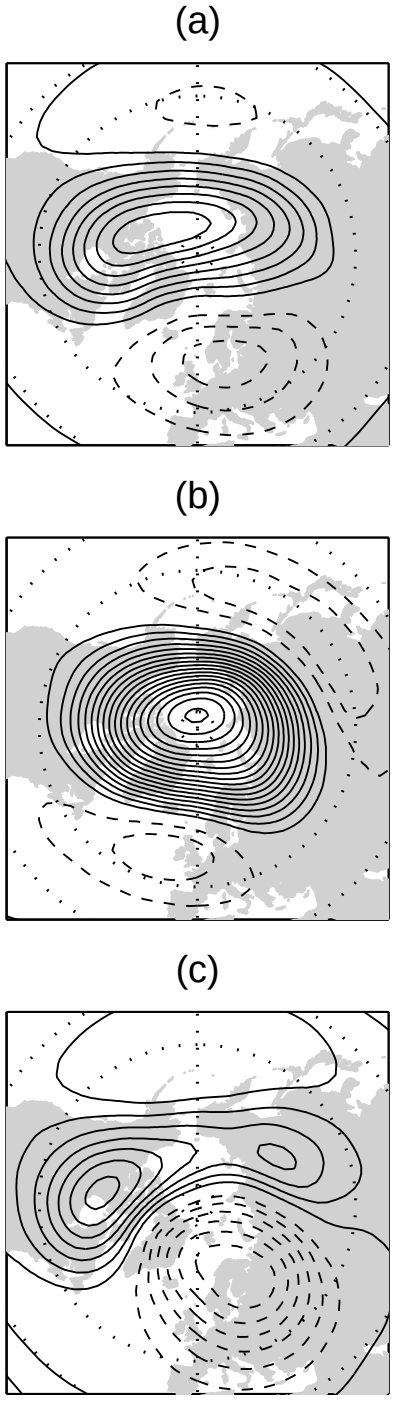

Figure 6.23: CTI winter regression on 30 hPa geopotential height. (a): 42 years, (b) first half, (c) second half of the record. Contours every 10 m

enough to favor sudden warmings, it is plausible that this mean state may be more sensitive to an external radiative forcing: cooling due to increasing greenhouse gas concentrations should tend to strengthen the vortex and suppress sudden warmings. The cold ENSO state, already characterized by lack of sudden warmings, would feel little effect from the same external forcing. For example, from preliminary results of Rolando Garcia on the WACCM model (NCAR, personal communication), there seems to be the same kind of relation between weak vortex events and warm ENSO years which can be seen in observations. Also, Taguchi and Hartmann (2004) obtain an increase of stratospheric sudden warmings in the same model, when forcing it with warm ENSO SST anomalies.

Chapter 7

CONCLUDING REMARKS

We offer here a brief discussion of the results of this thesis, in relation to the issues outlined in the introduction. The three sections of this chapter refer to the topics presented in the first three sections of chapter 1.

7.1 The need for synthesis

We have shown that two basis functions combined together can explain a high percentage of the month-to-month wintertime variability of the northern hemisphere circulation. Therefore, we suggest that definitions of new patterns be restricted to cases in which significant information is added to that already implicit in this two-dimensional phase space.

By focusing on the combined effects of the leading patterns of variability rather than on the structure of the individual patterns, we have circumvented the question of which is the best way to define any particular mode. The choice of the basis functions is to some extent subjective, but among the merits of selecting the leading EOFs of the monthly SLP field are:

- they are derived using an entirely objective procedure that requires a minimum of a priori specifications on the part of the analyst;
- by construction they explain the highest percentage of the variance of SLP;
- they are subject to the smallest possible sampling errors in the troposphere, given the available record;

- they correspond closely to the leading EOFs of variables such as 500-hPa height, wind, and surface air temperature.

The two time series associated with NAM and PNA pattern are also reasonably well predicted by medium range operational models, as shown in Fig. 7.1, which presents 7-, 10-, and 14-day forecasts by the medium range forecast (MRF) model of the Climate Prediction Center for the summer 2004; better scores are usually obtained during the winter season. In particular, the PNA pattern was found to be the most predictable pattern (Renwick and Wallace, 1995).

This phase space is well suited for comparisons of month-to-month patterns of variability found in observations, or in model output data. Furthermore, we have seen that the prominence of this two dimensional phase space is even higher for longer term variability, and dominant in the linear trends observed in the last 50 years of the record. Therefore, observational and modeling studies of climate change over the northern hemisphere might be facilitated by focusing on the large scale features described by this phase space.

7.2 Dynamical concepts

There is no guarantee that the spatial patterns that emerge in EOF analysis correspond to dynamical modes of variability. Mindful of this distinction, we have referred to EOFs 1 and 2 of the SLP fields as patterns, rather than modes. However, previous investigations and some diagnostics presented in this thesis offer some insights into the dynamical interpretation of these patterns. The leading SLP PC is closely associated with the variability of the zonally symmetric component of the NH circulation, and derives mainly from the interactions between the eddies and the zonal flow. The second PC, describing the eddy component of the NH flow, owes its prominence relative to other eddy patterns to the structure of the zonally varying climatological-mean flow at the jet stream level. The SLP EOFs for the SH are consistent with this inter-

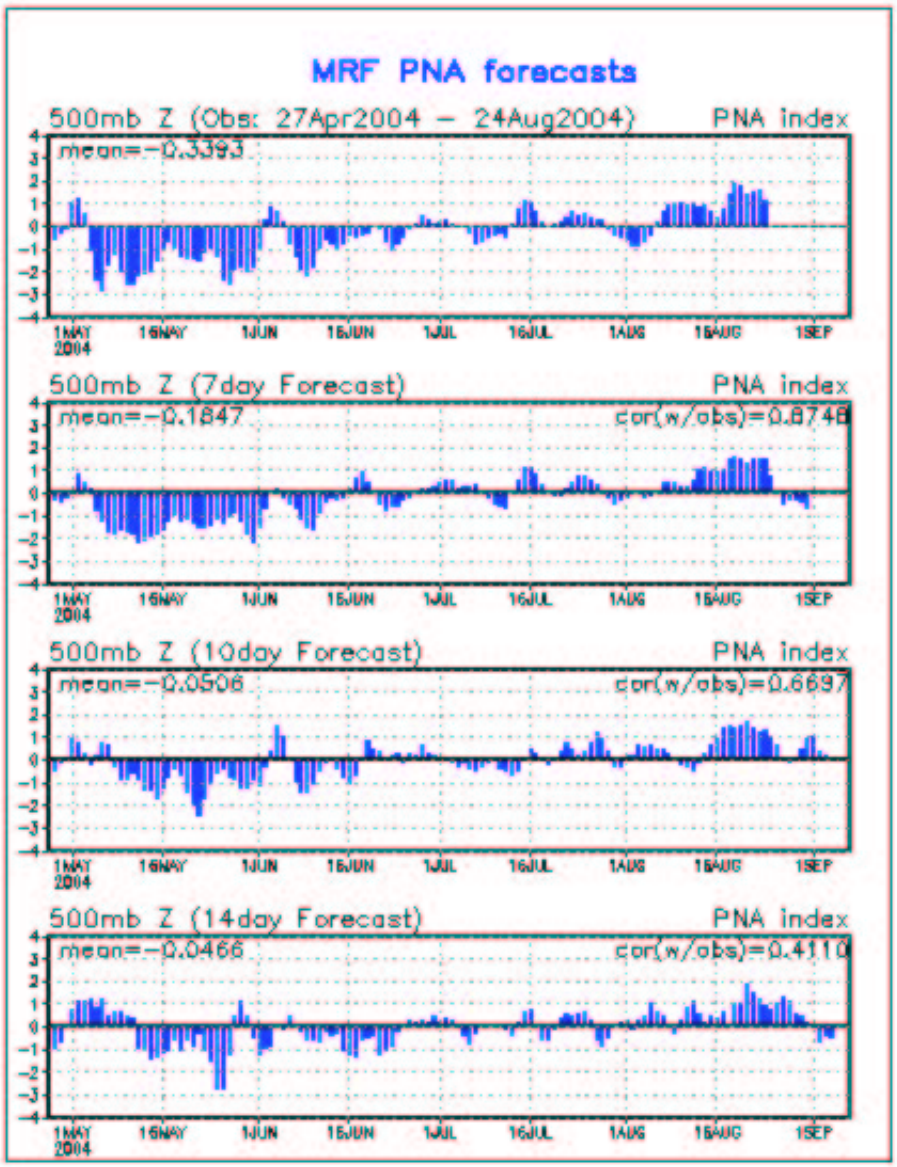

Figure 7.1: Daily time series of observed PNA pattern, and its MRF forecast values 7, 10, 14 days in advance. From the Climate Prediction Center (NOAA) website: *http* : *//www.cpc.ncep.noaa.gov/products/precip/CWlink/ ENSO/verf/ new.teleconnections.shtml*.

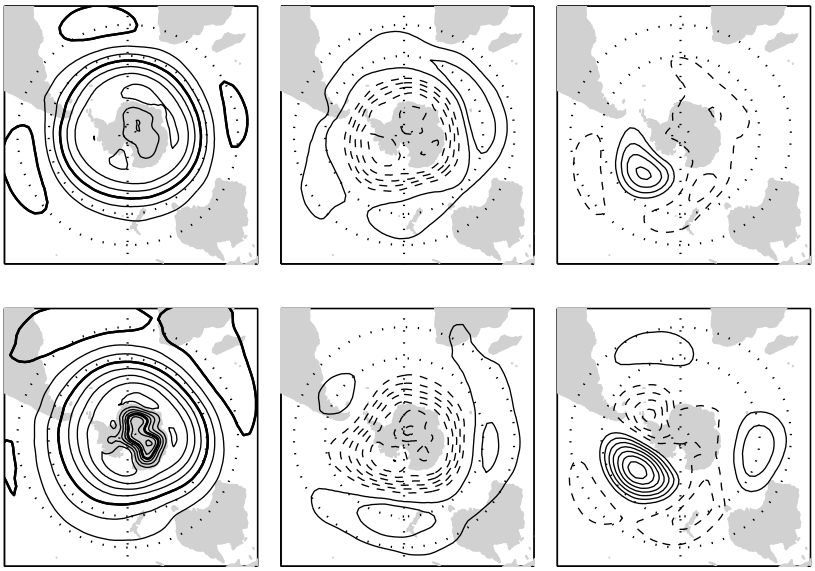

Figure 7.2: 850 hPa geopotential height mean and regression maps upon time series of PC1 and PC2 of the southern hemisphere poleward of 20°S. Upper panels: DJF, lower panels: JJA. Contours: every 60 m, bold 1360, 1540 m (left); every 15 m, negative dashed (center, right).

pretation. During the austral winter (JJA) EOF1, the southern annular mode (SAM) (Gong and Wang, 1999; Thompson and Wallace, 2000) accounts for 30% of the variance on the month-to-month time scale, while EOF2, the "Pacific South American" (PSA) pattern which is in some sense analogous to the NH PNA pattern, accounts for 13%. In contrast, during the austral summer (DJF) when the climatological mean basic state is more zonally symmetric, EOF1 (the SAM) accounts for 35% of the variance and the fraction explained by EOF2 drops to 8%. Mean states end EOF patterns for the two seasons are shown in Fig. 7.2.

The important issues that have yet to be resolved concern not so much the details of the structure of the modes but how best to dynamically interpret the structures and relationships that emerge from the various empirical representations of the data.

7.3 Changes in the basic state of the flow

We have shown that the spatial patterns of extratropical variability are sensitive to the mean background climatological flow. This happens with mean flow changes on a broad frequency range, from the 5-10 day mean time scale (as discussed for example in chapter 5 for the PNA-like wave propagation) to the winter mean time scale (as shown in chapter 6 with the effects of ENSO on the extratropical variability). We have also touched on the issue of changes in climatological flow due to the seasonal cycle, which are certainly as important as the above mentioned changes.

Because of the sensitivity of patterns of variability to the mean flow, it is probably impossible to associate a unique spatial structure with a dynamical phenomenon. In fact, the spatial structures associated with the axes of our two dimensional phase space can be considered as mean signatures of the dynamics of baroclinic wave/mean flow interaction and barotropic instability, respectively, on the mean climatological flow. Therefore, they should be viewed, only in a broad statistical sense, as representative of families of patterns observed under different flow conditions.

An important implication of this result is the need for models to reproduce the climatology very well before being considered to realistically represent the variability of the atmospheric circulation; this aspect is even more significant for studies of climate change, in which the mean background flow is expected to vary in response to external forcing.

In addition, in conditions of climate change, the hypothesis of stationarity in time of empirically estimated relations between atmospheric variables should always be carefully tested.

BIBLIOGRAPHY

Ambaum, M. H. P., B. J. Hoskins, and D. B. Stephenson, 2001: Arctic Oscillation or North Atlantic Oscillation? *J. Climate*, **14,**, 3495–3507.

Baldwin, M., L. J. Gray, T. J. Dunkerton, K. Hamilton, P. H. Haynes, W. J. Randel, J. Holton, M. Alexander, I. Hirota, T. Horinouchi, D. Jones, J. Kinnersley, C. Marquardt, K. Sato, and M. Takahashi, 2001: The quasi-biennial oscillation. *Reviews of Geophysics*, **39**, 179–229.

Barnston, A. G., and R. E. Livezey, 1987: Classification, seasonality, and persistence of the low-frequency atmospheric circulation patterns. *Mon. Wea. Rev.*, **115**, 1083–1126.

Baur, F., P. Hess, and H. Nagel, 1944: Kalender der grosswetterlagen europas 1881-1939. Bad Homburg, 35 pp.

Blackmon, M. L., and N.-C. Lau, 1980: Regional characteristics of the northern hemisphere wintertime circulation: A comparison of the simulation of a GFDL general circulation model with observations. *J. Atmos. Sci.*, **37**, 497–514.

Bretherton, C. S., M. Widmann, V. P. Dymnikov, J. M. Wallace, and I. Bladé, 1999: The effective number of spatial degrees of freedom of a time-varying field. *J. Climate*, **12**, 1990–2009.

Cash, B. A., and S. Lee, 2001: Is the atmospheric zonal index driven by an eddy feedback? *J. Climate*, **14**, 1017–1028.

Chang, E., and Y. Fu, 2002: Inter-decadal variations in Northern Hemisphere winter storm track intensity. *J. Climate*, **15**, 642–658.

Charney, J., and J. G. DeVore, 1979: Multiple flow equilibria in the atmosphere and blocking. *J. Atmos. Sci.*, **36**, 1205–1216.

Chen, W. Y., and H. van den Dool, 1997: Asymmetric impact of tropical SST anomalies on atmospheric internal variability over the North Pacific. *J. Atmos. Sci.*, **54**, 725–740.

Cheng, X., and J. M. Wallace, 1993: Cluster analysis of the northern hemisphere wintertime 500-hPa height field: spatial patterns. *J. Atmos. Sci.*, **50**, 2674–2696.

Cheng, X., N. G., and J. M. Wallace, 1995: Robustness of low-frequency circulation patterns derived from eof and rotated eof analyses. *J. Climate*, **8**, 1709–1720.

Codron, F., 2004: Relation between annular modes and mean state: southern hemisphere summer. *J. Climate*, in press.

Corti, S., F. Molteni, and T. Palmer, 1999: Signature of recent climate change in frequencies of natural atmospheric circulation regimes. *Nature*, **398**, 799–802.

DeWeaver, E., and S. Nigam, 2000: Do stationary waves drive the zonal-mean jet anomalies of the northern winter? *J. Climate*, **13**, 2160–2176.

Exner, F. M., 1913: Uebermonatliche witterungsanomalien auf der nrdlichen erdhaelfte im winter. *Sitz.- Ber. Wiener Akad. Wiss*, **122**, 1165–1241.

Feldstein, S., and S. Lee, 1996: Mechanisms of zonal index variability in an aquaplanet gcm. *J. Atmos. Sci.*, **53**, 3541–3555.

Feldstein, S. B., 2000: The timescale, power spectra, and climate noise properties of teleconnection patterns. *J. Climate*, **13**, 4430–4440.

Feldstein, S., 2002: Fundamental mechanisms of PNA teleconnection pattern growth and decay. *Quart. J. Roy. Meteor. Soc.*, **128,**, 775–796.

Frei, C., and C. Schär, 1998: A precipitation climatology of the alps from high-resolution rain-gauge observations. *Int. J. Climatology*, **18**, 873–900.

Gillet, N. P., and D. W. J. Thompson, 2003: Simulation of recent southern hemisphere climate change. *Science*, **302**, 273–275.

Gillett, N. P., F. W. Zwiers, A. J. Weaver, and P. A. Stott, 2003: Detection of human influence on sea level pressure. *Nature*, **422**, 292–294.

Girs, A., 1974: Large-scale circulation method of long term meteorological forecasts. *Hydrometizdat*, 485p.

Girshick, M. A., 1939: On the sampling theory of the roots of determinantal equations. *Ann. Math. Stat.*, **10**, 203–224.

Gong, D., and S. Wang, 1999: Definition of Antarctic Oscillation index. *Geophys. Res. Letters*, **26**, 459–462.

Gong, D. S. W., and J. Zhu, 2001: East Asian winter monsoon and Arctic Oscillation. *Geophys. Res. Letters*, **28**, 2073–2076.

Hartmann, D. L., and P. Zuercher, 1998: Response of baroclinic lifecycles to barotropic shear. *J. Atmos. Sci.*, **55**, 297–313.

Hoerling, M., J. Hurrell, and T. Xu, 2001: Tropical origins for recent north Atlantic climate change. *Science*, **292**, 90–92.

Honda, M., and H. Nakamura, 2001: Interannual seesaw between the aleutian and icelandic lows. Part I: Seasonal dependence and life cycle. *J. Climate*, **14**, 1029–1042.

Honda, M., H. Nakamura, J. Ukita, I. Kousaka, and K. Takeuchi, 2001: Interannual seesaw between the Aleutian and Icelandic lows. Part II: Its significance in the

interannual variability over the wintertime Northern Hemisphere. *J. Climate*, **14**, 4512–4529.

Horel, J., and J. Wallace, 1981: Planetary-scale atmospheric phenomena associated with the Southern Oscillation. *Mon. Wea. Rev.*, **109**, 813–829.

Horel, J., 1981: A rotated principal component analysis of the interannual variability of the Northern Hemisphere 500 mb height field. *Mon. Wea. Rev.*, **109**, 2080–2092.

Hoskins, B. J., and K. Karoly, 1981: The steady response of a spherical atmosphere to thermal and orographic forcing. *J. Atmos. Sci.*, **38,**, 1179–1196.

Hoskins, B. J., A. Simmons, and D. Andrews, 1977: Energy dispersion in a barotropic atmosphere. *Quart. J. Roy. Meteor. Soc.*, **103,**, 553–567.

Hoskins, B. J., I. N. James, and G. White, 1983: The shape, propagation and mean-flow interaction of large-scale weather systems. *J. Atmos. Sci.*, **40,**, 1595–1612.

Houghton, J., Y. Ding, D. Griggs, M. Noguer, P. van der Linden, X. Dai, K. Maskell, and C. Johnson, 2001: *Climate Change 2001: The Scientific Basis*, Cambridge University Press, 892 pp.

Hurrell, J. W., 1995: Decadal trends in the North Atlantic Oscillation: Regional temperatures and precipitation. *Science*, **269**, 676–679.

Karoly, D. J., 1990: The role of transient eddies in low-frequency zonal variations of the Southern Hemisphere circulation. *Tellus*, **42A**, 41–50.

Kidson, J. W., 1975: Eigenvector analysis of monthly mean surface data. *Mon. Wea. Rev.*, **103**, 177–186.

Kidson, J. W., 1988: Interannual variations in the Southern Hemisphere circulation. *J. Climate*, **1**, 1177–1198.

Kim, K.-Y., 1996: Temporal and spatial subsampling errors for global empirical orthogonal functions: applications to surface temperature field. *J. Geophys. Res.*, **101**, 23433–23446.

Kimoto, M., and M. Ghil, 1993a: Multiple flow regimes in the northern hemisphere winter. part I: methodology and hemispheric regimes. *J. Atmos. Sci.*, **50**, 2625–2643.

Kimoto, M., and M. Ghil, 1993b: Multiple flow regimes in the northern hemisphere winter. part II: sectorial regimes and preferred transitions. *J. Atmos. Sci.*, **50**, 2645–2673.

Koide, H., and K. Kodera, 1999: A SVD analysis between the winter NH 500-hPa height and surface temperature fields. *J. Meteorol. Soc. Japan*, **77**, 47–61.

Kumar, A., and M. P. Hoerling, 1998: Annual cycle of Pacific-North American seasonal predictability associated with ENSO. *J. Climate*, **11**, 3295–3308.

Kumar, A., A. G. Barnston, P. Peng, M. P. Hoerling, and L. Goddard, 2000: Changes in the spread of the variability of the seasonal mean atmospheric states associated with ENSO. *J. Climate*, **13**, 3139–3151.

Kushnir, Y., and J. M. Wallace, 1989: Low-frequency variability in the Northern Hemisphere winter: geographical distribution, structure and time-scale dependence. *J. Atmos. Sci.*, **46**, 3122–3142.

Kutzbach, J., 1970: Large-scale features of monthly mean Northern Hemisphere anomaly maps of sea-level pressure. *Mon. Wea. Rev.*, **98**, 708–716.

Labitzke, K., and Collaborators, 2002: The Berlin stratospheric data series. *Meteorological Institute*, free University Berlin, Germany.

Lee, S., and S. Feldstein, 1996: Mechanism of zonal index evolution in a two-layer model. *J. Atmos. Sci.*, **53**, 2232–2246.

Limpasuvan, V., and D. L. Hartmann, 2000: Wave-maintained annular modes of climate variability. *J. Climate*, **13**, 4414–4429.

Lorenz, D. J., and D. L. Hartmann, 2001: Eddy-zonal flow feedback in the Southern Hemisphere. *J. Atmos. Sci.*, **58**, 3312–3327.

Lorenz, D. J., and D. L. Hartmann, 2003: Eddy-zonal flow feedback in the Northern Hemisphere winter. *J. Climate*, **16**, 1212–1227.

Lorenz, E., 1951: Seasonal and irregular varirations of the northern hemisphere sea-level pressure profile. *J. Meteorol.*, **8**, 52–59.

Lorenz, E., 1963: Deterministic nonperiodic flow. *J. Atmos. Sci.*, **20**, 130–141.

Mantua, N., S. Hare, Y. Zhang, J. Wallace, and R. C. Francis, 1997: A Pacific interdecadal climate oscillation with impacts on salmon production. *Bull. Am. Meteorol. Soc.*, **78**, 1069–1079.

Mo, K., and M. Ghil, 1988: Cluster analysis of multiple planetary flow regimes. *J. Geophys. Res.*, **93**, 10927–10952.

Molteni, F. Tibaldi, S., and T. Palmer, 1990: Regimes in the wintertime circulation over Northern extratropics. I: Observational evidence. *Quart. J. Roy. Meteor. Soc.*, **116**, 31–67.

Molteni, F., A. Sutera, and N. Tronci, 1988: the eof's of the geopotential eddies at 500 mb in winter and their probability density distribution. *J. Atmos. Sci.*, **45**, 3063–3080.

Molteni, F., L. Ferranti, T. Palmer, and P. Viterbo, 1993: A dynamical interpretation of the global response to Equatorial Pacific SST anomalies. *J. Climate*, **6**, 777–795.

Monahan, A.H. Pandolfo, L., and J. Fyfe, 2001: The preferred structure of variability of the Northern Hemisphere atmospheric circulation. *Geophys. Res. Letters*, **28**, 1019–1022.

Monahan, A., J. C. Fyfe, and G. Flato, 2000: A regime view of Northern Hemisphere atmospheric variability and change under global warming. *J. Geophys. Res.*, **27**, 1139–1142.

Monahan, 2000: Nonlinear principal component analysis by neural networks: theory and application to the Lorenz system. *J. Climate*, **13**, 821–835.

Namias, J., 1950: The index cycle and its role in the general circulation. *J. Meteor.*, **7**, 130–139.

Newman, M., and P. Sardeshmukh, 1998: The impact of the annual cycle on the north-pacific/north american response to remote low-frequency forcing. *J. Atmos. Sci.*, **55**, 1336–1353.

Nitta, T., and S. Yamada, 1989: Recent warming of tropical sea surface temperature and its relationship to the Northern Hemisphere circulation. *J. Meteor. Soc. Japan*, **67,**, 375–383.

North, G. R., T. L. Bell, R. F. Cahalan, and F. J. Moeng, 1982: Sampling errors in the estimation of empirical orthogonal functions. *Mon. Wea. Rev.*, **110**, 699–706.

Palmer, T. N., 1999: A nonlinear dynamical perspective on climate prediction. *J. Climate*, **12**, 575–591.

Quadrelli, R., and J. M. Wallace, 2002: Dependence of the structure of the Northern Hemisphere annular mode on the polarity of ENSO. *Geophys. Res. Letters*, **29**, 2132–2135.

Quadrelli, R., and J. M. Wallace, 2004a: A simplified linear framework for interpreting patterns of Northern Hemisphere wintertime climate variability. *J. Climate*, **17**, in press.

Quadrelli, R., and J. M. Wallace, 2004b: Varied expressions of the hemispheric circulation observed in association with contrasting polarities of prescribed patterns of variability. *J. Climate*, **17**, in press.

Quadrelli, R., J. Wallace, and C. Bretherton, 2004: On mixing errors in empirical orthogonal functions. *J. Climate*, submitted.

Renwick, J. A., and J. M. Wallace, 1995: Predictable anomaly patterns and the forecast skill of the northern hemisphere wintertime 500-mb height field. *Mon. Wea. Rev.*, **123**, 2114–2131.

Renwick, J. A., and J. M. Wallace, 1996: Relationships between North Pacific wintertime blocking, El Niño, and the PNA pattern. *Mon. Wea. Rev.*, **124**, 2071–2076.

Rex, D., 1951: The effect of Atlantic blocking action upon European climate. *Tellus*, **3**, 100–111.

Robertson, A., and M. Ghil, 1999: Large-scale weather regimes and local climate over the western united states. *J. Climate*, **12**, 1796–1813.

Robinson, W. A., 1991: The dynamics of the zonal index in a simple model of the atmosphere. *Tellus*, **43A**, 295–305.

Rossby, C. G., and H. C. Willett, 1948: The circulation of the upper troposphere and lower stratosphere. *Science*, **108**, 643–652.

Rossby, C. G., 1939: Relations between variations in the intensity of the zonal circulation of the atmosphere and the displacements of the semipermanent centers of action. *J. Mar. Res.*, **3**, 38–55.

Sardeshmukh, P., M. Newman, and M. D. Borges, 1997: Free barotropic rossby wave dynamics of the wintertime low-frequency flow. *J. Atmos. Sci.*, **54**, 5–23.

Sardeshmukh, P., G. P. Compo, and C. Penland, 2000: Changes of probability associated with El Niño. *J. Climate*, **13**, 4268–4286.

Sassi, F., R. Garcia, B. Boville, and H. Liu, 2002: On temperature inversions and the mesospheric surf zone. *J. Geophys. Res.*, **107(D19)**, 4380.

Schubert, S., M. J. Suarez, and Y. Chang, 2001: the impact of ENSO on extratropical low-frequency noise in seasonal forecast. *J. Climate*, **14**, 2351–2365.

Simmons, A. J., J. M. Wallace, and G. Branstator, 1983: Barotropic wave propagation and instability, and atmospheric teleconnection patterns. *J. Atmos. Sci.*, **40**, 1363–1392.

Smith, C., and P. Sardeshmukh, 2000: The effect of ENSO on the intraseasonal variance of surface temperatures in winter. *ijc*, **20**, 1543–1557.

Storch, H. v., and Hannoschöck, 1985: Statistical aspects of estimated principal vectors (EOFs) based on small sample sizes. *J. Clim. Appl. Meteorol.*, **24**, 716–724.

Sutera, A., 1986: Probability density distribution of large-scale atmospheric flow. *Adv. Geophys.*, **29**, 319–338.

Thompson, D. W. J., and D. Lorenz, 2004: The signature of the annular modes in the tropical troposphere. *J. Climate*, in press.

Thompson, D. W. J., and J. M. Wallace, 1998: The Arctic Oscillation signature in the wintertime geopotential height and temperature fields. *Geophys. Res. Letters*, **25**, 1297–1300.

Thompson, D. W. J., and J. M. Wallace, 2000: Annular modes in the extratropical circulation. part I: month-to-month variability. *J. Climate*, **13**, 1000–1016.

Thompson, D. W. J., and J. M. Wallace, 2001: Regional climate impacts of the northern hemisphere annular mode. *Science*, **293**, 85–89.

Thompson, D., J. M. Wallace, and G. Hegerl, 2000: Annular modes in the extratropical circulation. part II: Trends. *J. Climate*, **13**, 1000–1016.

Thompson, D. W. J., M. Baldwin, and J. M. Wallace, 2002a: Stratospheric connection to Northern hemisphere wintertime weather: implications for prediction. *J. Climate*, **15**, 1421–1428.

Thompson, D., M. Baldwin, and J. Wallace, 2002b: Stratospheric connection to northern hemisphere wintertime weather: Implications for prediction. *J. Climate*, **15**, 1421–1428.

Trenberth, K. E., and J. Hurrell, 1994: Decadal atmosphere-ocean variations in the Pacific. *Climate Dyn.*, **9**, 303–319.

Trenberth, K. E., and D. Paolino, 1980: The Northern Hemisphere sea-level pressure data set: trends, errors and discontinuities. *Mon. Wea. Rev.*, **108**, 855–872.

Trenberth, K. E., and D. Paolino, 1981: Characteristics patterns of variability of sea level pressure in the Northern Hemisphere. *Mon. Wea. Rev.*, **109**, 1169–1189.

Trenberth, K. E., and D. J. Shea, 1987: On the evolution of the southern oscillation. *Mon. Wea. Rev.*, **115**, 3078–3096.

Trenberth, K. E., 1984: Signal versus noise in the Southern Oscillation. *Mon. Wea. Rev.*, **112**, 326–332.

Trigo, R. M., T. J. Osborn, and J. M. Corte-Real, 2002: The North Atlantic Oscillation influence on Europe: climate impacts and associated physical mechanisms. *Clim. Res.*, **20**, 9–17.

van den Dool, H., S. Saha, and A. Johansson, 2000: Empirical orthogonal teleconnections. *J. Climate*, **13**, 1421–1435.

van Loon, H., and J. Rogers, 1978: The seesaw in winter temperatures between greenland and northern europe. part I: General description. *Mon. Wea. Rev.*, **106**, 296–310.

Vangengeim, G., 1952: The basics of the large-scale circulation method of long term meteorological forecasts for the Arctic. *AANII*, **34**, 314p.

Vautard, R., and B. Legras, 1988: On the source of midlatituide low-frequency variability. part II: nonlinear equlibration of weather regimes. *J. Atmos. Sci.*, **45**, 2845–2867.

Vautard, R., 1990: Multiple weather regimes over the north atlantic: analysis of precursors and successors. *Mon. Wea. Rev.*, **118**, 2056–2081.

Walker, G. T., and E. W. Bliss, 1932: World Weather V. *Mem. Roy. Meteor. Soc.*, **4**, 53–84.

Wallace, J., and M. Blackmon, 1983: Observations of low-frequency atmospheric variability. *Large-scale dynamical processes in the atmosphere*, 55–109, edited by B.J. Hoskins and R.P. Pearce.

Wallace, J. M., and D. S. Gutzler, 1981: Teleconnections in the geopotential height field during the northern hemisphere winter. *Mon. Wea. Rev.*, **109**, 784–812.

Wallace, J. M., and D. W. J. Thompson, 2002: The Pacific center of action of the Northern Hemisphere annular mode: Real or artifact? *J. Climate*, **15**, 1987–1991.

Wallace, J. M., R. L. Panetta, and J. Estberg, 1993: Representation of the equatorial quasi-biennial oscillation in EOF phase-space. *J. Atmos. Sci.*, **50,**, 1751–1762.

Wallace, J. M., Y. Zhang, and J. Renwick, 1995: Dynamic contribution to hemispheric mean temperature trends. *Science*, **270**, 780–783.

Walsh, J., W. Chapman, and T. Shy, 1996: Recent decrease of sea level pressure in the central arctic. *J. Climate*, **9**, 480–486.

Wilkinson, J., 1965: *The algebraic eigenvalue problem*, Oxford University Press, 266 pp.

Willett, H., 1948: Patterns of world weather changes. *Trans. Amer. Geophys. Union*, **29**, 803–809.

Willmott, C. J., and S. M. Robeson, 1995: Climatologically Aided Interpolation (CAI) of terrestrial air temperature. *Int. J. Climatology*, **15**, 221–229.

Winkler, C. R., M. Newman, and P. Sardeshmukh, 2001: A linear model of wintertime low-frequency variability. part I: Formulation and forecast skill. *J. Climate*, **14**, 4474–4494.

Woodruff, S. D., 2000: COADS updates including newly digitized data and the blend with the UK Meteorological Office Marine Data Bank and Quality control in recent COADS updates. *Proceedings of workshop on Preparation, Processing and Use of Historical Marine Meteorological Data*, Tokyo, Japan, 28-29 November 2000, Japan Meteorological Agency and the Ship & Ocean Foundation, 9-13 and 49-53.

Wu, Q., and D. M. Straus, 2003: Multiple planetary flow regimes and the eddy forcing in northern hemisphere wintertime variability. *Geophys. Res. Letters*, **30**, 1861–1864.

Zhang, Y., J. M. Wallace, and D. S. Battisti, 1997: ENSO-like interdecadal variability: 1900-93. *J. Climate*, **10**, 1004–1020.

Appendix A

SAMPLING ERRORS IN EMPIRICAL ORTHOGONAL FUNCTIONS

A.1 Introduction

In this appendix we show that the leading EOFs of the sea-level pressure field are more clearly defined than their counterparts in the 500-hPa height field.

The specific issue that we are concerned with is the size of the "sampling errors" associated with EOFs of a finite dataset. It is in fact known that the EOFs for a finite sample are only estimates of the "true" eigenvectors that would be perfectly recovered from an infinite size dataset.

North et al. (1982) derived an explicit form for the first order errors in the eigenvalues λ_i of the covariance matrix for a sample of T independent realizations in time. The resulting formula

$$\delta\lambda_i \approx 2^{1/2}\epsilon\lambda_i, \tag{A.1}$$

where $\epsilon = T^{-1/2}$, has been extensively used to estimate the sampling variability. Eigenvalues with overlapping errors can be regarded as "effective multiplets"; one should avoid truncating an EOF decomposition within such a range. North et al. (1982) do not provide an explicit estimate for the error associated with eigenvectors; their formula (23) also relies on a hypothetical form of the sample covariance matrix. quite large, even satisfied.

Several other papers have dealt with the sampling variability issue. The statistical properties of estimated eigenvalues and eigenvectors for small samples have been studied (Storch and Hannoschöck, 1985), and bounds for sampling variability errors

have been proposed (Kim, 1996). Early in the statistical literature, Girshick (1939) derived the form of asymptotic errors in eigenvectors, but to our knowledge an explicit form for sampling errors associated with eigenvectors has never been given in the geoscience literature, or applied to a geophysical problem.

It is important for a number of geophysical applications to be able to quantify uncertainties not only in the eigenvalues, but also in the eigenvectors.

Examples include assessing whether a pattern that resembles the leading EOF should be interpreted as a realization of that EOF or as a distinctly different pattern and determining whether the leading EOFs derived from two different datasets (either observations or model output) are distinctly different from one another.

To quantify the uncertainties in EOFs estimated from a finite data sample, we propose a general formula which complements the formula for the degree of separation between eigenvalues given in North et al. (1982), and enables a more thorough analysis on eigenvector errors.

This appendix is comprised of five parts. In the next section we derive an analytical expression for the errors (to first order for eigenvectors and second order for eigenvalues) in sample EOF estimates. In section A.3 mixing errors in the leading EOF are analyzed for a hypothetical dataset with a prescribed eigenvalue spectrum. In section A.4 the results are applied to the observed Northern Hemisphere geopotential height field. Sampling errors for the leading EOF at several height levels are compared, and it is deduced that mode mixing is smaller at the earth's surface than in the mid-troposphere. Conclusions are given in section A.5.

A.2 Eigenvalue and eigenvector sampling errors

The magnitude of the sampling error associated with a single eigenvector depends on how much it tends to mix with each of the other eigenvectors of the sample. A simple illustration of this problem is presented by the schematic in Fig. A.1. Any

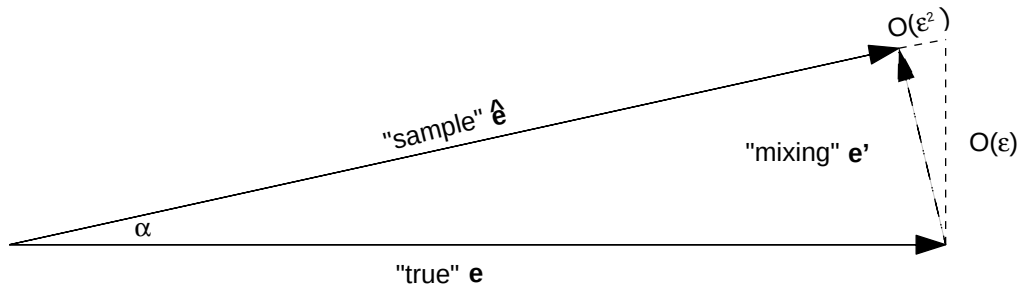

Figure A.1: Schematic of the mixing error associated with an eigenvector for a finite-size dataset, compared with its corresponding infinite size data eigenvector. To first order, the error is orthogonal to the true eigenvector.

eigenvector $\hat{\mathbf{e}}$ of a finite size dataset is generally located at an angle α from the direction of the "true" corresponding eigenvector $\mathbf{e}$, and the sampling error $\mathbf{e}'$ can be expressed as a linear combination of all the other "true" eigenvectors $\mathbf{e_i}$. In this paper we will find that if the eigenvalues are well separated the typical size of α will be $O(\epsilon)$, and, to first order in ϵ, $\mathbf{e}'$ is orthogonal to $\mathbf{e}$.

We consider the case of a dataset with T independent realizations in time over N grid points, where the grid spacing is dense enough that spatial sampling errors are not important. In general the number of resulting EOFs is $N^* = \min(T-1, N)$.

The mathematical formulation of the sampling problem is based on Appendix A of Bretherton et al. (1999), part b. Here we follow their approach of working in the basis of the "true" eigenvectors, which are obtained from the "true" covariance matrix $\mathbf{C}$. If $\mathbf{E}$ is the orthogonal matrix whose columns are the normalized eigenvectors, and $\mathbf{\Lambda}$ is the diagonal matrix of the eigenvalues λ_i, then

$$\mathbf{\Lambda} = \mathbf{E^T C E}. \tag{A.2}$$

With only T independent realizations in time none of the elements of Λ, $\mathbf{E}$ and $\mathbf{C}$ are known precisely. The corresponding variables obtained directly from the finite data sample will be denoted by $\hat{}$.

Applying the transformation of (A.2) to $\hat{\mathbf{C}}$ (instead of $\mathbf{C}$) we obtain a new matrix, $\hat{\mathbf{L}}$:

$$\hat{\mathbf{L}} = \mathbf{E^T}\hat{\mathbf{C}}\mathbf{E}.$$

The eigenvectors of $\hat{\mathbf{L}}$ correspond to the eigenvectors of $\hat{\mathbf{C}}$ but they are expressed in the basis of the "true" eigenvectors $\mathbf{e_i}$. In fact the eigenvalue equations for $\hat{\mathbf{L}}$ and $\hat{\mathbf{C}}$ are related by the fact that if

$$\hat{\mathbf{L}}\hat{\mathbf{e}} = \hat{\lambda}\hat{\mathbf{e}}, \tag{A.3}$$

then $\hat{\mathbf{C}}\hat{\mathbf{y}} = \hat{\lambda}\hat{\mathbf{y}}$, with $\hat{\mathbf{y}} = \mathbf{E}\hat{\mathbf{e}}$, and $||\hat{\mathbf{y}}_\mathbf{i} - \hat{\mathbf{y}}_\mathbf{j}|| = ||\hat{\mathbf{e}}_\mathbf{i} - \hat{\mathbf{e}}_\mathbf{j}||$ from the properties of the orthogonal matrix $\mathbf{E}$.

Therefore the sampling problem for the eigenvectors of $\hat{\mathbf{C}}$ can be solved working in the basis of the $\mathbf{e_i}$, and defining the errors as departures of the eigenvectors $\hat{\mathbf{e}}_\mathbf{i}$ of $\hat{\mathbf{L}}$ from the corresponding "true" eigenvectors $\mathbf{e_i}$. Since $\hat{\mathbf{L}}$ is symmetric and positive definite, it has real, orthonormal eigenvectors. It can be interpreted as a perturbed form $\hat{\mathbf{L}} = (\mathbf{\Lambda}+\epsilon\mathbf{P})$ of the diagonal matrix $\mathbf{\Lambda}$. Bretherton et al. (1999) showed that for a large number of independent samples (T), the elements of $\mathbf{P}$ can be expressed in terms of T, the "true" eigenvalues λ_i, and uncorrelated unit normal random perturbations (w_{ij}):

$$P_{ij} = \begin{cases} 2^{1/2}\lambda_i w_{ii} & j = i \\ \lambda_i^{1/2}\lambda_j^{1/2} w_{ij} & j \neq i \end{cases} \tag{A.4}$$

where

$$\epsilon = T^{-1/2} \ll 1. \tag{A.5}$$

For an infinite sample length $\hat{\mathbf{L}} \rightarrow \mathbf{\Lambda}$ (and no mode mixing occurs).

The eigenvalues $\hat{\lambda}_i$ and eigenvectors $\hat{\mathbf{e}}_\mathbf{i}$ of (A.3) can be expressed as perturbation series:

$$\hat{\lambda}_i = \lambda_i + k_{i1}\epsilon + k_{i2}\epsilon^2 ... \tag{A.6}$$

$$\hat{\mathbf{e}}_\mathbf{i} = \mathbf{e_i} + \epsilon\hat{\mathbf{e}}_\mathbf{i1} + \epsilon^2\hat{\mathbf{e}}_\mathbf{i2} ... \tag{A.7}$$

The solution of this perturbation problem (i.e. the terms k_{ij} and $\hat{\mathbf{e}}_{\mathbf{ij}}$) can be found in the statistics literature. Wilkinson (1965) showed that the first order perturbation to the i'th eigenvector is a sum of independent perturbations deriving from the mixing occurring between that eigenvector and each of the other $N-1$ eigenvectors:

$$\hat{\mathbf{e}}_{\mathbf{i1}} = \sum_{j \neq i} \frac{P_{ij}\mathbf{e_j}}{(\lambda_i - \lambda_j)}. \tag{A.8}$$

Recalling the expression (A.4) for P_{ij}, this implies that the perturbed eigenvectors have the form

$$\hat{\mathbf{e}}_{\mathbf{i}} = \mathbf{e_i} + \sum_{j \neq i} \alpha_{ij}\mathbf{e_j} + O(\epsilon^2) \tag{A.9}$$

where

$$\alpha_{ij} = \alpha^*_{ij} w_{ij} \tag{A.10}$$

$$\alpha^*_{ij} = \epsilon \frac{\beta_{ij}^{1/2}}{(1-\beta_{ij})} \tag{A.11}$$

$$\beta_{ij} = \frac{\lambda_j}{\lambda_i}. \tag{A.12}$$

The absolute value of α^*_{ij} corresponds to the standard deviation of α_{ij} because the w_{ij} are unit random perturbations. Note that the perturbation theory is valid only if $|\alpha^*_{ij}| \ll 1$.

Wilkinson also showed that, to second order in ϵ,

$$\hat{\lambda}_i = \lambda_i(1 + \sqrt{2}\epsilon w_{ii}) + \epsilon^2 \sum_{j \neq i} \frac{\lambda_j}{(1-\beta_{ij})} w_{ij}^2. \tag{A.13}$$

To first order (A.13) is consistent with the criterion of North et al. (1982) referred to here in (A.1). In that same paper it is noted that the first order perturbation for a given *eigenvalue* is independent of its spacing with respect to other eigenvalues. In contrast, it is clear from (A.11) that the first order *eigenvector* perturbation is strongly dependent on the ratio of the mixing eigenvalues.

Also, while the first order shift of the eigenvalues has random sign, the second order bias is positive or negative depending on the relative ranking of the two eigenvalues

that mix. Consistent with previous observations of Storch and Hannoschöck (1985), the largest eigenvalues tend to be overestimated and the smallest ones underestimated.

The two key factors that determine the typical mixing between pairs of eigenvectors i, j are thus:

- the ratio β_{ij} between the corresponding eigenvalues (the closer the ratio to 1, the larger the error) ($\hat{\lambda}_i$) are can error
- the number T of independent realizations in time.

For geophysical data the number of independent realizations in time T is generally smaller than the actual sample size, because of serial time dependence. Therefore, an estimate of the effective number of degrees of freedom T^* should be computed from the sample (as done in the example of section A.4) .

Figure A.2 shows the dependence of the individual error contribution α^*_{ij} (representing mixing of eigenvectors i and j only) upon the eigenvalue ratio $\beta_{ij} = \lambda_j/\lambda_i$ and the sample size T. Within the range represented (for small values of α_{ij}), the perturbation theory is valid, and $\arctan(\alpha_{ij}) \approx \alpha_{ij}$; thus, α_{ij} represents the angular error in the plane i, j, and α^*_{ij} is its standard deviation. Only ratios β_{ij} smaller than 1 (i.e. mixing with eigenvectors of lower order) are plotted, since the absolute value of α^*_{ij} is the same for a ratio β_{ij} and for its reciprocal. This is because the mixing between eigenvectors i and j contributes equally to errors in $\hat{\mathbf{e}}_\mathbf{i}$ (for which $\beta_{ij} = \lambda_j/\lambda_i$) and $\hat{\mathbf{e}}_\mathbf{j}$.

The total error is a sum of contributions from each direction; an estimate of the overall accuracy in the computation of an eigenvector $\mathbf{e_i}$ is the expected spatial correlation coefficient between a random sample realization $\hat{\mathbf{e}}_\mathbf{i}$ and $\mathbf{e_i}$: r= E[$\hat{\mathbf{e}}_\mathbf{i} \cdot \mathbf{e_i}$], where E denotes an expected value. Note that $\hat{\mathbf{e}}_\mathbf{i}$ is given by (A.9) to $O(\epsilon)$, but for this calculation must be normalized back to a unit vector (an $O(\epsilon^2)$ correction). Hence,

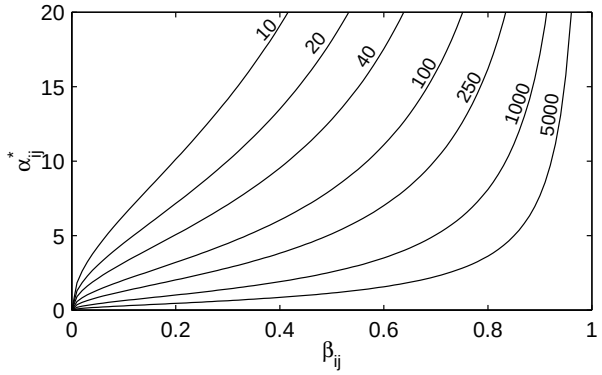

Figure A.2: Standard deviation of the angular error α_{ij} (in *degrees*) due to mixing between eigenvectors i and j, vs. ratio $\beta_{ij} = \lambda_j/\lambda_i$, as in (A.11), for 10, 20, 40, 100, 250, 1000, and 5000 independent realizations in time (T), as indicated.

to first order,

$$r = E\left[\left(\frac{\mathbf{e_i} + \sum_{j\neq i}\alpha_{ij}\mathbf{e_j}}{[1+\sum_{j\neq i}\alpha_{ij}^2]^{1/2}}\right)\cdot\mathbf{e_i}\right] \tag{A.14}$$

$$= E\left[\frac{1}{[1+\sum_{j\neq i}\alpha_{ij}^2]^{1/2}}\right] \tag{A.15}$$

$$= E\left[1 - 0.5\sum_{j\neq i}\alpha_{ij}^2\right] \tag{A.16}$$

$$= 1 - 0.5\sum_{j\neq i}\alpha_{ij}^{*2}. \tag{A.17}$$

The third step above follows since the α^*_{ij} are assumed small for large T, else the perturbation theory is not accurate. The last step follows since $E(\alpha^2_{ij}) = \alpha^*_{ij}$.

We now show that if the North eigenvalue separation criterion is satisfied for the leading eigenvalue λ_1, then the sample EOF1 is expected to be well correlated with the true EOF1. For the leading eigenvector, the North et al. (1982) separation criterion is satisfied when

$$\lambda_1 - \lambda_2 \geq \delta\lambda_1 + \delta\lambda_2 \approx (\lambda_1 + \lambda_2)\sqrt{2}\epsilon, \tag{A.18}$$

or, since $\epsilon \ll 1$,

$$\beta_{12} = \frac{\lambda_2}{\lambda_1} < \beta_c = 1 - 2\sqrt{2}\epsilon. \tag{A.19}$$

If the remaining eigenvalues are well separated from λ_1, they will contribute only $O(\epsilon^2)$ to the correlation r. Neglecting these contributions to (A.17),

$$\begin{aligned} r &= 1 - 0.5\alpha_{12}^{*2} && \text{(A.20)} \\ &= 1 - 0.5\epsilon^2 \frac{\beta_{12}}{(1-\beta_{12})^2} && \text{(A.21)} \\ &> 1 - 0.5\epsilon^2 \frac{\beta_c}{(1-\beta_c)^2} = 1 - \frac{1}{16} + \frac{\sqrt{2}}{8}\epsilon = 0.9375. && \text{(A.22)} \end{aligned}$$

The formula given in (A.22) can be trivially generalized to eigenvectors of any order. Also, from (A.17) it is clear that EOFs of higher order than 1 tend to be subject to greater uncertainty than the leading EOF, even if their eigenvalues are just as well separated from their nearest neighbors as λ_1 is separated from λ_2. This is because of the cumulative effects of mixing with other nearby EOFs of both higher and lower order.

A.3 Mixing error in the leading EOF: an example

In this section we estimate the sample size needed in order to obtain acceptably small errors in the computation of the leading EOF. We consider a hypothetical multivariate random process whose true covariance matrix has N eigenvalues, chosen as follows. It is assumed that $\beta_{12} = \lambda_2/\lambda_1$ can take any possible value $0 < \beta_{12} < 1$, that the eigenvalues from the third onward decrease exponentially with a constant ratio $\beta = \lambda_{j+1}/\lambda_j$, and that the N eigenvalues sum to 1. This uniquely defines all the eigenvalues:

$$\begin{cases} \lambda_1 = (1 + \beta_{12}\frac{1-\beta^{N-1}}{1-\beta})^{-1} \\ \lambda_2 = \beta_{12}\lambda_1 \\ \lambda_n = \beta^{n-2}\lambda_2, \qquad\qquad 3 \le n < N. \end{cases} \tag{A.23}$$

This eigenvalue spectrum idealizes the real examples to be shown in section A.4.

The sample size (T) needed to obtain a desired expected correlation coefficient for the sample EOF1 and the true EOF1 can be estimated from (A.17) for any combination of λ_1 and β_{12}. In Fig. A.3, results are shown for a hypothetical dataset with $N = 100$ eigenvalues and a threshold correlation coefficient of 0.975. The boundaries of the region reflect the fact that, for a given λ_1, the possible range of β_{12} is constrained by the definition of the model.[1]

For sufficiently large values of λ_1 (i.e. ≥ 0.6), for which λ_1 is necessarily well separated from all other eigenvalues, mixing errors are small even for relatively small samples ($T \leq 100$). However, very large samples ($T > 500$) are needed to accurately estimate the first EOF when λ_2 is more than 80% of λ_1 ($\beta_{12} > 0.8$). In this case, β_{12} largely controls the necessary sample size T, except for very small values of λ_1.

A.4 Sampling errors in geopotential height EOFs

Here we will use the results of section A.2 to estimate the size of the sampling errors in the leading EOF of the Northern Hemisphere winter geopotential height field, at various levels. In analogy with the SLP, at each of the other levels shown principal component analysis (PCA) is performed on the covariance matrix of monthly DJFM anomalies, for the period of record 1958-1999. The anomalies are area-weighted by the square root of the cosine of latitude, and only the region north of 20°N is included in the analysis.

The sample size T is 168 months but an effective sample size T^* for each level is computed by correcting T for the area weighted lag-1 autocorrelation $\langle r \rangle$, according to the second order formula given in Bretherton et al. (1999):

$$T^* = T\frac{(1 - \langle r \rangle^2)}{(1 + \langle r \rangle^2)}, \tag{A.24}$$

[1]For a given λ_1, the lowest possible β_{12} occurs when $\beta = 1$. Then, from (A.23), $\beta_{12} = \frac{1-\lambda_1}{\lambda_1(N-1)}$. Also, from $\lambda_1 + \lambda_2 \leq 1$ and $\lambda_2 \leq \lambda_1$ follows that the upper limit for β_{12} is $\min(1, \frac{1-\lambda_1}{\lambda_1})$.

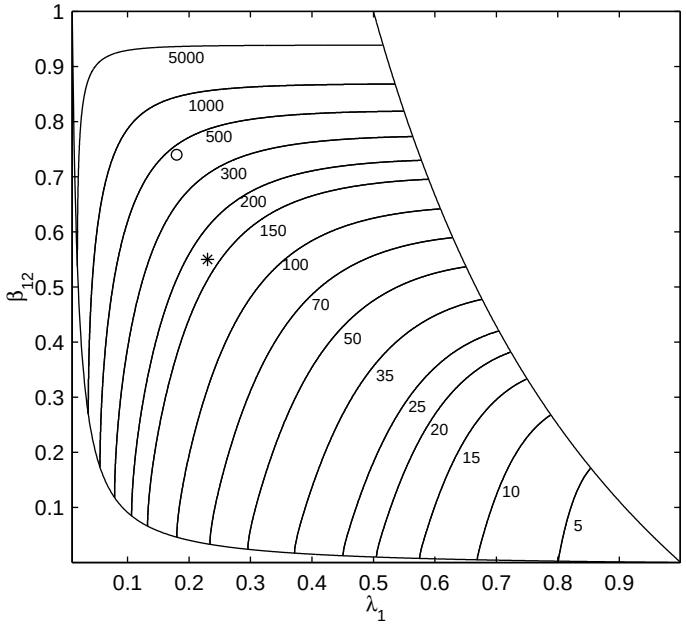

Figure A.3: Number of independent realization in time (T) needed to expect a correlation coefficient of .975 between estimated and "true" leading EOF as a function of the values of λ_1 and $\beta_{12} = \lambda_2/\lambda_1$. Total number of eigenvalues: $N = 100$. The symbols (star, circle) indicate values of λ_1 and β_{12} corresponding to observations of SLP and 500 hPa, respectively (see next section). See text for further explanation.

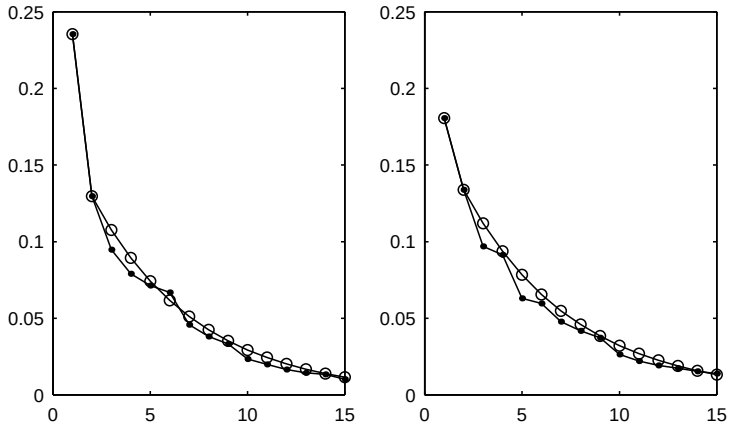

Figure A.4: Spectra of the eigenvalues normalized to a unit sum for SLP (left) and 500 hPa geopotential height (right) monthly mean fields (full circles), compared to a synthetic dataset with same values of λ_1 and λ_2, and constant ratio β between eigenvalues of higher order (empty circles). See text for further explanation.

with typical values of $\langle r \rangle^2$ of ≈ 0.06 ($T^* \approx 150, \epsilon = (T^*)^{-1/2} \approx 0.08$) in the troposphere and ≈ 0.2 ($T^* \approx 110, \epsilon \approx 0.1$) in the stratosphere.

Fig. A.4 shows the observed eigen-spectra of monthly mean SLP and 500 hPa geopotential height; in addition, it shows idealized fits to these spectra of the type analyzed in section A.3. These fits are quite reasonable, showing that the idealized spectrum provides representative estimates of the sampling errors in the leading EOFs of our real datasets.

The first SLP EOF has been defined as the northern annular mode (Thompson and Wallace, 1998), while the second is closely associated with the Pacific North American pattern (Wallace and Thompson, 2002; Quadrelli and Wallace, 2004a). These two modes are well separated from one another and from the third mode according to the criterion of North et al. (1982). At other tropospheric levels (e.g. 500 hPa, see Fig. A.4) the two leading eigenvalues the two SLP modes, are generally less separated from one another than the leading SLP EOFs are.

Figure A.5 shows expected mode-mixing estimated from (A.11) for our specific

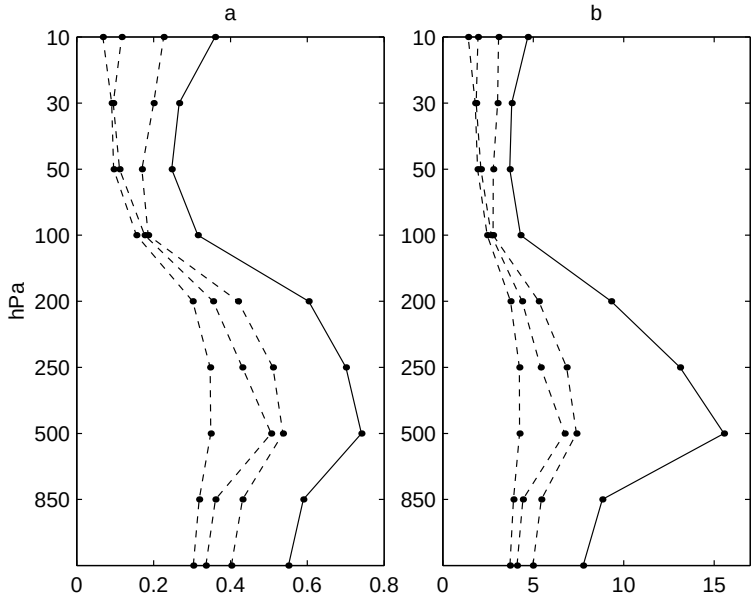

Figure A.5: Vertical profile of mixing errors in the leading EOF ($i = 1$): a) ratio $\beta = \lambda_j/\lambda_1$ for $j = 2$ (solid), $3 - 5$ (dashed), and b) angle α^*_{1j} ($degrees$) between the sample and "true" EOF in the plane defined by the first and the j^{th} EOFs, with $i = 1, j = 2$ (solid),$3-5$ (dashed). a) and b) are obtained using eigenvalues computed from the sample. See text for further explanation.

example. In analogy with the schematic of Fig. A.1, the errors are expressed as angular standard deviations α^*_{1j} of the direction of the first sample EOF with its true direction, in the plane that it forms with each mixing EOF.

The leading EOF of SLP is expected to have smaller sampling errors than geopotential height at other tropospheric levels, because its leading eigenvalue λ_1 is more dominant than in the mid-troposphere (Fig. A.4), so β_{1j} and α^*_{1j} are also correspondingly smaller. The SLP EOF1 angular standard deviation due to mixing between the leading two EOFs is estimated to be about 8°. generated random error can be a much faster and

At all stratospheric levels the sampling errors for the leading EOF are very small (2-5°), because the inherently low complexity of geopotential variability there makes

the first eigenmode even more dominant than at the surface. The leading EOF at the 500 hPa level is subject to particularly high mixing errors with all the subsequent three modes, and therefore is quite sensitive to sampling variability.

Figure A.6 plots the expected cumulative effect of mode mixing with the first n EOFs on the correlation of the sample EOF1 ($i = 1$) and EOF2 ($i = 2$) with the respective true EOF,

$$r_n = 1 - 0.5 \sum_{1<j\leq n} \alpha_{ij}^{*2}. \tag{A.25}$$

For EOF1 of both SLP and 500 hPa, mode mixing with the second eigenvector contributes roughly half, with EOFs 3-5 contributing another 25%. SLP EOFs 1 and 2 are much more robust with respect to sampling variability, compared to the respective EOFs of the 500 hPa level. The error in the leading 500 hPa EOF is in fact comparable to the error in EOF2 of SLP. The cumulative contributions of modes higher than 15 do not significantly alter the correlations shown for $n = 15$.

Figure A.7 shows, for the two levels, two pairs of sample EOFs $\hat{\mathbf{e}}_\mathbf{1} = \mathbf{e_1} + \sum_{j=2}^{15} \alpha_{1j}^* w_{1j} \mathbf{e_j}$, with $w_{1j} = +1$ for all j in the left panel and $w_{1j} = -1$ for all j in the right panel. These maps represent examples of the sampling variability which can be expected when computing EOFs from the current record of data. At both levels the strength of the Pacific center in the leading EOF is quite sensitive to sampling variability. However, over the Atlantic sector, the SLP EOFs are nearly identical, whereas the 500 hPa EOFs are quite different: one exhibiting zonally elongated features and the other much more wavelike. The area weighted correlation coefficients between each perturbed map and the unperturbed EOF are 0.94 for 500 hPa and 0.98 for SLP, in agreement with the values shown in Fig. A.6.

These empirical results are in agreement with the analysis of the hypothetical EOF spectrum presented in section A.3. In the observed dataset, which consists of about 150 independent time realizations, the sizes of the errors are expected to be substantially different for SLP and 500 hPa. Based on the results of Fig. A.3, it is

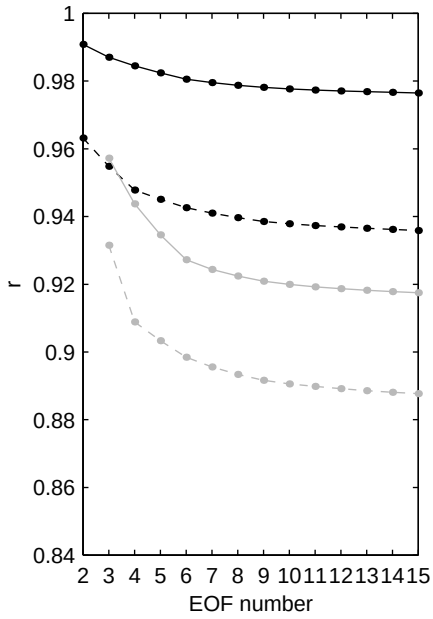

Figure A.6: SLP (solid) and 500 hPa (dashed) errors in EOF1 (and EOF2, in gray): expected correlation coefficient between sample and "true" EOF after cumulative mixing with EOFs up to 15. The error on EOF2 also includes the contribution from EOF1.

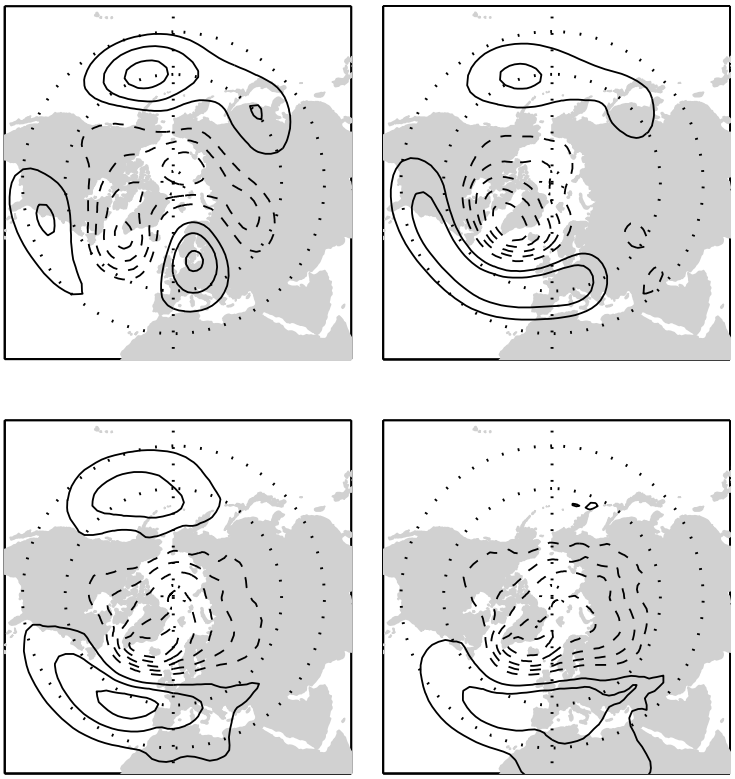

Figure A.7: Leading sample EOF of 500 hPa geopotential height (upper panels) and SLP (bottom panels) including plus or minus 1 standard deviation contributions due to mode mixing with the respective EOF 2 to 15 for a sample of size $T^* = 150$. Contour intervals: 15 m (500 hPa) and 1.2 hPa (SLP).

estimated that in order to reduce the sampling error in the leading 500-hPa height EOF to that of the leading SLP EOF it would be necessary to triple the number of independent monthly samples from ~ 150 to ~ 450.

A.5 Conclusion

We have developed simple, easily applied formulas for estimating how reliably an EOF of a time-varying field of data can be determined from a finite data record. The formulas show that if the North et al. (1982) criterion holds for the corresponding eigenvalue of the covariance matrix, the EOF can be estimated fairly reliably. We use monthly mean Northern Hemisphere wintertime 500-hPa geopotential height and SLP as examples, and find that the leading EOF of SLP can be estimated to within approximately half the error of the leading EOF of 500-hPa height from the current data record.

VITA

Roberta Quadrelli was born in Bologna, Italy, in 1971. In 1992 she earned a music degree in violin at the Conservatory of Music of Bologna and continued her career as a violin player for the next two years. After pursuing her artistic education she decided to also follow her native scientific curiosity, and enrolled into the Physics Department at the University of Bologna. She graduated in 1998 majoring in Geophysics and Atmospheric Sciences under the guidance of Stefano Tibaldi and Franco Molteni, and soon after she started working as a research fellow in the climate section of the Meteo Center of Emilia Romagna (ARPA-SMR). In September 1999 she joined the Department of Atmospheric Sciences at the University of Washington in Seattle, USA, to work with John M. Wallace, and in Autumn 2004 she earned her Ph.D. degree.